Doctoral Dissertation

Doctoral Program in Electronic Enginering (31st cycle)

Microwave Imaging Specialized Hardware for Biomedical Applications

Imran Sarwar

* * * * * *

Supervisor

Prof. Mario Roberto Casu

Doctoral Examination Committee:

Dr.-Ing. Marko Helbig, Referee, Technische Universität Ilmenau

Dr. Giuseppe Ruvio, Referee, National University of Ireland Galway

Politecnico di Torino

April 1st, 2019

I hereby declare that, the contents and organization of this dissertation constitute my own original work and does not compromise in any way the rights of third parties, including those relating to the security of personal data.

. . . .

Imran Sarwar

Turin, April 1st, 2019

Summary

Breast cancer and brain stroke are two critical and dangerous problems affecting people worldwide. Breast cancer is the most common and second leading cause of death in females after lung cancer, while brain strokes are among the common causes of permanent disability or death worldwide with more than 15 million people getting affected annually according to statistics.

Breast cancer in its early stages is not much harmful and can be treated with a high success rate if diagnosed accurately. Hence the critical factor is to have a system to detect it in the early stages reliably. During a brain stroke, abnormal blood flow inside the head of the patient starts, which can result in devastating changes in the brain or, at worst, lead to death. On-the-spot accurate detection and monitoring employing head imaging in the post-acute stage are of utmost importance for appropriate medication for ensuring the proper care and complete recovery of the patient. Currently available standard imaging tools such as X-Ray Mammography, which is considered as gold standard for breast cancer detection, while MRI and CT, the most common stroke monitoring techniques, are limited due to their cost, size, use of ionizing radiations and low reliability. These limitations encouraged us to design alternative imaging techniques, to overcome their limitations and to get reliable results.

The work done in this thesis is in the framework of designing highly efficient, low cost, low power, and reliable Microwave imaging (MI) systems to detect Breast cancer and to monitor brain stroke. MI systems have the advantage of using low ionizing radiations, low cost, easy of use and are capable of producing reliable results.

The designed MI system for breast cancer detection is compact because it uses components off-the-shelf (COTS) to transmit and receive microwave signals, instead of heavy lab equipment like Vector Network Analyzers (VNA) which other MI systems usually use. I-MUSIC [90] is the preferred imaging algorithm for the designed MI system over other common proposed approaches because it provides many processing and practical advantages over them. Measurements are performed on 2D, and 3D breast phantoms having properties similar to normal breast tissues and tumor and the results obtained from the designed MI system are compared with the results obtained with the VNA based MI system. The results from the designed COTS-based MI systems are very similar to the results obtained with VNA and in some cases even better. Moreover, the acceleration of the computationally intensive parts of the algorithm due to the implementation of hardware acceleration in the FPGA of Zynq SoC (a development and evaluation board), increased the execution time of the algorithm 20 times faster than its execution in a high-performance server.

The designed MI subsystem in this thesis for stroke monitoring, is a low cost, low power and portable system. The imaging algorithm used for stroke monitoring is Truncated Singular Value Decomposition (TSVD) [104], different from I-MUSIC. In this algorithm, signals are acquired at a single frequency, and the execution of the algorithm for image reconstruction is much faster. The algorithm detects the variation of the blood mass across two successive data, and then the reconstructed image shows this variation. Moreover, the imaging algorithm is accelerated due to the implementation of hardware accelerator in the FPGA of the Zynq SoC and the obtained results are at least five times faster than the software execution of the algorithm.

Both the MI systems presented in the thesis successfully produced very reliable results, and at the same time they were low cost, compact, consumed very low power with fast execution times.

Acknowledgements

First of all, I would like to thank Allah Almighty for everything which he has blessed me. I want to express my sincerest gratitude to my principal advisor **Prof. Mario Roberto Casu** for his excellent supervision, encouragement and professional guidance during the course of my Ph.D. It has been very inspiring and fruitful to work under his supervision. I have learnt a lot from both his scientific expertise and his attitude towards research. The most important thing about him was his friendly and co-operative approach, and I am fortunate to have him as my supervisor. I would also like to acknowledge my research group members for their guidance throughout my Ph.D. studies and for their help and time. I want to offer my kind regards to all those who supported me during this research endeavor. Besides, I would like to thank the Department of Electronics and Telecommunication of Politecnico di Torino for providing a good research environment and facilities. I am also very thankful to all my friends in Turin, my flatmates and friends from my home city for their support, courage and for making my life in Turin more exciting. I also want to thank Higher education Commission (HEC) of Pakistan for providing me the opportunity and supporting me financially to get higher education in one of the prestigious institution in the world. Last but not the least, I wish to express gratitude to my family for their support during all these years of studies, and standing beside me, whenever I needed their support and also for believing in me and encouraging me to do things on my way. Thank you all..!!

This thesis is dedicated to my loving parents

’This thesis is dedicated to my Late father, Ghulam Sarwar. He was the best father one could ask for, his support, love, care, and dedication for the family was the most valuable and beautiful thing in my life. I will always miss his presence in my life, but also I am very sure his blessings are always with me, and always he is and will be in my heart. I would also like to dedicate this thesis to my mother for her support, care and love. Moreover, I wish her a long and healthy life’.

Contents

List of Tables

List of Figures

[empty]

Chapter 1

Introduction

1.1 Background and Motivation

Breast cancer is the 2nd most common cause of death in females after lung cancer [1-4]. In the US only in 2017, 252,710 new cases of invasive breast cancer were estimated to be diagnosed while 40,610 deaths due to breast cancer were also estimated [5]. According to the world health organization, in 2018 deaths caused due to breast cancer globally were 2.09 million, which is equal to the leading cause of deaths (lung cancer) in humans by cancer [6]. Table 1 shows the percentage of new estimated female breast cancer cases and death for the US according to the American Cancer Society for different ages.

Table 1.1: Estimated New Female Breast Cancer Cases and Deaths by Age, US, 2017.

	In situ Cases		Invasive Cases		Deaths	
Age	**Number**	**%**	**Number**	**%**	**Number**	**%**
<40	1610	3%	11160	4%	990	3%
40-49	12440	20%	36920	15%	3480	9%
50-59	17680	28%	58620	23%	7590	19%
60-69	17550	28%	68070	27%	9420	23%
70-79	10373	16%	47860	19%	8220	20%
80+	3760	6%	30080	12%	10910	27%

Source: www.cancer.org

Table 1 shows that the percentage of females suffering from breast cancer increases with age. Breast cancer in its early stages gives no symptoms of its presence. However, breast cancer can be treated appropriately if detected at an initial stage. In fact, the survival rate can be up to 97% if detected early and treated accordingly [7], which further stresses the requirement for efficient, highly reliable, comfortable and cost-effective methods of breast cancer detection at early stages.
Similar to breast cancer, brain stroke is another most common cause of mortality globally [8-10] and is the leading cause of mortality in aging societies such as Europe [11][12] and the US [13]. Brain stroke can be either of hemorrhagic or ischemic type. For normal functioning of brain, blood supply to brain must be properly functioning and if due to any reason this supply gets affected it can result in brain stroke, which can cause permanent disability in humans, heart problem and sometimes results in death, with more than 15 million people getting affected worldwide on a yearly basis [14]. During brain stroke blood is stored inside the human head, it can happen due to the bursting of a blood vessel inside the intracranial chamber or due to physical trauma, abruptly torn because of hypertensive damage or due to any other malfunction or venous infections. After brain stroke, abnormal blood flow inside the head occurs, which can result in irremediable changes or, at worst, lead to death. It can be said without any doubt that the rapidity of intervention and treatment are very important for quick and effective therapy. On-the-spot accurate detection and monitoring employing head imaging in the post-acute stage is of utmost importance for appropriate medication for ensuring the proper care and, complete recovery of the patient [15][16].

Imaging methods like X-ray mammography, Magnetic Resonance Imaging (MRI), Computed Tomography (CT), Ultrasound, and Positron Emission Tomography (PET) are widely used to detect, identify, monitor and in some cases treat many injuries to human body including breast cancer and brain stroke.

Breast cancer detection

In case of breast cancer detection, X-ray mammography is considered the gold standard, but it causes inconvenience to the patient during examination due to breast compression and sometimes can produce false positive and negative results [17]. It also uses ionizing radiations, which have a high risk of producing harmful effects in the body.

Brain stroke monitoring

The main problem with brain stroke monitoring is that it is performed too late at the hospital due to non-portable access of MRI/CT scanners and their high cost. Moreover, there is no imaging technique for monitoring the stroke without moving over the patient.

Recent efforts to look for a more accurate, reliable, safe, portable, low power consumption and cost-effective imaging system have indicated Microwave imaging (MI) as a good alternative for biomedical imaging applications.
MI is an imaging technique, which uses Electro-Magnetic (EM) waves in microwave range (300 MHz-300 GHz). MI is being used for different kind of applications like NTD&E (nondestructive testing and evaluation), hidden weapon detection, through-wall imaging, health monitoring, and medical imaging.

Recently, MI for biomedical applications attracted the interest of researchers all over the world due to its ability to detect local variations of the dielectric properties of tissues. MI can be either of quantitative type (providing electrical and geometrical parameters of an object to be imaged) or qualitative type (providing information about a hidden object) depending upon the technique used to generate images. In the first step of MI, target is first hit by electromagnetic waves emitted by a set of antennas and then the scattered waves are collected by same (monostatic system) or different antennas (bistatic or multistatic system). In the second step of MI, the signals obtained from the scattered waves are post-processed and are used to generate different kind of images, depending on the MI algorithm used. If there is a dielectric contrast between the target and the surrounding area hit by MI, this contrast results in a larger reflection of the backscattered waves.

Experimental research has shown that normal tissues have significantly different dielectric properties as compared to malignant and benign tissues [18-19]. Malignant tissues are characterized by higher dielectric contrast compared to benign and normal tissues [20]. MI maps electrical properties of tissues, without any invasive procedure [19]. Many researchers have put significant efforts to detect this difference and to produce images that highlight it, particularly for breast cancer detection [21]. Recent research has shown that MI can also detect abnormalities in the human brain such as those created by a hemorrhagic stroke [22]. This is because during the occurrence of a stroke accumulation of bleeding changes the electrical properties of the affected part of the brain resulting in a detectable dielectric contrast between the affected area and the surrounding part of the brain. By striking brain with low power EM waves and acquiring the scattered EM waves, we can image the state of the brain stroke at different time intervals to monitor its evolution.

1.2 Challenges of the Microwave Imaging system for biomedical applications

Researchers have proposed various MI systems for biomedical applications, especially for breast cancer detection and brain stroke monitoring. However, these microwave imaging systems have some limitations: On the one hand the imaging algorithms may need a processing that may take an excessively long time for a practical application. On the other hand, since these systems are often based on standard microwave equipments, they are not portable and do not have the flexibility that is required for continuous monitoring. By solving the problem of portability and non-ionizing radiations, microwave imaging systems could have a disruptive impact in the general medical practice, by shifting the clinical assessment path from the radiology department to general clinics and potentially even to ambulances and medical offices.

1.3 Aims of the thesis

This thesis contributes to the field of MI for biomedical applications, both for breast cancer detection and brain stroke monitoring. In particular, for the part concerning breast cancer detection, the aims of the thesis are:

- ⇒ To contribute to the construction, characterization, and improvement of an MI system based on Commercial Off-The-Shelf components (COTS).
- ⇒ To enable the acceleration of the execution time of one of the effective MI algorithms by implementing hardware accelerator in field programmable gate array (FPGA) to offload its computationally intensive parts.

For the part concerning to brain stroke monitoring, aims of the thesis are:

- ⇒ To contribute to the design of a compact and low power MI subsystem for continuous bedside monitoring of brain stroke.
- ⇒ To accelerate the execution time of the Imaging algorithm for producing fast images by the applications of hardware acceleration in FPGA on a target architecture.
- ⇒ To reduce the cost and power consumption of the MI systems by using low cost and low power components.

1.4 The novelty of the research

The main novel aspects of the research activity described in this doctoral dissertation are summarized in the following.

1.4.1 Breast Cancer detection:

An improved and efficient MI imaging approach, Interferometric MUltiple SIgnal Classification (I-MUSIC) [90] was adopted for breast cancer detection. This approach allows detecting the most scattering points inside the breast by using microwaves at few selected frequencies in a relatively small bandwidth. This allowed us to use the low-cost components working between 1.4 and 1.6 GHz. Moreover, since the image reconstruction algorithm used in I-MUSIC avoids non-linear inversion and the associated processing issues, we could accelerate the execution time of the MI system by pairing an embedded processor with ad-hoc developed hardware running in an FPGA.

The hardware accelerated MI system executed imaging algorithm 20 times faster than multicore CPU.

1.4.2 Brain stroke monitoring.

An MI algorithm for brain stroke monitoring based on Truncated Singular Value Decomposition (TSVD) [104] has been analyzed in detail for best hardware acceleration in a low-cost embedded system with FPGA. The bottleneck of the computation has been deployed in the FPGA.
Hardware acceleration implemented in FPGA speeds up the execution time 5× compared to its software execution. To the best of our knowledge, this MI subsystem is the first for accelerating MI algorithm for brain stroke monitoring.

1.5 Thesis organization:

This thesis consists of the following chapters.

Chapter 1 is the introduction chapter and provides a summary of the research background. This chapter highlights the importance of the MI system to meet the challenges which other imaging techniques are facing. Finally, it highlights the aims and the novel contributions of the research.

Chapter 2 contains the literature review related to the research work performed in this thesis. It explains briefly breast cancer and brain stroke. Different imaging techniques being used, and their limitations are discussed in this chapter. The basis for MI and its detection principle is also discussed. The chapter is concluded with the discussion on the MI systems and the importance of portable and reliable MI systems for breast cancer detection and brain stroke monitoring.

Chapter 3: In this chapter the MI approach (I-MUSIC) used for breast cancer detection is explained briefly. Its main parts related to detection are discussed. The chapter is concluded with a short discussion about its implementation on the Zynq SoC.

Chapter 4 is a detailed discussion about the MI system, which is designed during research. In this chapter adopted methodology, components used, challenges which were faced during the system implementation and all the important details of the MI systems are discussed. In the chapter factors which can affect the performance of the system are analyzed and how to remove their effect from the final results is also discussed.

Chapter 5 contains the results obtained from the MI for breast cancer are discussed. The results are compared with the results obtained using standard microwave equipments,e.g. a VNA. In this chapter we can see that the designed COTS-based MI system has successfully detected tumors in the breast phantom and has a performance comparable to an MI system using a VNA.

Chapter 6 is about the MI imaging subsystem for brain stroke monitoring. In this chapter details of the subsystem and the acceleration of the imaging algorithm for brain stroke monitoring are discussed. In the chapter the designed hardware accelerator for accelerating the execution of imaging algorithm is explained in detail and then the chapter is concluded with the obtained results.

Chapter 7: This chapter is the conclusion of the thesis.

Chapter 2

Literature Review

2.1 Breast Cancer

The female breast is divided into two main parts, breast gland and ducts [23]. In breast gland, there are about 15 to 20 sections called lobes, and inside each lobe there are many small structures known as lobules, at the end of each lobule there are tiny sacs (bulbs) which produce milk in the breast. Lobules, lobes, and bulbs are connected by a network of thin tubes which are known as ducts. One of the functions of the ducts is to carry milk from bulbs towards the areola, which is the dark area of skin in the center of the breast. Ducts join to make a larger duct ending at the nipple, where milk is delivered. In general, the breast is composed of fat, skin, glandular and connective tissues. The breast lies at the chest, and its shape is different among individuals; consequently, proportions of fat, glandular and connective tissue also vary among individuals, this proportion also varies during pregnancy and menstruation [24]. Breast cancer has many types, but the two main types are non-invasive and invasive types. In Non-invasive, cancer tumor is found in the ducts of the breast, and this type of cancer does not spread outside the breast while in case of invasive, cancer can spread outside of the breast which makes this type the dangerous type of breast cancer.

2.1.1 Electrical properties of the breast

Microwave imaging for cancer detection is possible because of the different electrical properties of tumor and surrounding tissues. Relative permittivity (ϵ) and conductivity (σ) are the two main electrical properties used in MI for cancer detection. Permittivity and conductivity both give different types of information about the human body tissue as permittivity tells about the ability of a tissue to store microwave energy whereas conductivity informs about the loss (dissipation) or attenuation (absorption) of microwave signal that it faces while propagating through the tissue. The higher the conductivity of the tissue, the higher the loss or attenuation of the microwave signal. The electrical properties of tissues, most importantly their relative permittivity, are determined by the amount of water they contain [25-29]. Tissues such as fat have lower relative permittivity compared to tissues like muscle, skin or tumor because these have high water content than the fat has [30-31].

2.1.2 Currently used imaging methods

Commonly used screening methods for breast cancer detection are X-ray Mammography, Ultra-sound, Magnetic Resonance Imaging (MRI), and Computed tomography (CT). X-ray Mammography is considered ”gold standard” for Breast cancer detection.

X-Ray Mammography

X-ray mammography is the most recommended diagnostic tool by doctors for breast cancer detection. In this technique, breast is compressed between two plates, and then X-rays are passed through the breast and recorded onto film as shown in fig 2.1. X-ray mammography has the advantage that it has good sensitivity for normal breast types, the high-quality resolution is also possible and the time for the examination is also short while on the other side if the breast is dense then the sensitivity decreases. For its detection process, X-ray mammography uses ionizing radiation which has harmful effect on the human tissues. The fact that while examining the patient, the breast is compressed onto plastic plates causes inconvenience for the patient and sometimes can be very painful.

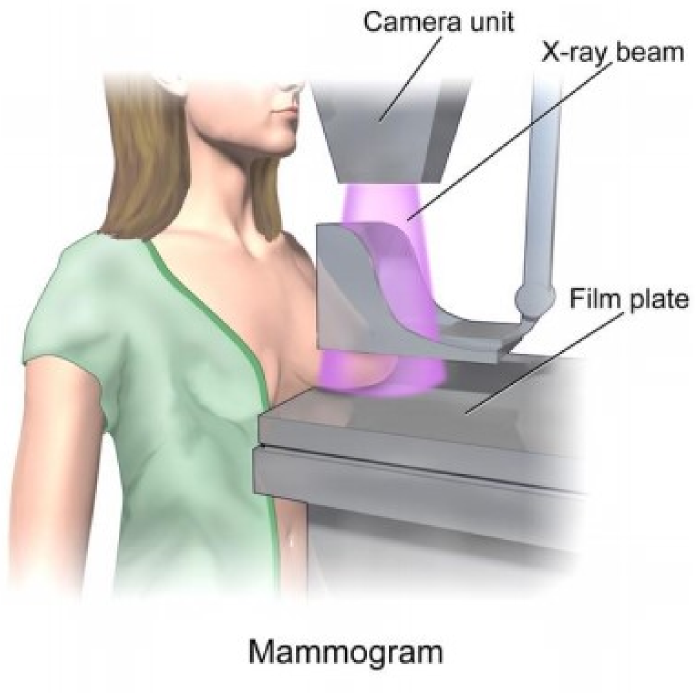

Figure 2.1: Compressed breast of patient during X-ray Mammography.
Source: https://www.theengineer.co.uk/laser-device-detects-breast-cancer-that-x-rays-can-miss/

Ultrasound

In this technique, Ultrasonic waves with a frequency range of 1 MHz to 15 MHz are used to diagnose internal body structure. During breast cancer detection this imaging technique determines whether the area under consideration has normal tissues or cancerous tissues. Ultrasound imaging is considered a safe screening tool since it uses non-ionizing radiation and is a noninvasive procedure. It can easily detect between normal and suspicious tissue since it has high image contrast and resolution. However, ultrasound has limitation to detect breast cancer, because during breast cancer detection the results produced have a high percentage of false positive and negative results.

Ultrasound screening results depend heavily on the skills of the person performing the test [35].

Magnetic Resonance Imaging (MRI)

Magnetic Resonance Imaging (MRI) is a non-invasive imaging technique that uses radio waves and strong and powerful magnets to create images of tissues, bones, organs, and other internal body structures. For breast cancer detection, MRI is generally used on patients already been diagnosed with breast cancer, to evaluate the size of the tumor or to look for other tumors in the breast. MRI scanning can detect small cancerous tissues that are not identified with X-ray mammography [36]. However, MRI often produces false-positive results for breast cancer, due to which MRI is generally not preferred as a standalone scanning technique but to be used along with X-ray mammography for reliable results. During breast cancer detection with MRI, the patient must lie down on a table as shown in fig 2.2.

Figure 2.2: MRI for Breast Cancer
source:http://www.breastlink.com/services/breast-imaging/breast-mri/

The advantage of MRI over other techniques is that it does not uses ionizing radiation for its operation; however its disadvantages are: it is a time-consuming procedure, immovable MRI machine, and false positive and negative results [37].

Computed tomography (CT)

CT scanning uses special X-ray equipment to obtain cross-sectional images of the human body. Screening using CT can be performed on any part of the body. For breast cancer detection, it gives information about the presence of a tumor. If a tumor is detected, it can also provide information about its location and size and most importantly it can provide information on whether the cancerous cells have spread to other parts of the body. Scanning by CT is very comfortable and causes no pain to patients, but the amount of radiation used during CT screening is higher [38], which makes the procedure harmful for frequent testing of a patient.

2.1.3 Summary of the conventional breast cancer detection methods

The existing methods for breast cancer detection suffer from safety, efficiency, discomfort and false diagnosis. During breast cancer, detection at early stages is crucial for proper treatment before it reaches to a dangerous stage. Over the past few decades a number of research groups have conducted researches and experiments on alternative and complementary tools and methods. Microwave imaging has emerged as a possible complementary method for early breast cancer detection. The reason is that tumors have a very detectable dielectric contrast at microwave frequency range compared to normal tissues, and MI system can detect these strong backscattered signals for imaging.

A microwave-based imaging system is safe as it is noninvasive and uses non-ionizing radiations. Portability, cost and execution time of MI system can be further improved by using hardware acceleration in FPGA and by using commercially available low-cost off-the-shelf components.

2.1.4 Microwave Imaging Systems

Microwave imaging (MI) has been of interest for researchers over many years for the detection of human body tissue abnormalities. The physical basis of microwave imaging technique is the ability to quantify or detect the dielectric difference between different body tissues based on their permittivity values [40]. This potential ability to distinguish between them could help to detect breast cancer in early stages. MI can be either an alternative technique or complementary imaging tool to existing imaging methods. The advantages include a wide range of frequencies, negligible health risk, low cost, good detection capabilities compared to conventional methods. The highly competitive commercial radio frequency (RF) electronics industry has helped to push down the prices of electronic devices drastically, and use of these components in MI system can help us to reduce the cost of the system. The execution time of the sometimes complex imaging algorithm can be improved by the application of hardware acceleration in FPGA. Microwave imaging is classified into three main categories based on the approach used namely, passive, hybrid and active methods. These approaches have been investigated by researchers extensively for detection of breast cancer at early stages. These methods are explained briefly below.

Passive Microwave Imaging

In Passive microwave imaging (figure 2.3), the contrast between the temperatures of the malignant tissue to that of the healthy tissue is measured. Several investigators examining breast cancer patients have reported that there is a considerable difference in temperature between healthy and cancerous tissue. According to their findings, cancerous tissues produce more heat and are more active to microwaves [41] than normal tissues. According to the authors of [42] tumors cannot keep their temperature within the normal limit (thermoregulatory capacity). During Passive Microwave imaging, by using Radiometers, the temperature difference between the tissues is measured, and if a tumor is present inside the breast, then the radiometer will record higher temperature values then normal tissue temperature.

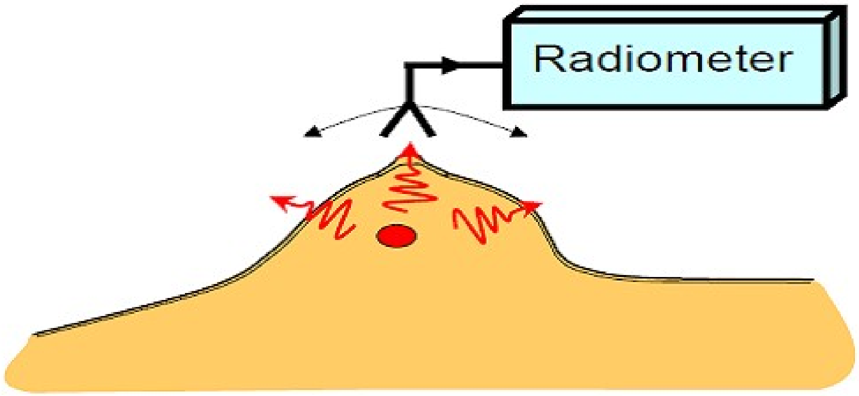

Figure 2.3: Passive Microwave Imaging.

Active Microwave Imaging

In active microwave imaging an antenna or antenna array is used for transmitting low power microwaves to penetrate human tissues from different positions, and then the backscattered response is recorded. Using a suitable processing algorithm 2-D or 3-D images of the tissues are obtained. Two approaches, Microwave Tomography and UWB radar-based [43][44] are commonly used microwave techniques for active microwave imaging. Both these techniques have produced promising results and are briefly explained below.

Microwave Tomography

In Microwave Tomography imaging technique, multiple signals are collected from antennas placed at different positions around the breast. These microwave signals are backscattered from the breast and are received by antennas for processing. From these backscattered microwave signals an image is created which gives information about dielectric constant of the breast based on its permittivity using inverse scattering. Forward and reverse electromagnetic field problems are solved for detecting and locating the cancerous tissue. By assuming a known distribution of the complex dielectric constant of the object to be imaged a forward problem is solved and then these electrical parameters are compared with measured data. Using an optimization algorithm, the process is repeated several times by changing the electrical parameters to a new value. Measured data is then compared with new values obtained, and the procedure is repeated till a low error between the calculated and measured data is achieved.

UWB Radar Based Microwave Imaging

In this method amplitude of the scattered signal and the time delay between the transmitted and scattered signal contains the information about the size and position of the tumor. In UWB Radar based microwave imaging electromagnetic signal is transmitted towards the target and the signal is either absorbed or backscattered; this scattering is used to form an image which helps in identifying the position of the strong reflections. In UWB different imaging algorithms are used such as Microwave imaging via space-time beamforming, confocal or delay-and-sum method or tissue sensing adaptive radar. The confocal method is one of the most common approaches used in UWB radar technique [46-48]. UWB Radar based microwave imaging tumor detection focuses mainly on detecting the existence of a strong reflection, which makes this approach computationally more efficient than microwave tomography [45].

Hybrid Microwave Imaging

In hybrid techniques, two different physical modalities and techniques are combined. In one such hybrid technique, microwave energy first illuminates the breast, and then pressure waves are detected due to the expansion of heat. Due to higher conductivity, tumors absorb more microwave energy as compared to healthy tissues, hence producing stronger pressure waves; these pressure waves are detected using sensors or antennas (ultrasound transducers) to estimate the presence or absence of any abnormal tissue as shown in fig 2.4. This technique provides both sensitivity to tumors and high resolution of images. Further details of this technique can be found in [49].

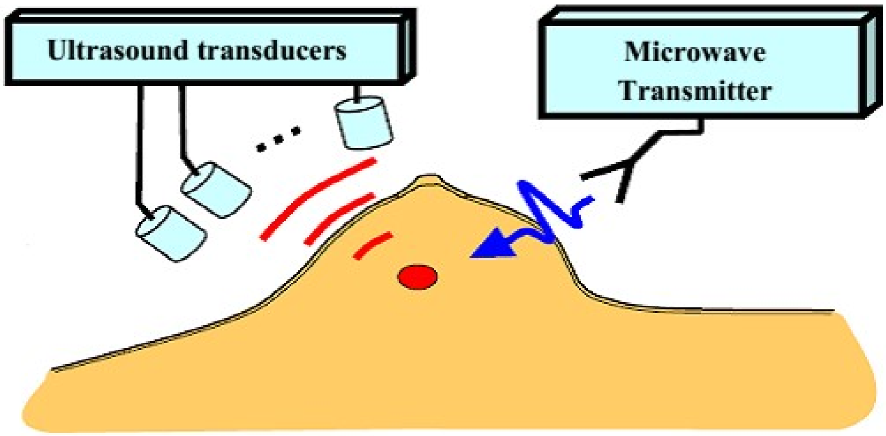

Figure 2.4: Hybrid Microwave Imaging.

Having information on the tumor on a different energy modality may help to increase the sensitivity of MI. Based on this principle, M. Helbig and his team at the Technische Universitat of Ilmenau, Germany, used magnetic nanoparticles (MNP) for an enhanced microwave breast cancer detection system [119]. They increased the diagnostic reliability of their MI system assuming that the functionalized magnetic nanoparticles accumulate selectively within the tumor tissue. Using an external magnetic field, magnetic nanoparticles are first modulated. Then changes in scattering of the nanoparticles due to the application of the external magnetic field are measured using ultra-wideband (UWB) sensors and an M-sequence UWB radar technology, which ultimately resulted in the detection of the nanoparticles. By differentially observing the response of a breast phantom between ON- and OFF-state of the magnetic field, Dr. Helbig and collaborators at Ilmenau showed that with this technique the detectability in an actual measurement case can increase. Further details and results of this technique can be found in [119].

2.1.5 History of Microwave Imaging System

Researchers have shown interest in the potential of MI as good imaging from past few decades; important initial work in this regard was performed by Larsen and Jacobi in late 1990s. By immersing in water an antenna which they developed, they were able to image the internal structure of a canine kidney [50]. Since then, due to continues efforts of researchers, variety of applications of MI have been reported in the literature, from detection of cancer in the lungs, ischemic heart disease to pediatric transcranial brain imaging. Among these techniques, detection of breast cancer at early stages are of very importance in recent times. A good discussion about the sequential growth and advances in MI system for breast cancer detection can be found in [51-61].

2.1.6 Research Gap

Microwave imaging systems are considered as good imaging alternatives or complementary tools to available methods for breast cancer detection. Microwave imaging techniques rely on the difference of the electromagnetic parameters between different biological tissues and offer a method with a wide range of advantages such as being a low-cost and portable system, using non-ionizing radiations and providing fast and reliable results. However, inspite of providing all these advantages, still, a proper MI system is needed to image the human body for practical clinical applications. Different type of MI system has been proposed by researchers for breast cancer detection. However, these systems are either bulky and use heavy and costly equipment like Vector Network Analyzers (VNA), or they require time for producing results, which is unacceptable for clinical applications. Finally, the lack of portability is another issue that, if solved, would provide a dramatic shift of the current clinical path. All these limitations motivated us to work on a new MI system to minimize the limitations mentioned before without affecting the performance and reliability for detecting breast cancer in initial stages.

2.1.7 Proposed Research on MI for Breast Cancer Detection

The first objective of the work presented in this thesis is to propose solutions to improve MI systems, especially for breast cancer detection. We propose an improved approach for MI by using I-MUSIC [90] as an imaging algorithm for breast cancer detection. This method does not require a large band to detect the main scatterer inside the breast. The system developed works in frequency domain and provides many flexibilities compared to tomography or UWB radar-based approaches. To reduce the cost and improving the execution time of the MI system, we use COTS and hardware acceleration with FPGA.

2.2 Brain stroke

Brain stroke occurs, when the blood supply to the brain is interrupted, preventing the supply of oxygen and nutrients to brain tissues. Brain stroke can be caused either by blockage of blood flow or by bleeding into the brain. There are two main types of brain stroke Ischemic and hemorrhagic stroke shown in figure 2.5.

Ischemic stroke: During ischemic stroke blockage of blood vessel occurs in the brain and this is the most frequent cause of stroke causing 80% of the cases. Blockage can occur either due to the formation of the clot within the blood vessel or by movement of the clot from another part of the body like the heart to the brain or due to narrowing of an artery inside or in the path to the brain.

Hemorrhagic stroke: if bleeding occurs into the brain or at places surrounding the brain then hemorrhagic stroke occurs.

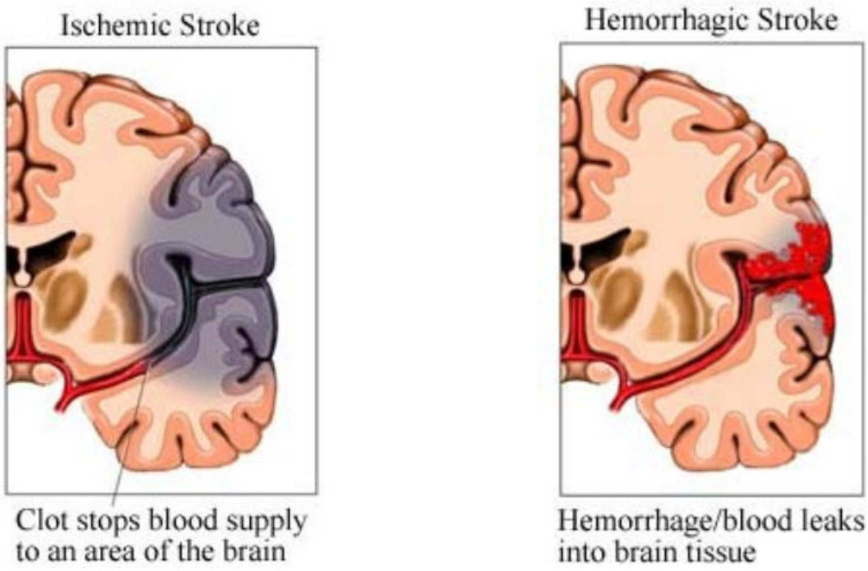

(a) Ischemic Stroke

(b) Hemorrhagic Stroke

Figure 2.5: Types of Brain Stroke
Source:https://www.mayoclinic.org/diseases-conditions/stroke/symptoms-causes/syc-20350113

2.2.1 Electrical properties of the brain

The human brain consists of brain tissues and blood, both of which have different dielectric contrasts. In case of stroke the dielectric difference between healthy and diseased tissue increase due to the accumulation of blood at the point in the brain where the stroke occurs [32-33]. Microwave Imaging for stoke monitoring uses this difference for detection and monitoring of stroke.

2.2.2 Currently used Imaging Methods

Standard techniques used to monitor brain strokes are MRI, CT and Ultrasound, where MRI and CT are considered as gold standard for monitoring brain strokes [34]. These techniques are explained very briefly in below sections.

Ultrasound

In this technique, Ultrasonic waves with a frequency range of 1 MHz to 15 MHz are used for diagnosing an internal body structure. To monitor brain stroke with ultrasound, flow of blood in the brain is evaluated. Ultrasound imaging is considered a safe screening tool since it uses non-ionizing radiation and is a noninvasive procedure. It can easily detect between normal and suspicious tissue since it has high image contrast and resolution. However, ultrasound has limitation for brain stroke monitoring. During brain stroke monitoring, adult patients are challenging to be diagnosed by ultrasound due to their skull structure, and a large number of tissues and the results can be affected easily by wounds or recent surgical incision, changes in blood flow due to heart disease or due to non-uniform heart rhythms.

Magnetic Resonance Imaging(MRI)

Magnetic Resonance Imaging (MRI) is a non-invasive imaging technique that uses radio waves and strong and powerful magnets to create images of tissues, bones, organs, and other internal body structures. For brain stroke monitoring and imaging, MRI is often considered as gold standard and provides better results than other imaging techniques. With MRI scanning it is also possible to distinguish between the ischemic and hemorrhagic strokes which is vital for proper and timely treatment. Figure 2.6 shows a typical setup of a patient undergoing MRI scanning.

Figure 2.6: MRI for stroke monitoring
source: https://www.radiologyinfo.org/en/info.cfm?pg=headmr

Computed tomography(CT)

CT scanning uses special X-ray equipment to obtain cross-sectional images of the human body. CT scan is very common for initial brain stoke monitoring especially when the patient is in the emergency room for the ischemic type. CT scan has the advantage of showing abnormalities in the brain and can identify if the abnormality is caused by insufficient blood flow (ischemic stroke) or due to the ruptured blood vessel (hemorrhage), or another kind of problem. This technique has the advantage of being comfortable but the amount of radiation used during CT screening is higher [38].

2.2.3 Summary of common brain stroke monitoring techniques

Main limitations with existing methods to monitor brain stroke monitoring are safety, efficiency, time of operation, and most important, the lack of portability. The existing methods for monitoring brain strokes mostly uses ionizing radiation and the equipments used are bulky and hence are not portable and they can not be used as a bedside monitoring device or to be used in ambulances for initial diagnosis and care. Researchers have proposed microwave imaging systems as a possible complementary method for brain stroke monitoring. The reason is that bleeds and blood clots have a very detectable dielectric contrast at microwave frequency range, and MI system can detect these strong backscattered signals for imaging. Evolution of MI system for brain stroke monitoring can be found in [62-68].

A microwave-based imaging system is safe as it is noninvasive and uses non-ionizing radiations. Portability, cost and execution time of MI system can be further improved by using hardware acceleration in FPGA and by using commercially available low-cost off-the-shelf components.

2.2.4 Research Gap

Microwave imaging systems in general are low-cost, and use non-ionizing radiations for detection purposes. However, inspite of these advantages, still, a proper MI system to monitor brain strokes in a practical clinical applications is needed. Different type of MI system has been proposed for brain stroke monitoring. However, most of the systems are fixed and does not provide the critical property of portability,in fact a portable imaging system using non-ionizing radiations is not only important for brain stroke monitoring but it can also be used for other clinical applications. These limitations motivated us to work on new MI systems to minimize the limitations mentioned earlier without affecting the performance and reliability.

2.2.5 Proposed Research on MI for Stroke Monitoring

The second objective of the work presented in this thesis is to propose a new MI subsystem to improve MI systems for brain stroke monitoring. The proposed MI system is portable and can be used as bedside monitoring subsystem. The imaging algorithm is accelerated due to the implementation of the hardware accelerator in programmable system-on-chip where FPGA offloads heavy part of the computation from ARM-based CPU for improving the execution time of the system to get results instantly.

2.3 Conclusion

There are four main imaging techniques in clinical applications to image the abnormalities of the human body. These methods are X-ray mammography, Ultrasound, MRI and CT scan. Each of these methods have their own limitations such as the use of ionizing radiations, costly, bulky, immovable equipment, and time-consuming procedure. Microwave imaging system has been proposed by researchers as an alternative or complementary technique to these available methods. The basis of the MI system relies on the dielectric contrast of the different human body tissues. Many researches reported in the literature have proved that there is a significant difference in the electrical properties of normal and abnormal tissues in the human body. The focus of the past research has been on validating the functionality of MI systems, both for breast cancer and brain stroke. There is lack of research focused on making these systems low cost, compact, portable, and fast. Use of non-ionizing radiations gives MI systems the freedom of repeating the procedure on patient many times for reliable and accurate results.
The next chapter is about the proposed "I-MUSIC" algorithm for breast cancer detection. This imaging algorithm has many advantages over the commonly used Tomography and UWB approaches.

Chapter 3

I-MUSIC Algorithm

Microwave Imaging for breast cancer detection is considered a useful diagnostic tool to complement and, in some cases, replace well established diagnoses techniques like X-ray mammography [73] and magnetic resonance imaging [69-71]. At microwave frequencies, benign, malignant and normal tissues have different dielectric properties [74]. Significant research has been put to build MWI systems to detect and image this difference without any invasive procedures. During the last two decades researchers have proposed several imaging techniques to image the dielectric difference between the benign, malignant and normal tissues and these techniques, in general, are categorized as linear and non-linear inversion techniques. In nonlinear inversion techniques the dielectric and conductivity parameters of the breast are imaged while in linear inversion techniques (also known as radar focusing) breast tumor can be detected and localized. Both techniques have their limitations, because non-linear inversion techniques are computationally intensive [117] and subject to issues such as false solutions and convergence problems, while linear methods being robust typically needs large bandwidths. Generally, Ultra-Wide-Band (UWB) Radar and Tomography are the proposed approaches for MI systems.

3.1 Ultra-Wide-Band (UWB) Radar

UWB Radar approach belongs to the class of linear scattering technique. In this approach the amplitude of the scattered signal and the time delay between the transmitted and scattered signal contain the information about the size and position of the tumor to be imaged [72]. This approach is a detection method since it determines the highest energetic spots in the field as determined by the highest dielectric contrast created by the presence of a tumor. To use the UWB radar approach in time-domain, new ad-hoc integrated circuits (ICs) must be developed [76-78]. It is possible to use this approach in the frequency-domain and reconstruct the UWB pulses via FFT, an approach usually referred in the literature as Stepped-Frequency Continuous Wave (SFCW) and in this case it is possible to use laboratory microwave tools, besides the developed new ICs [79-80], which have the flexibility of handling large bandwidth with the required accuracy and precision.

3.2 Tomography

This approach aims at reconstructing the dielectric profile of breast by collecting the scattered field at single or few selected frequencies. In this approach a non-linear and ill-posed inverse problem needs to be solved, which may cause problems of convergence to inaccurate results as well as problems of speed such that the execution of the algorithm sometimes can take days of CPU [72].

For our prototype, we adopted another approach “Interferometric- MUltiple SIgnal Classification (I-MUSIC)” developed by G. Ruvio and co-workers [90]. This approach offers many significant practical advantages over the other mentioned approaches. In the following we describe the I-MUSIC approach to highlight the reasons why we decided to use it. We refer the reader to the original publication for more details [90].

3.3 Interferometric- MUltiple SIgnal Classification (I-MUSIC)

I-MUSIC is an imaging approach belonging to a class of linear scattering imaging techniques like radar methods. However, it is different from both UWB-Radar and tomography approach because for the detection of scattering points inside breast it does not require a large bandwidth. The term interferometric in I-MUSIC is related to the diversity introduced by using different frequency samples. I-MUSIC can also be viewed as a multi-frequency variant of the time-reversal MUSIC [82]. In I-MUSIC by multiplicatively mixing different frequencies, images are obtained. I-MUSIC has been theoretically and experimentally verified by many researchers [81,91].

3.3.1 Advantages of using I-MUSIC algorithm

One of the advantages of I-MUSIC is the minimal dependence of a priori information of the antenna. In MI imaging systems different RF components are used and these components, especially the antennas play an essential role. During breast cancer detection presence of antennas in the proximity of breast is beneficial for better and reliable results. However, their presence in the proximity of the breast can change the antenna response and can cause degradation of the detection system if this depends on a precise knowledge of the antennas response. Hence it is important to consider the presence of antennas around breast for achieving the best performance from an MI system. A possible solution to this problem is to characterize the antenna for near-field MI by running some preliminary measurements or numerical solutions [118]. However, in practical situations, antennas are placed close to the breast, and their response is unknown because breast properties vary from patient to patient and this brings complication in the reconstruction problem of standard linear inversion methods. With I-MUSIC algorithm it is possible to detect tumor with very low contrast to surrounding breast tissue without considering the antennas response during image generation. The advantage of I-MUSIC over other approaches has been extensively studied and compared in [81,75,91].

I-MUSIC has two main advantages:

⇒ Reduction in overall cost, time for calibration and testing.

⇒ Complete independence from antenna characterizations.

Reduction in overall cost, time for calibration and testing

The use of I-MUSIC algorithm allows the use of simple monopole antennas, which can be easily fabricated in university laboratories. As shown in the next chapter, we built a prototype with Ultra-Wide-Band (UWB) monopole antennas, which we designed to be of small size, low cost, and with good matching performance when immersed in the coupling mediums. These coupling liquids are needed during measurements and their dielectric properties should be matched with dielectric values of the average female breast. The average dielectric values of these coupling mediums are one of the input parameters of the I-MUSIC algorithm.

Complete independence from antenna characterizations

When antennas are placed close to the breast, their response is mostly unpredictable because antenna response depends on distance from skin, profile of skin layer and its thickness. The sensitivity of the antenna to changes in all these factors (e.g. from one patient to another) bring complications in the image reconstruction. One of the reasons why we selected I-MUSIC over other imaging algorithms is the fact that I-MUSIC is completely agnostic of the antenna response, which means that it does not require any prior antenna characterization. Authors in [91] had tested the validity of I-MUSIC using three different antennas (planar monopole, semi-folded monopole, and antipodal Vivaldi antenna) without characterizing them. They performed experiments under the same conditions for all the antennas and compared their results with other microwave imaging techniques. The results generated using I-MUSIC were superior to other imaging techniques, and for all antennas, the results were almost identical. Even though I-MUSIC desensitizes the imaging procedure from a priori antenna characterization (near-field information), it still benefits from better energy focusing: for example, results with Vivaldi antennas are better than those obtained with monopole antennas due to an improved SNR for each scan.

3.4 A brief explanation of I-MUSIC

In our MI system (discussed in the next chapter) results are obtained by processing the acquired data with the I-MUSIC algorithm. The I-MUSIC algorithm allows generating an image through the acquisition of data obtained from several pairs of antennas in the configuration Tx/Rx, arranged in a circle around the breast. The algorithm consists of two main steps. The first step is clutter removal, which is mainly due to large scattering at the interface between coupling medium and skin interface, and second is the image generation from the acquired data to show the detection. During clutter removal, I-MUSIC uses subspace projection method based on singular value decomposition (SVD).

Let us assume the data in the scattered field is sensed by A different antenna pairs operating in bistatic mode (different antennas for transmitting and receiving RF waves) at N different frequencies. The acquired complex data is then organized in N rows and A columns in the matrix form and is transformed in **SVD**. The clutter is removed by discarding the projections relative to the two dominant singular values. After removing the clutter, we obtain the decluttered S_d matrix, and this matrix is the input for image generation (second step).

For the correlation matrix **R**, we calculate the eigenvectors and eigenvalues **[V, D]** for each frequency f. The correlation Matrix **R** is given as

$$\mathbf{R} = S_d^f.((S_d^f))^H \tag{3.1}$$

Where S_d^f=is the *fth* row of the *NxA* decluttered matrix S_d. Each pixel of the output image is than multiplied by an array of Green function W and are identified by row and column indexes *(u,v)*, through a Hermitian inner product of the dominant eigenvector V_{max} of **R**. These functions then model the propagation between antenna pairs *A* and the point in the scanned region corresponding to the pixel in question. To model the propagation, I-MUSIC uses a breast average dielectric permittivity, which can be computed by averaging the data of breast tissues from a large database [120]. For all *N* frequencies, function *F(u,v,f)*, which is the Euclidian norm of the Hermitian product is computed. Than all frequency components of *F(u,v,f)* are combined as

$$\prod_f (1 - F(u, v, f)^2$$

By taking the inverse of the above term, we get *P(u,v)* which contains the output image. It is important to note that the product of single frequency produces a kind of constructive interference, highlighting the actual tumor response and reducing spurious artifacts. For more details on the I-MUSIC equations we refer the reader to [81].

3.5 Standard hardware/software implementation of I-MUSIC

In MI systems RF components play an essential part. The overall cost, form factor, and portability of the imaging system depend upon these components. A current conventional imaging system such as X-Ray mammography, MRI, Ultrasound all have costly equipments and are very bulky and stationary imaging systems. The modern MI systems generally use costly lab equipment such as VNA to generate microwave signals to feed antennas and then receive the backscattered waves. Then the MI algorithms process the amplitude and phase of these input and output signals to generate images for detection purposes. These algorithms are typically software coded in a high-level programming language or in a Matlab script and executed in a general purpose processor. The figure 3.1 shows a conventional MI system, where a VNA is connected to the antennas (TX and RX) to transmit and receive microwave signals to and from a target (tumor). The target and the antennas are placed in a coupling medium to provide an environment similar to a practical clinical scenario, such that the coupling medium must have properties similar to female breasts. The angle between the antennas and their position is an essential factor to be considered in MI for tumor detection. In the above figure there are only two antennas, and for a complete scan of the tumor, either antennas or tumor have to be rotated. However, it is also possible to have a large switch system with many antennas around the breast where each antenna can be used as a transmitter and receiver, and for a practical system, this is the case. The VNA is then connected to a processing system having a graphical interface in which the software coded algorithm is processed, and the image is generated based on the amplitude and phase values of the signals.

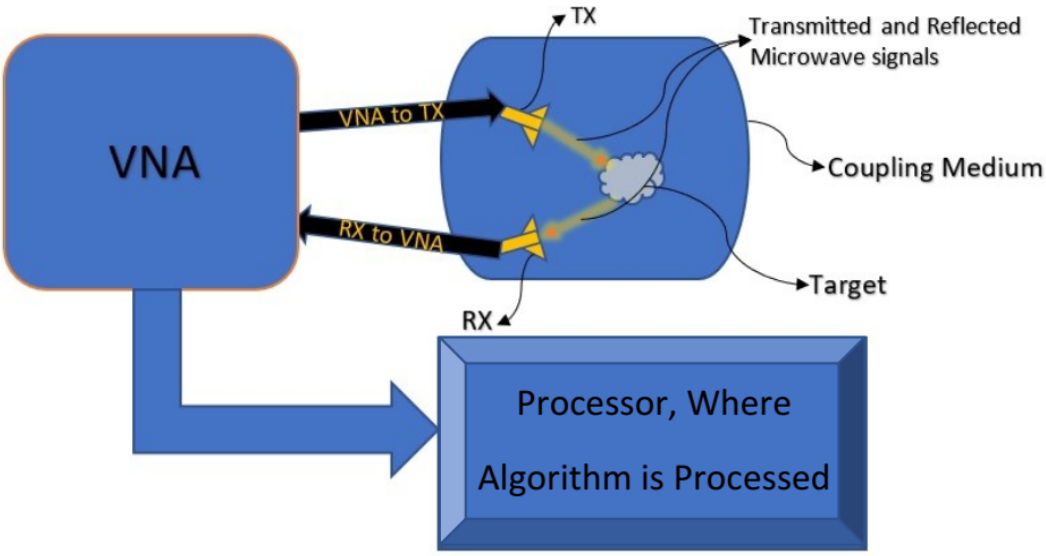

Figure 3.1: Conventional MI system.

The I-MUSIC algorithm has been coded in C language and is reported entirely in

Appendix A. This code is assumed to run in a standard MI system like the one sketched in figure 3.1.

3.6 Pros and Cons of the standard approach

The standard MI approaches have their own pros and cons, some of them are mentioned below.

Pros

- ⇒ Standard approaches are easy to use because they use standard CPU which are easy to program and they mostly have VNA which is flexible and easy to operate.
- ⇒ Abundance of references in the literature makes it easy to reproduce experiments.

Cons

- ⇒ Standard approaches are very slow in executing the imaging algorithm, hence they are time-consuming.
- ⇒ The equipments used consume a considerable amount of power.
- ⇒ Usually these equipments have a large form factor, hence not portable.

The combination of VNA with a standard CPU is not meant to be a definite solution, but it is rather a flexible and reliable set up useful in preliminary research or for a proof-of-concept. One possible evolution in a direction where portability, reliability, low power and speed are required is to develop ad-hoc integrated circuits (ICs). However, this will have a tremendous impact on the overall cost of the MI system. Fortunately, as we show later on, this is not necessary because existing commercial off-the-shelf (COTS) components can be used instead.

3.7 Our approach in solving the limitations of the standard approaches

To overcome some of the limitations of the standard approaches, we replaced the VNA and the processing system (generally a PC) with COTS components to generate microwave signals, to receive them, and finally to process them. Instead of developing new ICs as required by other MI techniques such as UWB Radar, we used commercially available low-cost components for this purpose. The other essential requirement is to have a processing system to run the algorithm and to generate images. For this purpose we replaced the standard PC with a Zynq SoC having an embedded FPGA. With this approach, we decreased the overall cost and size of our prototype without affecting its performance compared to the system operated with VNA and PC. The comparison of our MI prototype with the MI system operated with VNA is provided in chapter 5. I-MUSIC despite being faster than non-linear inversion algorithms, still requires CPU time which is not feasible for standard practical applications and the execution time is unacceptable if running on an embedded processor. The Use of Zynq SoC with an embedded FPGA helped us to speed up the execution time of the algorithm. The details of the components which we had used in our MI prototype is provided in next chapter.

3.8 Conclusion

In this chapter, we explained why we selected I-MUSIC as a good approach for the MI system instead of common UWB Radar and Tomography approach. We explained briefly the advantages of the I-MUSIC algorithm and the way it works for removing clutter and image generation. In this chapter we also explained what kind of components conventional imaging techniques and MI systems are using and what kind of problems, especially related to antennas can occur and how I-MUSIC algorithm deals with this problem.

Next chapter is related to the Microwave imaging system which we built. In that chapter, we will discuss the hardware of our prototype, software, the methodology which we adopted, designed hardware accelerator and the results of our prototype and their comparison to MI systems comprising of costly components.

Chapter 4

COTS-based Microwave Imaging System for Breast Cancer Detection

For our MI system, we adopted I-MUSIC [90-91] algorithm because it offers better flexibility compared to the other mentioned approaches. I-MUSIC does not require large bandwidth for its detection of the tumor (scatterer) and makes the imaging algorithm independent of antenna characterization. Numerical and experimental assessment of I-MUSIC using a Vector Network Analyzer (VNA) for breast cancer detection is in [91] where the authors have used a costly and bulky component like VNA and PC for processing the data. We followed a different approach for building an innovative MI system using low-cost off-the-shelf components. This approach is described in the following sections of this chapter. Since this is the result of a collaborative work, it is important to highlight what were my personal contributions as a PhD candidate to the construction and characterization of the COTS-based MI system. My contributions were as follows:

- Construction of the second version of the tank used for experiments (see section 4.5.2).
- Design and testing of the digital electronic interface and the software needed to

move the data from the data acquisition board to the Zedboard for data processing (see section 4.6).

- Implementation of the software for automating the measurements to run in the Zedboard (see section 4.7).
- Full implementation of the I-MUSIC software in the Zedboard and improvement of the FPGA hardware accelerator design (see section 6.3).
- Conception of the calibration method and its testing and characterization (see section 4.9).

4.1 System Architecture and Design

A detailed diagram of our designed prototype for breast cancer detection is in figure 4.1. This diagram is also helpful for understanding the main sections of the prototype and what function each part plays.

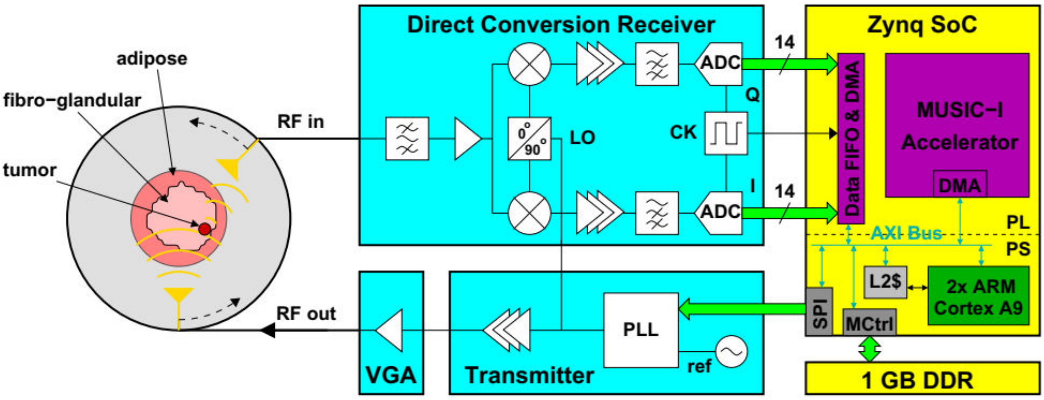

Figure 4.1: Schematic of the MI system.

Main parts of The Prototype

- Transmitter section.

- Receiver Section.
- Zynq SoC for controlling and processing.
- Measurement tank, containing breast phantom and wideband antennas.

4.2 Transmitting Subsection

One of the purpose of our prototype is to replace complex and costly equipments (e.g., Vector Network Analyzers) with low cost yet high precision off the shelf components. In the prototype, Zynq SoC configures the phase-locked-loop (PLL)-based transmitter (Tx), and for this purpose, we use the following components in the transmitting section of the prototype:

- 10 MHz Oscillator.
- LT DC590B PCI interface.
- LTC6946 N-synthesizer board.
- DC 1705B interface board.
- Voltage Controlled Amplifier
- UWB monopole Antenna(TX)
- Low Pass Filters

Our prototype has a working frequency of (1.4 GHz -1.6 GHz), and the RF signal is provided by a **10 MHz** oscillator by *Golledge Electronics Ltd*, in conjunction with **DC1705B** featuring the *Linear Technology* **LTC6946**. The LTC 6949 frequency synthesizer has a range from 0.37 GHz to 6.39 GHz with Integrated VCO, a phase-locked loop (PLL) with a fully integrated VCO, including a reference divider, a phase-frequency detector (PFD) with a phase-lock indicator, ultra low noise charge pump, integer feedback divider, and VCO output divider. The integrated low noise VCO requires no external components for its calibration and can be calibrated internally to the correct output frequency without any external system support. The 10 MHz oscillator is connected to the **DC 1705B** board and has a 50-Ω SMA connector for the reference frequency input, f_{REF}, the reference output buffer (REF OUT), and the differential RF output (RF+ and RF−). The two differential outputs (RF+ and RF−) are then used as input to transmitting antenna and as input to the local oscillator at the receiver board. RF+ is supplied to the antenna (Tx) through power amplifier connected in between transmitter antenna (Tx) and the LTC6946 boards RF output. The purpose of the amplifier is to raise the power level of the signal so that it propagates effectively in the mixture to breast phantom and is then backscattered so that the receiver antenna (Rx) senses these RF signals. The schematic of the transmitter section is given in figure 4.2.

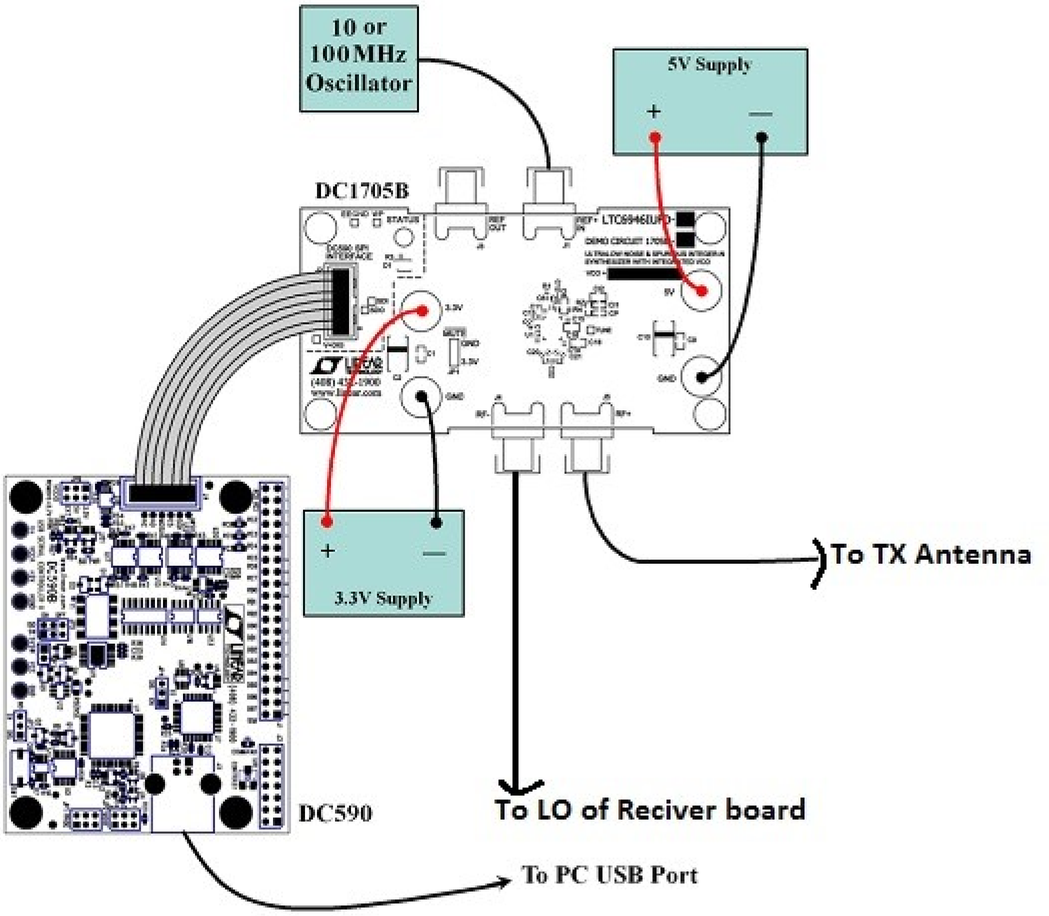

Figure 4.2: Transmitting subsection of the Prototype.
Source:
https://www.analog.com/media/en/dsp-documentation/evaluation-kit-manuals/DC1705CFB.PDF/

4.3 Receiver Subsection

Receiving subsection of the prototype consists of the following main components.

- UWB monopole Antenna (RX).
- Pre-amplifiers.
- Low Pass Filters.
- DC-Receiver LTM9004.

- Clock Signal Source

At the receiver side of the prototype, we are using 14bit direct conversion **LTM9004b** chip by *Linear Technology*. The backscattered signal from the breast phantom received by Rx is supplied to the input of the LTM9004b, through a pre-amplifier to raise the power level of the received signal. The use of a direct conversion (DC) receiver provides many advantages over the more common heterodyne approach [79], in particular:

- The DC receiver solves the requirement for RF front-end bandpass filters because it is not susceptible to signals at the image frequency. The only signals which RF bandpass filters must attenuate are strong out-of-band signals.
- DC eliminates the need for intermediate-frequency (IF) amplifiers and bandpass filters as the RF input signal is directly converted to baseband.
- The entire chain is DC-coupled and provides access for DC offset adjustment.
- Use of DC also provides comparatively better robustness to phase inaccuracies in the paths of the local oscillator. As a result, direct conversion performs better in terms of signal-to-clutter ratio as compared to the heterodyne approach [79].

The integrated on-chip broadband transformers provide 50 Ω single-ended interfaces at the RF and LO inputs. LTM 9004b is then connected to the demonstration circuit **DC1513**. DC1513 is an evaluation board featuring *Linear Technology Corporations LTM* 9004 **14-bit** direct conversion receiver subsystem. The DC1513b has three inputs: one is the RF signal from the antenna through filters and amplifiers, the other input is the local oscillator (LO) input from the transmitting boards (RF−), and the third input is the clock input from external frequency generator, required for sampling for analog to digital conversion. The sampled data is then sent via a USB-interface board to the Zynq SoC. LTM9004b removes the second-order nonlinearity of the receiver, generated by unwanted baseband signals and provides DC offset correction options. The DC offset can be corrected manually on the board by two separately rotatable terminals for each channel (I–Q). In our prototype, all the components are off the shelf except the low-cost custom printed antennas. Fig 4.3 shows a block diagram of the arrangement of our COTS-based system, whereas figure 4.4 shows a picture of it.

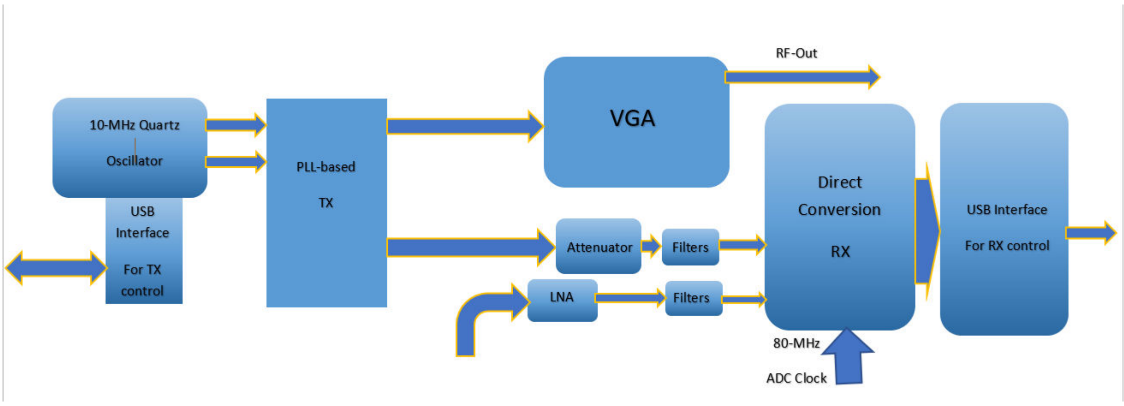

Figure 4.3: Blockdiagram of the COTS of Prototype.

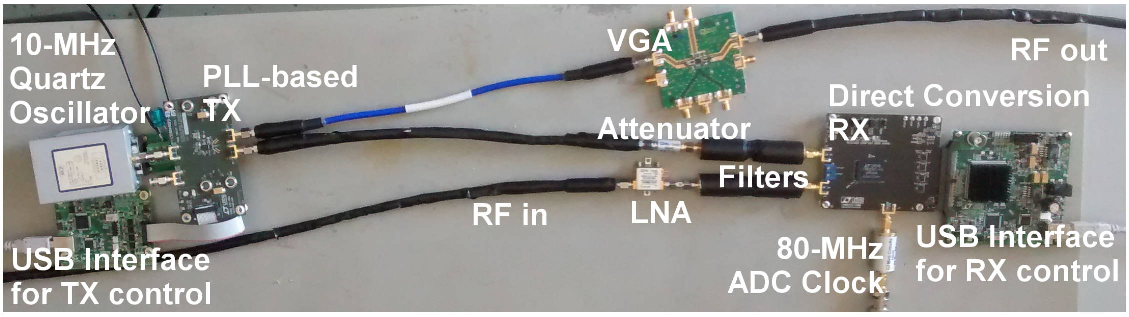

Figure 4.4: COTS of the Prototype.

The passive components on the Linear Technology boards used for both the transmitter and the receiver sections offer good 50Ω matching in the working frequency range (1.4 GHz-1.6 GHz) of the prototype (input return loss better than -10 dB). By default, the chips can cover a much larger bandwidth ranging from 0.37 to 5.7 GHz for Tx and 0.7 to 2.7 GHz for Rx. However, working on a wider bandwidth apart from bringing matching complication does not improve the detection performance, and this has been verified by comparing our results with that obtained from VNA working in the full bandwidth (0.5-3 GHz) discussed in the next chapter. Thus, we selected frequency range (1.4 GHz-1.6 GHz) with 200 MHz bandwidth for our experiments.

4.4 Measurement Tank with Coupling liquid and Antennas

To validate our approach and to test our MI system we designed a first test environment consisting of a cylindrical tank filled with a coupling liquid and in which we immersed various kinds of breast phantoms. To irradiate the phantoms and to collect the scattered field we used antennas immersed in the coupling liquid.

Antenna design is an essential aspect of microwave imaging. Traditionally, while designing antenna it is assumed that the antenna lies in the free space, but for the prototype, we designed antennas by considering the fact that, they will lie close to the breast in the near-field region. The other important issue while designing an antenna is its dimensions. In order to increase the number of antennas in a circular plastic tank of 10 cm diameter, it is crucial that geometrical dimensions must be kept as small as possible without affecting the performance. Our designed antenna shown in fig 4.5 is a wide-band monopole antenna with an SMA connector printed on a standard FR4 dielectric substrate. This technology helps in reducing the cost of antenna fabrication and the size of the antenna is reduced due to its flat shape. The designed antenna has good matching performance when immersed in the coupling mediums used during measurements. These coupling mediums are further explained in the following section. The geometry of the designed antenna is given in fig 4.6. The S11 parameters of the antenna (for 50 Ω reference) is also given in fig 4.5, obtained when the antenna is fully immersed in the coupling liquids.

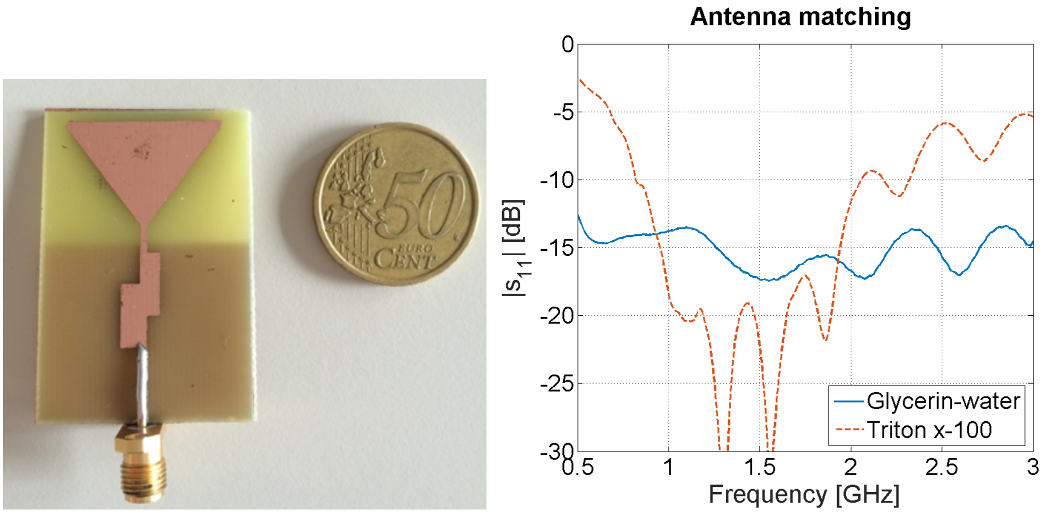

Figure 4.5: Designed UWB antenna and its S11 Parameter.

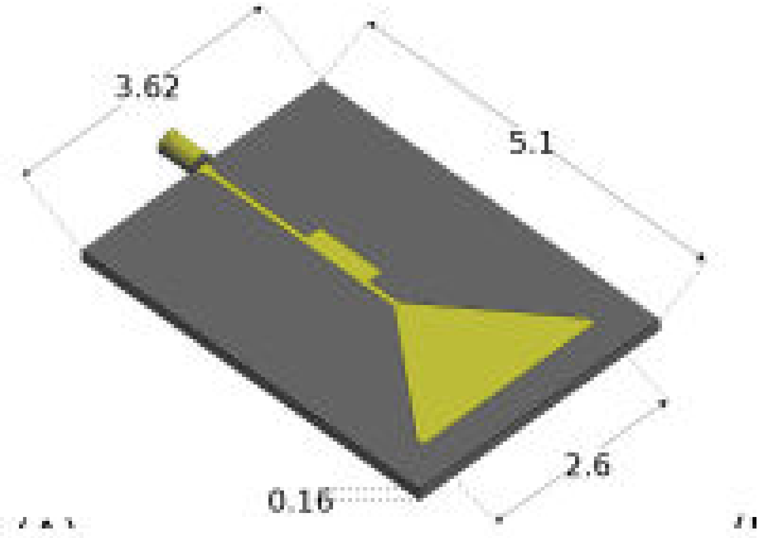

Figure 4.6: Geometry of the designed antenna (values are in cm).

The measurements are performed with two different coupling mediums having different dielectric properties. Both coupling liquids have been proposed in the literature [115][96].

The first coupling medium is the mixture of 80% glycerin [95], and 20% water with average dielectric value of permittivity ϵ_r=22. The second medium is Triton x-100 which mimics the dielectric characteristics of the 85-100% of the adipose tissue content of the normal breast tissue [96] in (0.5-3.0 GHz) frequency range and has average dielectric value of permittivity ϵ_r=7. Triton x-100 is a nonionic surfactant, also normally used as a detergent in laboratories and therefore easily supplied. Dielectric properties of both liquids are shown in fig 4.4 for the frequency range 0.5-3.0 GHz.

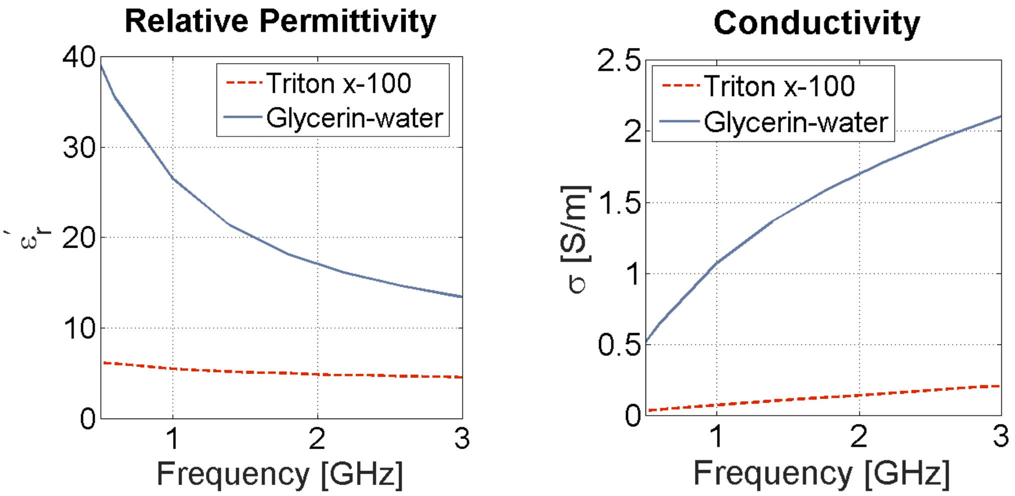

(a) (b)

Figure 4.7: (a) Relative Permittivity (b) Conductivity of the Coupling liquids.

We observed that the characteristics of the first coupling medium are stable over the time (the measured dielectric properties did not change even several weeks after creating the liquid blend), which clearly improves the repeatability of experiments. Since it is a mixture, however, it is difficult to reproduce it in exact proportions repeatedly. This mixture offers higher conductivity as shown in fig 4.7, hence, a higher signal attenuation, which is useful to eliminate the effect of multipath. Its attenuation also provides a good impedance matching for minimizing signal attenuation due to reflections at breast/liquid surface. The second coupling liquid, Triton x-100, is not a mixture which makes it simpler to use than the first medium (no need to blend).

Using these two significantly different coupling mediums in terms of dielectric values also helped us in validating that the our prototype MI system and the I-MUSIC algorithm can work in different scenarios that mimicked breasts having different dielectric values (low and high); the results reported in next chapter verifies this claim. Using these two coupling mediums and having satisfactory results in both cases also shows that the designed prototype is robust and quite insensitive to changes in the test environment.

For the prototype two different versions of the tank were used, which were designed for two set of experiments of increasing realism. The first tank was used with a 2D version of the breast and the tumor phantoms, whereas the second tank was used with a more realistic 3D version of the phantoms. The two versions are shown in figure 4.8 on the left and of the right picture, respectively.

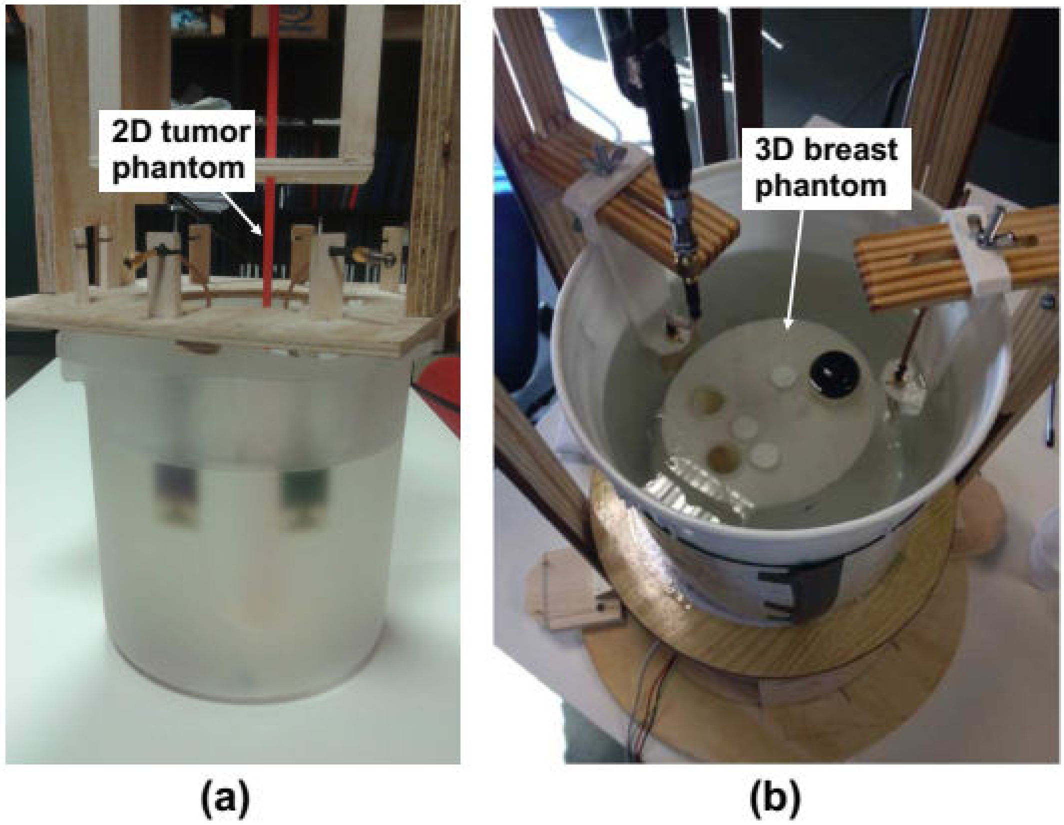

Figure 4.8: (a) First 2D version of the tank and (b) second 3D version of the tank, both filled with coupling liquids and breast phantoms.

In the first 2D setup, Tx and Rx antennas are mounted on a plexiglass support and placed in the tank filled with the mixture of glycerin and water. The antennas are placed along a circle of 20-cm diameter and the angle between the Tx and Rx antennas can be any multiple of 45^o. This is due to design constraints of the prototype shown in figure 4.8(a), which has 45^o-spaced holes in the plexiglass support. It is also important to mention here that the angle between the antennas is an important input parameter of the I-MUSIC algorithm and testing with different antenna angles also gives us an additional knob to evaluate the performance of the imaging algorithm. We used three different angles between the antennas in the measurements reported in the next chapter: 45^o, 90^o and 135^o. We kept the angle fixed during any complete measurement, therefore the results are reported for each individual angle.

In this 2D setup, a tumor phantom is represented by a metallic cylinder (mainly used as a control case) or by a hollow plastic cylinder with a very negligible thickness. The plastic cylinder is filled with a liquid, which could be different than the coupling medium liquid or the same (another control case). As shown in next chapter, these different liquids represent different scenarios of tumor of varying contrast to the surrounding medium. In this version of the tank, the cylinder can be placed at any position. Notice that the position of the scatterer inside the tank stresses the algorithm differently. A scatterer located close to the tank sides mimics a tumor located close to the breast skin, which is an adverse condition for the imaging algorithm because the information is concentrated across a limited number of scans. When the tumor phantom is around the center of the tank (away from skin), it is another adverse condition because now the algorithm needs to differentiate across a high degree of ambiguity. The exact location of the scatterer is crucial to evaluate the quality of the generated images and the detection capabilities, therefore it was carefully considered during the measurements.

Notice that a complete scan of the measurement scene is obtained by rotating a pair of antennas around the tumor rather than by switching between different antennas, which simplifies the measurement setup and avoids the use of a complex switch matrix. To further simplify the set up, instead of rotating the pair of antennas around the tank, a motor rotates the tank and the 2D tumor inside it in fixed angle steps, while keeping the antennas in the same position. This arrangement of rotating the tank makes the experiment in the laboratory simpler and rotating the phantom is equivalent to rotating the antennas. This setup also gives us much more flexibility than having a system with fixed position antennas. In order to eliminate or reduce external interference all the components and the tank were shielded with the help of aluminum foils during measurements.

The second setup of the tank is shown in fig 4.8(b), where to hold the antennas, we added two external wooden supports. This setup allows the movement along the z-axis in steps and makes it easy to change the angle between antennas. In the figure 4.8(b) the angle between Tx and Rx is 135^o and for this version of the tank, we used a full 3D breast-phantom whose details are explained in the next section. The motor is placed below the tank, and the whole tank containing the breast phantom is rotated. Similar to the first setup, antennas are at their original position during entire measurement while the tumor rotates and a complete scan of the phantom is recorded. Motor rotation in both setups is controlled automatically by the Zynq SoC and the IP to control the motor, as discussed in upcoming sections. We adopted the rotating arrangement in both versions of the tank to simplify our prototype. By eliminating the use of switch matrix for multiplexing Tx and Rx antennas in both versions of the tank, we reduced the measurement inaccuracies and minimized the cost of the prototype. However, for a clinical setting, this approach is not possible, because the patient cannot be rotated during measurements. In a clinical setting, the patient will lay still in prone position, and a tank attached with a motor and containing antennas will be placed under the patient breast. It is also possible in a realistic setup to rotate compact antennas around the breast. For 3D measurements, additional motors can be used for moving the antennas up and down.

4.5 Breast and Tumor Phantoms

Our prototype as discussed earlier has two different versions of the tank with different coupling mediums and tumor phantoms. These versions are explained below.

4.5.1 First Version of the Tank

In the first version of the tank (fig 4.8(a)), measurements are performed using 2D tumor phantoms. We used two different phantoms, one is a 12-mm diameter metallic cylinder and the 2nd is a 20-mm diameter plastic cylinder filled with a mixture of (i) 40% glycerin and 60%water, (ii) same mixture as of the coupling liquid and (iii) only water. Metallic tumor mimics a highly reflective tumor and it was used as a control case, whereas the other tumors offer much less dielectric contrast compared to the metallic tumor. Both the tumor phantoms have a length equal to the length of the tank. The antennas are at fixed positions and the tumors rotate with a step of 15^o (however this angle can be easily changed with Zynq SoC), and in total there are 24 measurement positions for a complete rotation. Although results reported in next chapter are for 24 steps, measurements were also performed with different steps and the results were the same in all considered cases (18, 24 and 30 steps), with no noticeable change in detection results. This number of steps is in accordance to the existing literature [81][91] but it is also important to mention here that thanks to the way the prototype is designed, it is easy to increase or decrease the number of steps or the rotation angle. The measurements and the results reported in the next chapter for this first tank refer to Tx and Rx antennas with an angle of either 45^o or 135^o between them, placed along a 20cm diameter circle.

4.5.2 Second Version of the Tank

In this version of the tank shown in fig 4.8(b), similar to the first version fixed antennas and phantom are placed inside the tank. In this case we experimented with the *GeePs-L2S* breast phantom [72][97], which we received in the framework of BMBS COST Action TD1301 “MiMed”, a project funded by European Union dedicated to the applications of microwave imaging in the field of medicine. The GeePS-L2S is a 3D breast model, fabricated with a 3D printer. In this breast model, fibrograndular, adipose, and tumor, the three different tissues are represented by three different parts of the 3D breast phantom as shown in fig 4.9. Each part is filled with a liquid mimicking the dielectric properties of the corresponding tissue [97] which are obtained by a proper mixture of water, salt, and Triton X-100. The conductivity and permittivity of the breast are reported in fig 4.9 (a) and (b).

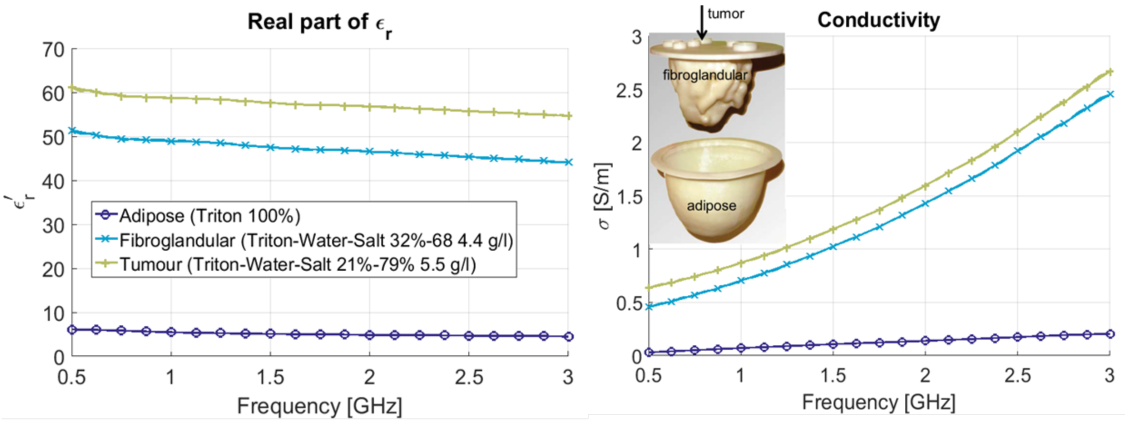

(a) (b)

Figure 4.9: GeePs-L2S phantom, (a) Permittivity and (b) Conductivity of the liquids, mimicking the breast tissues.

The 2D horizontal cut of the GeePs-L2S phantom is given in fig 4.10. The cut corresponds to the plane of tumor detection by I-MUSIC algorithm and also shows the position of Tx and Rx.

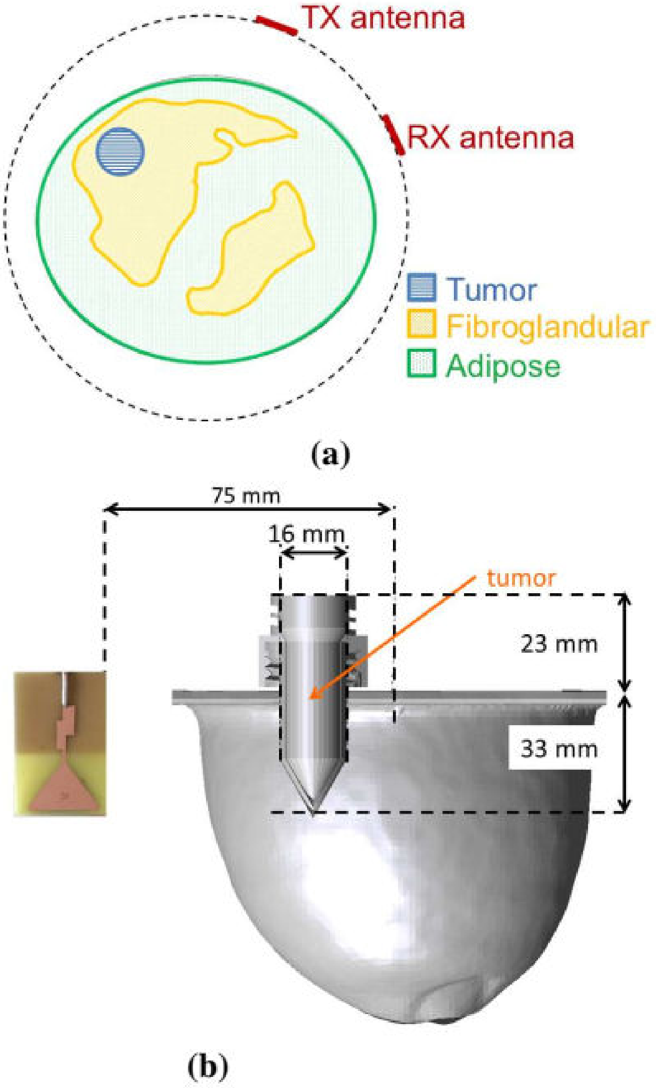

Figure 4.10: GeePs-L2S breast phantom: (a) horizontal cut in the antenna plane; the outer circle represents the rotation path. (b) Cross section view showing tumor size and position. The antennas can be placed at any vertical position.

In this tank we used Triton X-100 as a coupling medium because it has the dielectric properties of an "average" breast. The antennas are placed at a 15-cm diameter circle, so as to surround the breast phantom at a shorter distance than in the previous tank. The angle between Tx and Rx antennas can be 45^o, 90^o, or 135^o, as described before. The motor rotates with a 15^o step, and there are total 24 positions to record the measurements. In figure 4.10 (a) the path of the rotation of the antennas is shown by dashed lines and the shape of the three tissues is represented by different patterns similar to their actual shape inside the 3D breast phantom. Tumor with a diameter of 16mm is located inside the fibroglandular tissue, which represents an adverse condition for detection because the dielectric contrast between them is **1.2:1**, which is very less compared to the contrast between fat and tumor which is **11:1**. The cross-sectional view of the 3D breast phantom is given in figure 4.10(b), which also shows the position of antennas relative to phantom and they are located at 75mm distance from the center of phantom near the upper part. With this version of the tank, it is also possible to perform 3D measurements, because the height at which antennas are placed can be changed easily. The tank with both versions of the coupling liquids and all the components are shielded from external interference by placing components in a metallic box and by a metallic foil around the tank enclosing antennas, tumor and coupling liquids.

4.6 Vivado and Zedboard

For controlling the transmitter, receiving the digital complex data from the digital receiver, storing them and then running the I-MUSIC algorithm on the acquired data to generate results, we are using Zynq SoC mounted on the Zedboard board. Zedboard is an evaluation and development board based on the Xilinx Zynq-7000 Extensible Processing Platform.

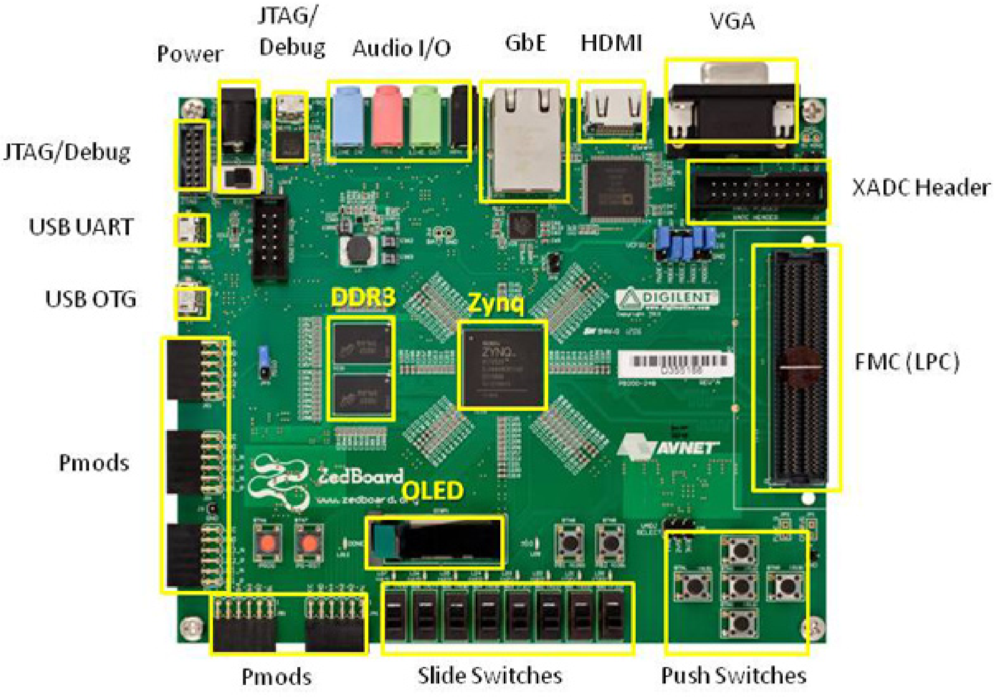

* SD card cage and QSPI Flash reside on backside of board

Figure 4.11: Zedboard (Evaluation and Development board). source:http://zedboard.org/product/zedboard

The Zynq combines both applications processor and FPGA fabric due to which its features, capabilities, and potential applications are different from a processor or an FPGA in isolation. The Zynq-7000 All Programmable SoC (System on Chip) has a dual-core ARM Cortex-A9 processing system and hard peripherals coupled with Xilinx 7-Series 28 nm programmable logic, all integrated on a single SoC. The internal clock frequency of the processing system is 667 MHz. Its memory consists of 512 MB DDR3 RAM, a 256 MB Flash Quad-SPI and a 4 GB SD card. Figure 4.11 shows the labeled diagram of the ZedBoard and position of its main components such as the Zynq processing system, power supply, RAM, USB, JTAG, push button. Further details about the Zedboard can be found in [84].

In order to design for Zynq we used the **Vivado Design Suite (2016.3)** available at Xilinx website and from it installed ***Vivado IDE*** and ***SDK***. Both are very important as they provided the bases for designing hardware and software respectively [113] for our MI system. A short description of both of these is provided here for understanding their importance.

Vivado IDE

Vivado is an integrated development environment (IDE) where the hardware system part of the SoC design is created, i.e., processor, peripherals, memories, external interfaces, and bus connections. In Vivado IDE reusable hardware blocks called Intellectual Properties (IPs) can be developed and packaged for later reuse . Packaging IP is an important facility offered by Vivado IDE because it broadens the possibilities for design reuse and creating new IPs according to the requirements.

SDK

The Software Development Kit (SDK) based on the popular Eclipse platform is a software design tool. It includes driver support for all Xilinx IPs, GCC library support for ARM using the C++ and C languages, and tools for debugging and profiling.

An outline of the design flow for designing hardware and software using ***Vivado IDE*** and ***SDK*** is given in the figure 4.12.

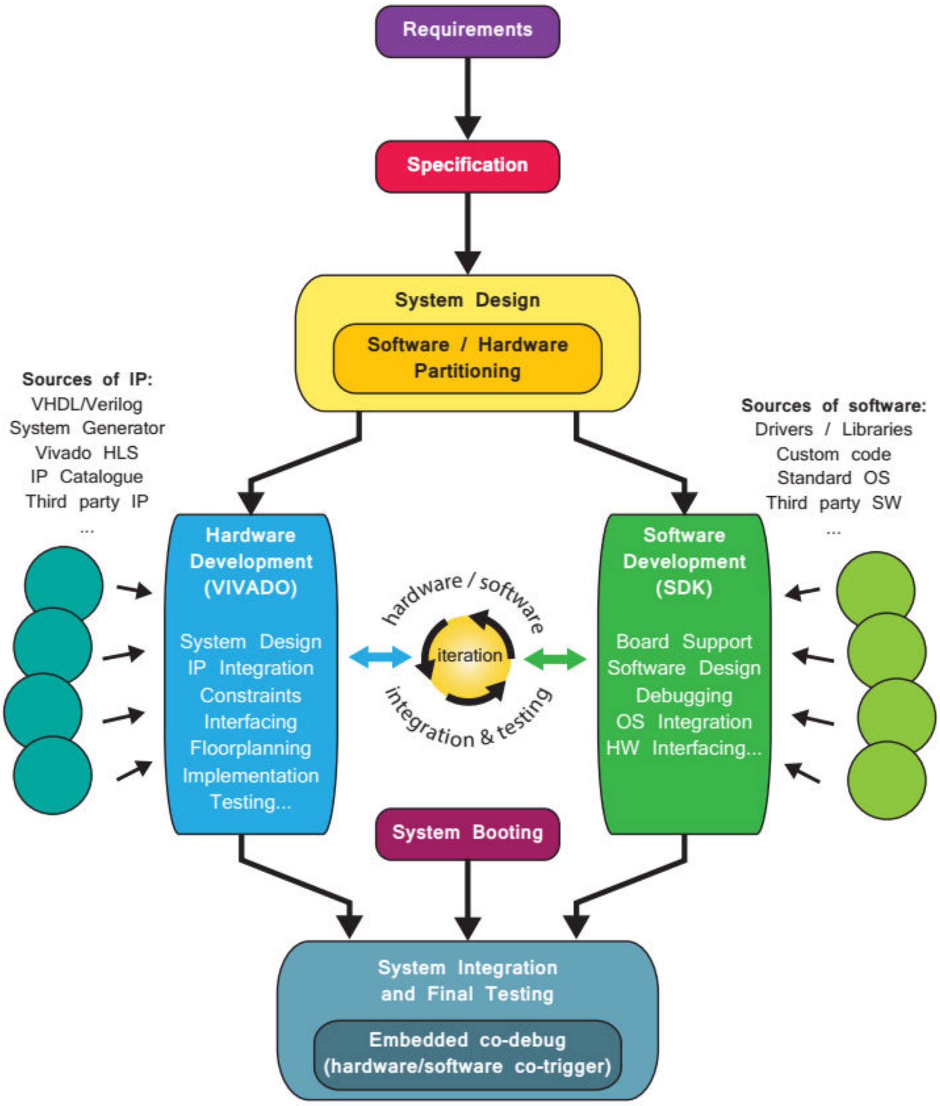

Figure 4.12: Zynq SoC Design flow.
source:http://www.zynqbook.com/download-book.php

Further details about the design flow for Zynq SoC in Vivado IDE and SDK readers can find in [114][83-85]

4.7 Vivado Project for the MI system

A project using the ***Vivado IDE*** design tool has been created, and the I-MUSIC algorithm written in **C** is compiled and executed on the ARM processor using ***SDK***. ***SDK*** (Software Development Kit) is also included in the Vivado design suite and can be launched within the Vivado IDE environment. For the prototype, we designed an embedded system in Vivado by adding a ZYNQ7 processing system block and other necessary IPs. We also created custom IPs using Vivado IP manager, whose function is to receive the data coming from the DC receiver and storing them into the DRAM of the Zynq SoC in I and Q form. This data is then inputted to the I-MUSIC algorithm for generating the image. Block diagram of the project containing all the essential IPs necessary for the processing system is given in figure 4.13.

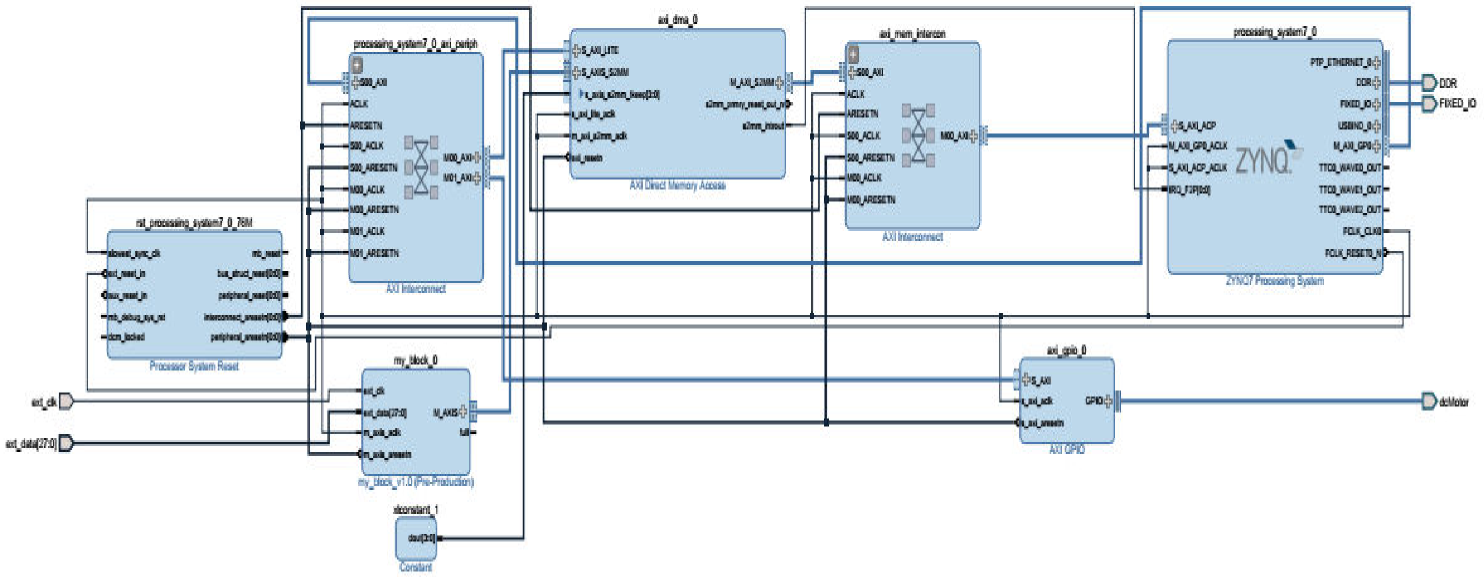

Figure 4.13: Vivado Project for MI system.

In the above figure two essential IP blocks ”**my_block**” and “**dcmotor**” are custom made IPs, which we created for three important functions. The IP block ”**my_block**” shown in figure 4.14 performs two important functions: first it receives the output of the DC receiver for processing in the imaging algorithm, and our designed accelerator which is described in next section for accelerating the imaging algorithm is also inside this IP. The other IP “**dcmotor**” (figure 4.15) automatically rotates the dc motor, which in turns rotates the tank (in which breast phantom and tumor are present). With this IP the bucket is rotated automatically after specified time interval, when the data is acquired at a particular position for the complete frequency range. This makes our prototype completely autonomous, and data is acquired for a complete rotation of the tank and is stored in DRAM for processing.

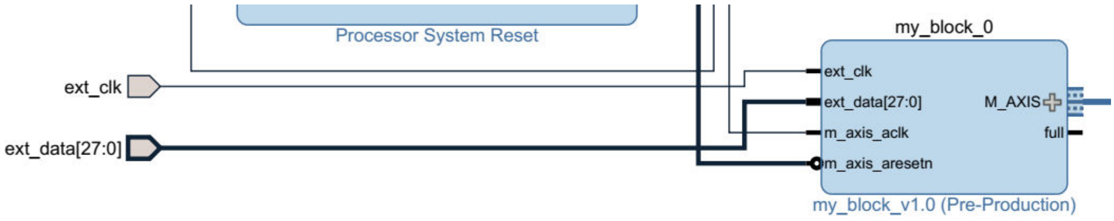

Figure 4.14: IP for acquiring data from DC Receiver.

Figure 4.15: IP for Rotating the Tank.

Dc motor is rotated at an angle of 15^o and for a complete rotation **24** steps are needed. At each of the 24 positions, data is acquired for each of the 11 discrete frequencies and frequency of the output RF is updated automatically after a fixed time interval (to store I and Q components for each 11 discrete frequencies) in the steps of 200 MHz.

4.8 FPGA-Based Digital Back End

Our goal of designing the prototype is to have an imaging system, which is low-cost and portable compared to other MI systems. The Xilinx's Zynq SoC plays the most crucial role in achieving our goal. It integrates into its dual-core ARM processor chip, a level 2 cache, various standard peripherals and is denoted by a processing system (PS) with an Artix-7 FPGA denoted as programmable logic (PL) shown in figure 1. During measurement at every antenna position and for each frequency, data is acquired in the form of (I & Q) samples by the DC receiver, and then these 14bit samples are sent in the source-synchronous mode to the Zynq SoC using the IP block "my_ block" discussed earlier. The data is first buffered in a FIFO implemented in PL part of the Zynq, and then the buffered samples are transferred via DMA to the external DDR memory. Before processing the received samples, they are averaged for reducing the noise. After that, the decluttering phase and eigenvalue computation are performed for each frequency. The computational bottleneck is in two loops where Green functions and Hermitian products are evaluated. It is important to notice that for each pixel of the image in a 2D slice, kernel code of the loops is repeated and if multiple scans are performed along the z-axis, then the execution time would be the number of scans multiplied by execution time. In a clinical application the execution of these loops in a pure software environment is not a feasible solution because the time it will take to execute the algorithm to produce results will be longer, hence not acceptable for practical applications; therefore we decided a hardware acceleration for these loops is a good choice. We implemented the hardware accelerator in the PL part of the Zynq. The remaining part of the algorithm runs in the software in ARM processor, while the accelerator and ARM processor communicates via DMA. The accelerator is defined in behavioral SystemC and by using commercial High-Level Synthesis (HLS) tool we obtained its RTL description. RTL description is the entry point of the Xilinx FPGA design flow. With the help of the HLS tool, we validated in about four months more than 100 design alternatives. We obtained these alternatives due to the application of parallelism, loop unrolling, pipelining and other design knobs, starting from a single high-level description. We ranked all the accelerator solutions based on the performance in terms of the execution time and the one with least execution time was selected. Final accelerator which we selected is shown in figure 4.16.

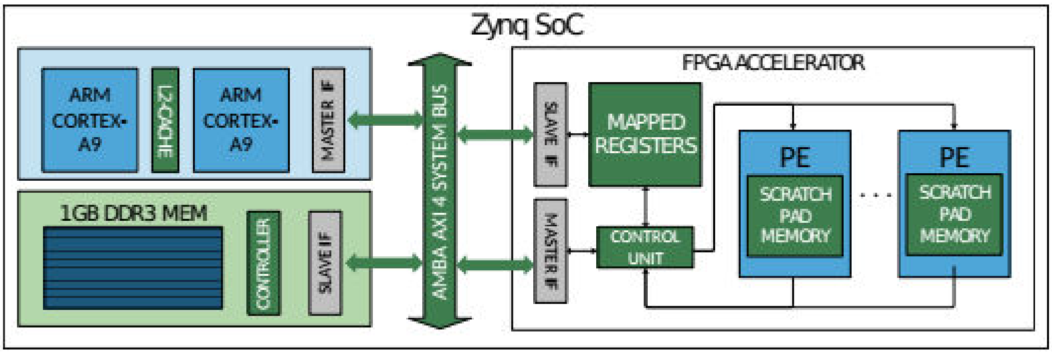

Figure 4.16: Implemented Accelerator in Zynq SoC for computing I-MUSIC.

Our designed accelerator consists of identical **processing elements (PE)**. These PEs are operating in parallel each on the row of the image. Using HLS for each complex operations such as square root, division, trigonometric functions etc. which these PEs execute, we obtained a high performance, pipelined implementation. In the accelerator, we pipelined computation and communication in such a way that the communication between accelerator and processor does not hold the computation and we do not waste a single clock cycle. The designed accelerator has the bus-master interface for DMA data transfers and two bus-slave interfaces for status and commands information. As our goal behind the prototype is to have high performance while minimizing cost and form-factor, we synthesized the maximum possible number of PEs that could fit on the Zynq. To check the performance of our prototype, we compared the execution time of the prototype with a server-class Intel multicore (Xeon E5-2653 @ 3.3 GHz, 64GB RAM). The Intel multicore completed the execution of a 2D scenario in around **20s** while the designed accelerator completed the execution in less than **1s** independent of the input data. With our accelerator, we obtained more than 20× speed-up compared to software execution. From these results, we can estimate that for a 3D scenario the overall measurement time will reduce from (20-30) minutes to only a few minutes which is acceptable for a clinical application.

4.9 System Calibration

Our prototype uses components off the shelf and DC receivers often introduces offset issue due to LO leakage [98] and second order non-linearities. For a better understanding of these issues let us consider the given below schematic of DC conversion receiver.

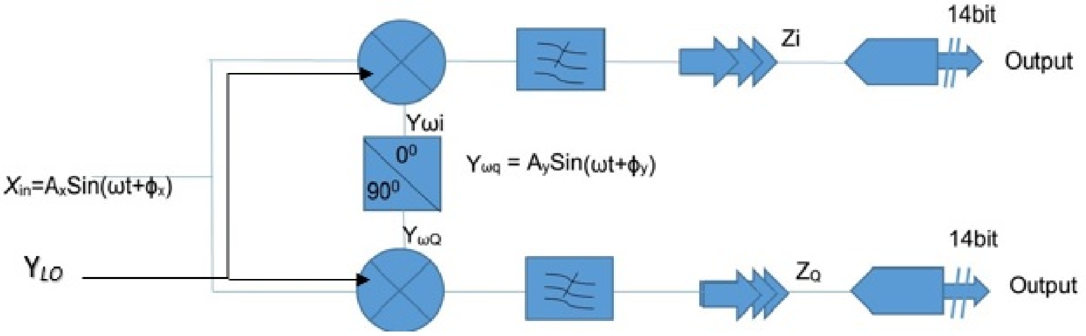

Figure 4.17: Direct Conversion receiver structure.

Let us assume that input signals to RF and LO of the receiver have the same frequencies, i.e. $\omega_{X_i} = \omega_{Y_{LO}}$. Note that in the calculation terms involving x are those which are due to the input signal, y are those which are due to local oscillator signal, if a term involves r then it means these are the terms related to reference signal (when transmitter is directly connected to the receiver input RF with a known attenuation) while m denotes the terms related to measured values. Considering only offset and second-order-linearity, and taking into account that terms at frequencies ω and multiples are eliminated by the low pass filters in Fig. 4.17, than the overall response of the receiver to these factors is given by the equation 4.1.

$$\begin{aligned} Z_I &= G_I \frac{A_x A_y}{2} cos(\phi_x - \phi_y) + \delta_{Ix} \frac{A_x^2}{2} + \delta_{Iy} \frac{A_y^2}{2} + \gamma_I \\ Z_Q &= -G_Q \frac{A_x A_y}{2} sin(\phi_x - \phi_y) + \delta_{Qx} \frac{A_x^2}{2} + \delta_{Qy} \frac{A_y^2}{2} + \gamma_Q \end{aligned} \tag{4.1}$$

where G is the gain of the amplifier in the respective sides (I & Q), the δ terms are related to 2nd order non-linear errors, while γ term is related to offset errors. A_x, A_y are the amplitudes of the RF and LO signal while ϕ_x and ϕ_y are their respective phases. In the above equation the terms A_x, A_y and others involving x and y together with G_I and G_Q are the useful terms due to input signal (albeit possibly affected by gain errors due to the difference between I and Q gains, if any).

Equation 4.1 tells us about all the factors which can possibly affect the performance of the prototype. To reduce these inaccuracies, we devised an analytical procedure to identify these factors and then took the necessary steps for their possible compensation.

4.9.1 Offset compensation

To compensate for the offset let us consider $X_{in} = 0$ and $Y_{in} = 0$ in equation 4.1, the equation will be simplified as

$$\begin{aligned} Z_I &= \gamma_I \\ Z_Q &= \gamma_Q \end{aligned} \tag{4.2}$$

These values do not depend upon the frequency and can be compensated by the adjustment of I&Q terminals in the receiver board.

4.9.2 Non-linearity Determination

To know the factors which are responsible for the non-linearity, let us first set LO signal Y_{in} different then zero and the input signal from the antennas equal to zero. i.e $Y_{in} \neq 0$, $X_{in} = 0$. Because the offset is already compensated the equation can be now written as,

$$\begin{aligned} Z_{I\omega} &= \delta_{Iy}\frac{A_y^2}{2} \\ Z_{Q\omega} &= \delta_{Qy}\frac{A_y^2}{2} \end{aligned} \tag{4.3}$$

These values do not depend upon the input signal from the transmitter but depend only on the LO signal. Therefore they are constant at a given frequency and can be fully compensated during the processing phase.

4.9.3 Non-linearity due to input signal X_{in}

The non-linearities due to input signal is determined when $Y_{in} = 0$, and $X_{in} \neq 0$.

$$\begin{aligned} Z_{Ix} &= \delta_{Ix}\frac{A_r^2}{2} + \textbf{Compensated terms} \\ Z_{Qx} &= \delta_{Qx}\frac{A_r^2}{2} + \textbf{Compensated terms} \end{aligned} \tag{4.4}$$

Notice that to determine the terms due to non-linearity, we apply as input signal a reference signal of amplitude A_r.

4.9.4 Characterization with reference signal

For the reference signal, equation takes the below form after compensations

$$\begin{aligned} Z_{Ir} &= G_I\frac{A_rA_y}{2}cos(\phi_{xr} - \phi_y) + \textbf{Compensated terms} \\ Z_{Qr} &= -G_Q\frac{A_rA_y}{2}sin(\phi_{xr} - \phi_y) + \textbf{Compensation terms} \end{aligned} \tag{4.5}$$

Assuming that the difference of I and Q gains is negligible, i.e. $G_I = G_Q = G$ then the above equation can be simplified further as

$$\begin{aligned} Z_{Ir} &= G\frac{A_r A_y}{2} cos(\phi_{xr} - \phi_y) + \textbf{Compensated terms} \\ Z_{Qr} &= -G\frac{A_r A_y}{2} sin(\phi_{xr} - \phi_y) + \textbf{Compensated terms} \end{aligned} \tag{4.6}$$

The magnitude and phase of the non-linear terms due to reference signal are given by $G\frac{A_r A_y}{2}$=$\sqrt{Z_{Ir}^2 + Z_{Qr}^2}$ while the angle is given by $(\phi_{xr} - \phi_y) = -\arctan\frac{Z_{Qr}}{Z_{Ir}}$

All the above-calculated terms are essential in calculating the overall transfer function of the system due to non-linearities.

4.9.5 Transfer Function of the System

Assuming linearity, the response of the system at a given frequency ω to an unitary excitation is given by $H \exp^{j\phi H}$. This response in terms of magnitude and phase, our system needs to obtain similar to what a VNA would obtain. Equation below shows how we can obtain it from the measured Z_{Im} and Z_{Qm}. By considering that the X input to the receiver is now replaced by the reference signal multiplied by the transfer function H, equation 4.1 can be rewritten as follows.

$$\begin{aligned} Z_{Im} &= G\frac{A_r H A_y}{2} cos(\phi_H + \phi_x - \phi_y) + \delta_{Ix}\frac{H^2 A_r^2}{2} \\ Z_{Qm} &= -G\frac{A_r H A_y}{2} sin(\phi_H + \phi_x - \phi_y) + \delta_{Qx}\frac{H^2 A_r^2}{2} \end{aligned} \tag{4.7}$$

replacing $G\frac{A_r A_y}{2}$ by α and $\delta_{Ix}\frac{A_r^2}{2}$ by b_I and $\delta_{Qx}\frac{A_r^2}{2}$ by b_Q and putting $(\phi_H + \phi_x - \phi_y) = \theta$ the equation simplifies to

$$\begin{aligned} Z_{Im} &= \alpha cos(\theta) H + b_I H^2 \\ Z_{Qm} &= -\alpha sin(\theta) H + b_Q H^2 \end{aligned} \tag{4.8}$$

Having determined b_I and b_Q after the characterization with the reference signal, we can solve this equation algebraically to obtain the magnitude H and the angle θ, and from θ we can obtain the angle ϕ_H. An approximated but still accurate result can be obtained by neglecting b_I and b_Q. Even though in general the system of equations 4.8 can be solved to get the values of b_I and b_Q, we found out that these two terms are negligible in the receiver board which was used in the prototype. As a result, the equation 4.8 after neglecting the mentioned two terms can now be written as follows:

$$\begin{aligned} \phi_H &= -\arctan\frac{Z_{Qm}}{Z_{Im}} - \arctan\frac{Z_{Qr}}{Z_{Ir}} \\ H &= \frac{\sqrt{Z_{Im}^2 + Z_{Qm}^2}}{\sqrt{Z_{Ir}^2 + Z_{Qr}^2}} \end{aligned} \tag{4.9}$$

Notice that the compensation of offset and non-linearity has to be performed at different frequencies. The behavior of the system reference signal and offset with respect to the considered frequency range is in figure 4.18. The given offset behavior in the figure is obtained after performing a partial offset compensation with the help of the terminals available at the receiver board at the starting frequency (1.4 GHz). Measured values of offset for each frequency are given in Table 4.1.

For the reference, measurement values are given in Table 4.2. The values that are obtained here are not just γ_I and γ_Q, i.e., the offset values when both Ax and Ay = 0, but when the local oscillator (LO) is active ($Ay \neq 0$); therefore they also include the terms δ_{Iy} and δ_{Qy}.

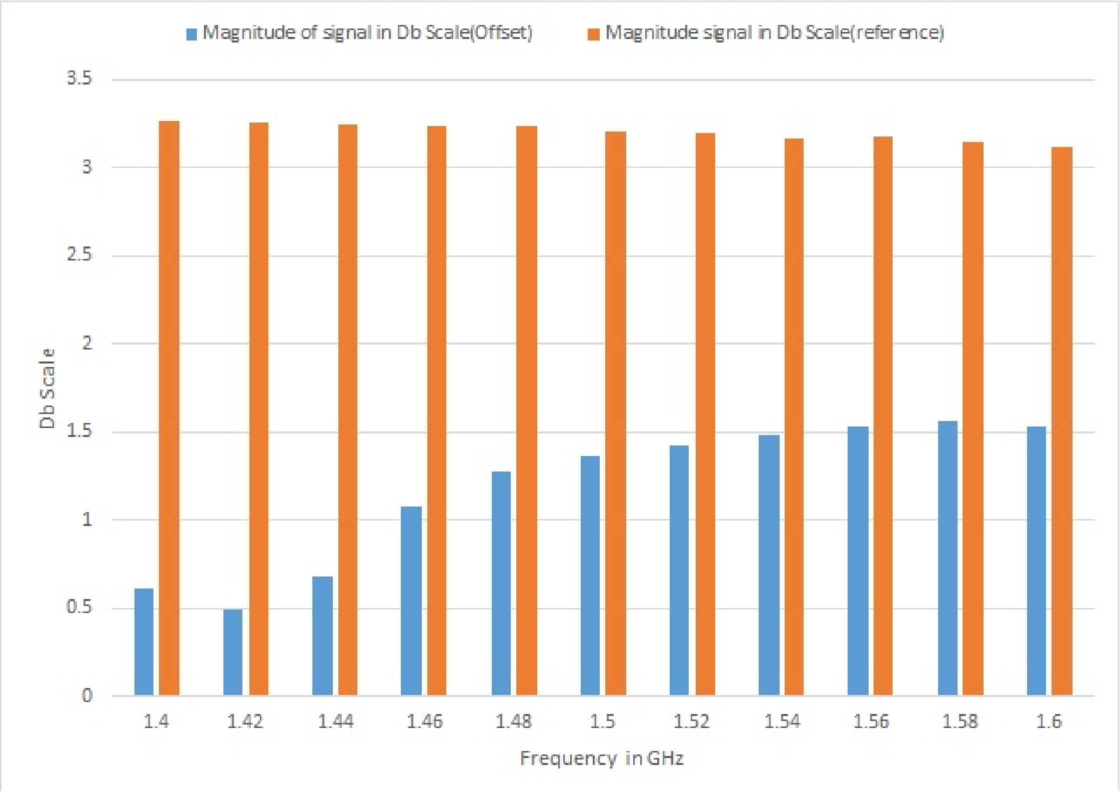

Figure 4.18: Behavior of Offset and Reference Signal with Frequency.

Table 4.1: Behavior of offset with frequency.

Freq(GHz)	I-Component	Q-Component	Magnitude of Offset	Offset in dB Scale
1.40	-0.7	4	4.06	0.608
1.42	1.5	-2.7	3.08	0.489
1.44	-3.5	-3.2	4.742	0.676
1.46	-11	-4.4	11.847	1.0736
1.48	-18	-6.2	19.038	1.28
1.50	-22	-7.7	23.308	1.37
1.52	-25	-8.8	26.503	1.42
1.54	-27.8	-11.5	30.084	1.48
1.56	-30	-15.4	33.72	1.53
1.58	-29.4	-21	36.13	1.56
1.60	-22.5	-26	34.38	1.536

Table 4.2: Behavior of reference signal with frequency.

Freq(GHz)	I-Component	Q-Component	Magnitude of Reference	Reference in dB
1.40	745	1685	1842	3.26
1.42	-1526	-970	1808	3.25
1.44	1742	12	1742	3.24
1.46	-1484	892	1731	3.23
1.48	782	-1506	1969	3.23
1.50	101	1611	1614	3.2
1.52	-948	-1264	1580	3.19
1.54	1353	554	1462	3.16
1.56	-1471	217	1486	3.17
1.58	1066	-928	1413	3.15
1.60	-420	1221	1291	3.11

From the above figure 4.18 and tables 4.1 and 4.2, we can say that when frequency is changed during measurement, the values of offset are also changed, and their effect must be subtracted during post processing, because they can affect the image. However, change in frequency does not affect the reference signal much and its response is almost constant throughout the measurement.

4.10 Conclusion

In this chapter, the developed MI prototype is described in detail. All the essential parts of the prototype, their characteristics, and their dependence on different factors which can affect their performance is discussed. In this chapter we discussed in detail the coupling mediums which we used and the two measurement setups of the prototype. In the chapter, we also discussed the designed accelerator required to speed up the execution time of I-MUSIC. In the chapter, factors which can affect the performance of the prototype are analyzed, and their behavior with respect to frequency is observed,

and then the steps required to minimize the effect of these errors from the final generated image are also proposed.
In the next chapter, the results of our measurements performed with the prototype and their comparison with a MI system operated with VNA and PC is provided.

Chapter 5

Experimental results of the COTS based Microwave imaging prototype

In this chapter the results of our experiments performed with our built prototype are given. The tank of the prototype, which contains the breast phantoms, and the antennas can be connected to a broadband **Vector Network Analyzers (VNA)** or to our **components of the shelf (COTS)** based Microwave Imaging system. This flexibility allows us to compare our COTS-based prototype with a standard system consisting of VNA and CPU. We obtained results by running the I-MUSIC algorithm with the data acquired with the VNA and with our prototype. When we conducted experiments with our system, we acquired data of the backscattered field between the frequency range of 1.4 GHz to 1.6 GHz in 200 MHz step. We selected this range, because the board with the DC receiver has the best matching for this range. When conducting measurements with the VNA, we acquired data in the same bandwidth for a fair comparison, but we also acquired data between 0.5 and 3.0 GHz which is the full bandwidth where our antennas are matched ($|S_{11}| \leq -10$ dB) (figure 4.5). This gives us two crucial measurement advantages: first by doing this, we can compare our system with the VNA and evaluate its accuracy; the other advantage is by comparing our results with 0.5 to the 3.0 GHz range we can assess that there is no loss of valuable information when considering only the

1.4-1.6 GHz range. In the previous chapter, we explained that our prototype has two versions of tank one with the mixture of **Glycerin (80%)** and **(20%) water** while the other tank is filled with **Triton X-100**. Experimental results obtained with both versions and their comparison with VNA is discussed in the next sections of this chapter.

Before acquiring the real measured data, compensation for offset and non-linearities for each experiment was performed. This was done according to the procedures mentioned in chapter 4 section 4.9 from the actual measured data. Then, images are obtained by running the I-MUSIC algorithm on the acquired data obtained after compensation subtraction. As a control case for checking the prototype, measurements were performed using the metal as tumor and the prototype was able to efficiently detect the tumor. When the prototype detected the tumor easily measurements were performed in different scenarios using both version of the tank (explained in previous chapter), these results are provided below.

All the experiments and measurements described in this chapter of the thesis were personally conducted by the PhD candidate.

5.1 Results Obtained with a Mixture of Glycerin (80%) & Water (20%) as Coupling Medium (1st Version of the Tank)

5.1.1 Tumor Cylinder filled with same liquid as of coupling medium

In the first version of the tank before filling the tumor cylinder with the mixture (40% Glycerin and 60% water) we filled it with the same liquid as of the coupling medium (80% Glycerin and 20% water). This is a control case because theoretically, since there is no contrast between the tumor and the coupling medium, there should not be any detection (the plastic cylinder is transparent in the frequency range considered). The measurements with prototype and with the VNA were performed under same conditions and with the same arrangement of the tank. The images obtained by running the I-MUSIC algorithm on the data acquired by the VNA and our prototype are in figure 5.1.

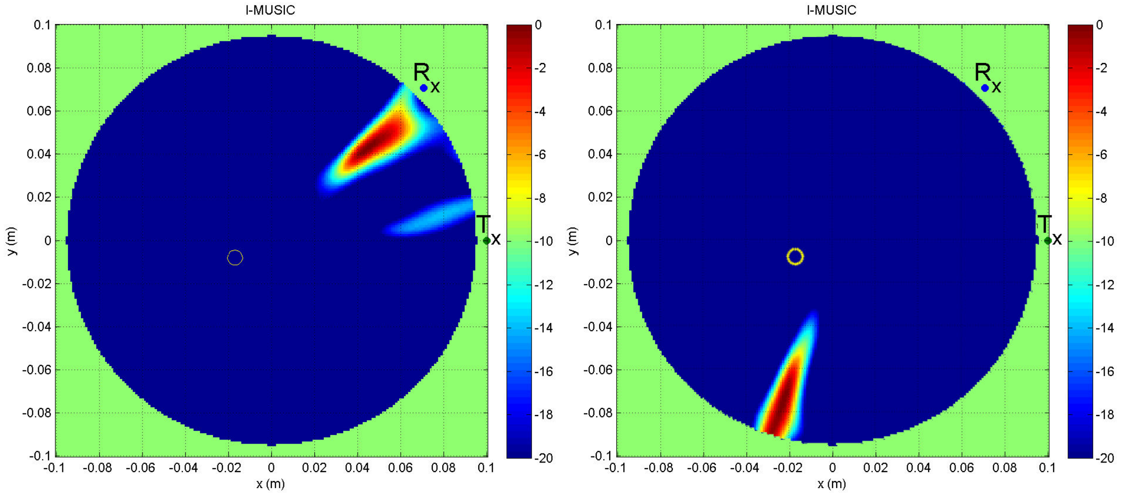

(a) Generated Image obtained with COTS-Based MI System. Colorbar unit is dB.

(b) Generated Image obtained with VNA. Colorbar unit is dB.

Figure 5.1: Tumor phantom same as the Coupling Medium.

The images in figure 5.1 are plotted in the plane transversal to the tumor cylinder with origin at the center of the tank. The image corresponds to a scanned circular area of 10-cm radius, therefore it has a width and length of 10 cm on each side (x and y) from origin. Rx and Tx in figure indicate the receiver and transmitter antennas respectively. In the image, the yellow circle shows the actual position and size of the tumor, while colored shades highlight the scattering points detected by the algorithm. For a successful detection by the algorithm the detected scattered points and the yellow circle needs to be overlapped, or at least they must be in close proximity of each other. In the images the unit of colorbar is in dB normalized to the highest value.

The result in figure 5.1 is in accordance with our expectations, as there is no detection in or around the yellow circle. Notice the similarity between the two cases in terms of exhibiting an artifact (albeit at different locations) and not detecting the cylinder at the predefined location (yellow circle) in figures 5.1(a) and 5.1(b), which shows that both our prototype and the VNA behave quite similarly in this situation. The two images are different in terms of location of maximum (artifact) but this behavior was random when the measurements were performed in this condition (same tumor and coupling medium liquid). Sometimes the images obtained were very clean (i.e. no artifact), and sometimes with different location of maximum. The exact reason for this random behavior in this condition is difficult to predict but it could be due to noise and antenna mismatching. The ambiguity of the scene that theoretically has many degrees of symmetry when there is no scatterer certainly plays a role in determining an almost random location of the artifact.

5.1.2 Tumor Cylinder filled with water

In this case, we filled the tumor cylinder with water while the coupling liquid is same (80% Glycerin and 20% water). Water and the coupling liquid have very high dielectric contrast (4:1) between them, and the prototype should detect the tumor easily. By running the acquired data under this condition in the I-MUSIC algorithm, the generated image is in figure 5.2 (colorbar unit is dB).

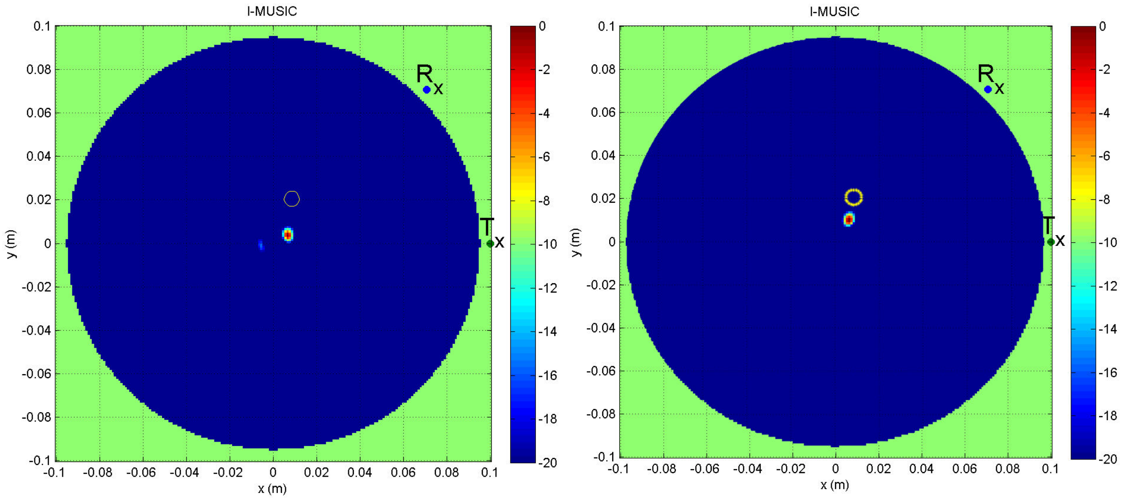

(a) Generated Image obtained with COTS-Based MI System. Colorbar unit is dB.

(b) Generated Image obtained with VNA. Colorbar unit is dB.

Figure 5.2: Tumor Cylinder filled with water.

Constructed images with the prototype and with the data acquired from VNA have similar detection. The slight difference (2mm on y-axis between the scatterers) in the detection position could be due to the movement of the tumor inside the tank because the tumor is a very thin plastic cylinder and can be easily twisted. However, the important thing here is the similar behavior of our prototype and VNA.

5.1.3 Tumor Cylinder filled with mixture (40% Glycerin and 60% water) and Metallic Rod as tumor phantoms

After the successful detection in previous cases we tested our prototype with different cases and compared the results of our chosen range with the full range of the VNA. In the figure 5.3, the results obtained with the prototype are compared with the VNA in the subrange (1.4 GHz to 1.6 GHz) and full range (0.5-3.0 GHz). Angle between the Tx and Rx is 135^o, different from previous cases as we tried different possibilities of the antenna arrangement. In the figure below images from (a) to (c) are obtained when the tumor phantom was a metallic cylinder, while in the images from (d) to (f) tumor phantom was a cylinder filled with the mixture (40% Glycerin and 60% water). By analyzing the figures and comparing the results obtained with VNA for both ranges to the image obtained with the prototype, we can easily say there is no significant loss of the information, and the results are very similar. Our system has successfully detected the tumor phantom and there is a negligible shift of the detection position when the tumor inside the tank is a metallic rod. Notice that this can be considered a control case because the metallic cylinder offers the highest contrast being totally reflective.

In the 2nd case when the tumor phantom is the mixture of (40% Glycerin and 60% water), the angle between Tx and Rx is 45^o again. Also in this case, the results obtained with the prototype are in complete agreement with the results obtained with VNA for both ranges. Based on these initial results it is safe to say that our prototype is as efficient as VNA for detecting the tumor and the frequency range which we selected is producing reliable results and there is no noticeable effect on the performance of the prototype.

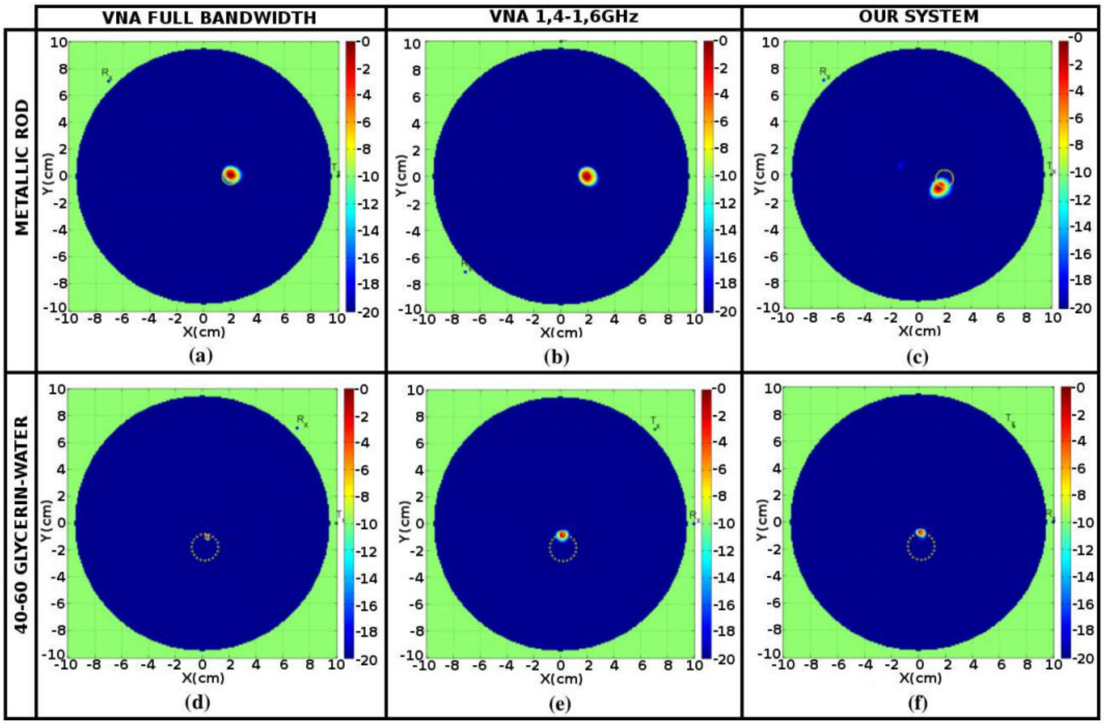

Figure 5.3: Images obtained with I-MUSIC, (a)-(c) 12-mm metallic target, (d)-(f) 20-mm cylinder filled with 40%-60% glycerin-water mixture. (a) and (d) obtained with the VNA, full bandwidth; (b) and (e) obtained with the VNA, 1.4-1.6 GHz; (c) and (f) obtained with our system. Colorbar unit is dB.

5.2 Results Obtained with Triton X-100 as Coupling Medium (2nd Version of the Tank)

In this version of the tank, **Triton X-100** is used as a coupling liquid, and the **GeePs-L2S** is the breast phantom. In this measurement setup with both VNA and prototype, the angle between the Tx and Rx is changed after a complete scan of the tumor. Data is acquired when the angle between the antennas is 45^o, 90^o and 135^o (reasons explained earlier) due to the fact that the prototype is designed in such a way that the space between antennas can be a multiple of 45^o. Figure 5.4 reports the results obtained on the acquired data under these conditions.

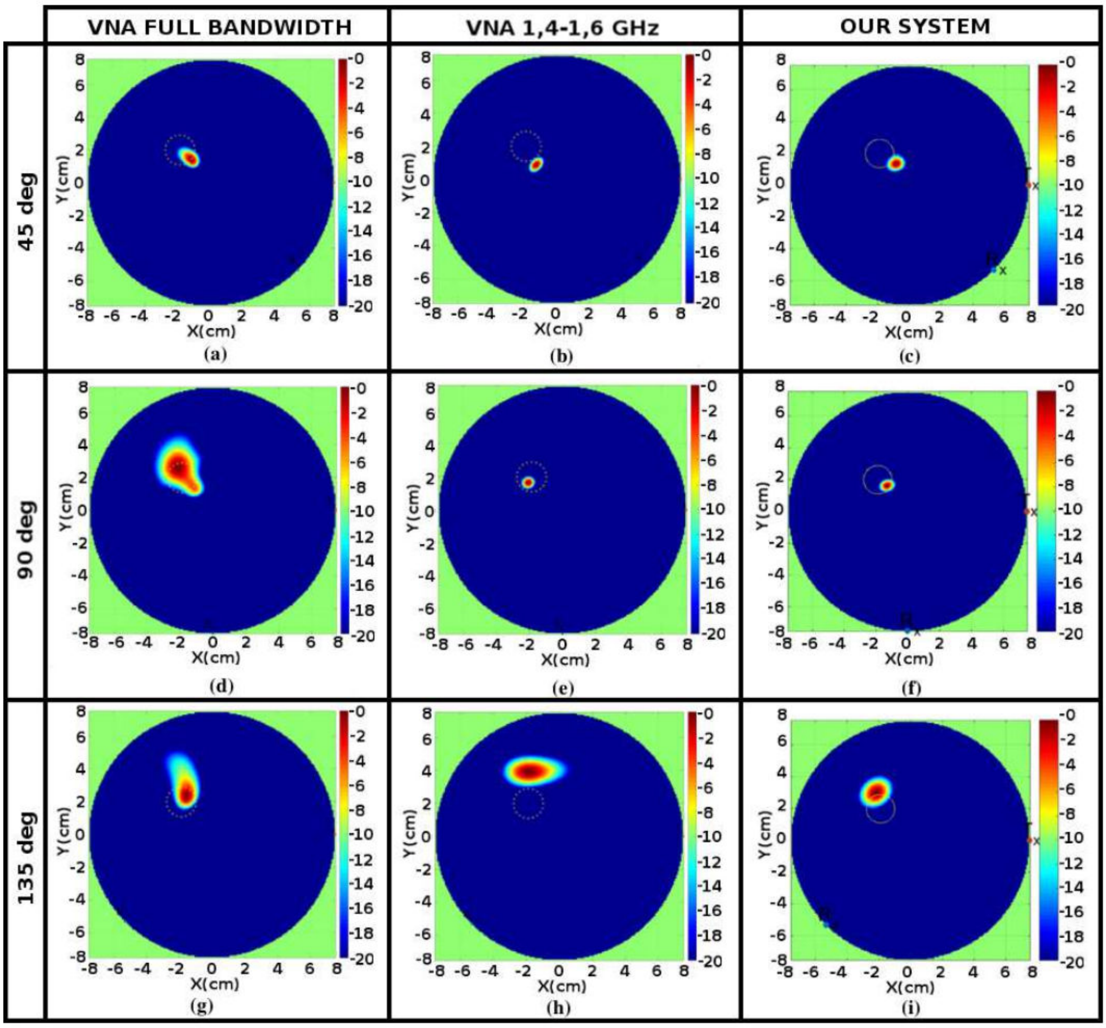

Figure 5.4: Images obtained with I-MUSIC using the GeePs-L2S breast phantom; the angle between the TX and RX antennas is 45^o in the first row (a-c), 90^o in the second row (d-f), and 135^o in third row (g-i); in the first column (a,d,g) the VNA is used in the 0.5-3 GHz range; in the second column (b,e,h) the VNA is used in the 1.4-1.6 GHz range; in the third row (c,f,i) our system is used in the 1.4-1.6 GHz range. Colorbar unit is dB.

In the figure first two columns are the results with VNA in the full bandwidth and the (1.4-1.6 GHz) range, while in the 3rd column results obtained with the prototype are given. The above figure is a good representation of an actual scenario because the image reconstruction is affected by some delocalization, which in turn depends on the angle between the Tx and Rx antennas. Please notice that working at 45^o is best because at this angle the delocalization is less and same is the case for 90^o with VNA and the prototype and the behavior is same for both. When the angle between the antennas is 135^o the behavior is again same for both but there is less localization and it can be due to multi-path because the signal has to travel more and probably it will go from more paths and the dispersion is more in this case as compared to the others. We can say that this localization problem is due to the result of the unavoidable model mismatch between the equivalent permittivity of the I-MUSIC algorithm (i.e. the breast average dielectric permittivity) and the actual breast dielectric profile, antenna angles, and multipaths. However, the important thing is our COTS-based system has detected the tumor. These results are very encouraging because the dielectric contrast between the tumor and surrounding fibro-glandular tissue is very low (1:2:1) and the fact that a tumor is somewhat hidden by the fibro-glandular tissue, as shown in figure 4.9(a). The above result is also a functional verification of the suitability of the frequency range which we selected. If we compare the results of column 1 with column 2, we can observe that the results obtained under full range with VNA are worse then the results obtained with 1.4 GHz-1.6 GHz range, as the detection in full range is not much focused compared to the other range and is due to the fact that the signal in the upper frequency range is affected by noise, which ultimately results in worse performance.

For each case of figure 5.4, a comparison of the results obtained with VNA and by our system is shown in table 5.1. In this table, the signal-to-mean (SMR) ratio, which is the ratio of maximum value of backscattered energy in the tumor region to the average energy in the whole image, and the signal-to-clutter (SCR) ratio, which is the ratio of maximum value of backscattered energy in the tumor region to the maximum value found elsewhere in the image, are given. SMR and SCR are the standard metrics to evaluate how good the detection is by comparing signal to clutter and signal to mean. An ideal system would detect a peak as a maximum surrounded by a null background with no clutter, which would result as infinite values for both metrics. As a general rule of thumb, we can assume that at least 30 dB are needed for a clear detection. Now, almost all the values in table 5.1 meet this criterion, with the exception of the VNA in the full frequency range. This is in accordance with the qualitative results in figure 5.4, in which the VNA at full bandwidth performs worse than both the VNA and the COTS-based prototype in the 200-MHz range centered around 1.5 GHz. Notice that SMR and SCR metrics do not indicate if the detection occurs in the exact location or slightly off. Therefore we obtain high SMR and SCR values even if the detection occurs slightly offset with respect to the yellow circle indicating the exact location. Nevertheless, the results in figure 5.4 show that both the VNA reference and the COTS system are equivalent as far as precision of peak location is concerned, which is a consequence of limited precision in determining the exact tumor and the antenna position, slight changes in the coupling medium permittivity, and I-MUSIC model errors.

Table 5.1: SMR AND SCR OBTAINED WITH THE GEEPS-L2S BREAST PHANTOM IN A TRITON COUPLING MEDIUM, VARYING THE ANTENNA ANGLE.

VNA full bandwidth			**VNA 1.4-1.6GHz**		**Our System 1.4-1.6GHz**	
Angle (deg)	**SMR (dB)**	**SCR (dB)**	**SMR (dB)**	**SCR (dB)**	**SMR (dB)**	**SCR (dB)**
45	47.8	30.4	52.0	29.4	53.8	32.7
90	30.7	28.4	56.3	92.9	55.6	68.0
135	36.8	41.1	34.9	38.9	42.4	57.1

The quantitative metrics of the detection are generally higher for the COTS-based system as compared to the VNA. However, for the case when the angle between Tx and Rx is 90 degree these values are better for VNA, especially the SCR metric for which we obtained an exceptional value od 92.9 dB. There is no apparent reason for this exceptional result and we tend to believe that it was a lucky case with an extremely peaked maximum with small clutter, as it is evident from the very small clutter around the peak in figure 5.4(e).

5.3 Conclusion

In this chapter, we presented the results obtained with our COTS-based MI system. The results are also compared with VNA for different versions of tank, tumor, coupling medium, and antenna angles and in each case results of the prototype were comparable to the results obtained with VNA. These results are very encouraging and based on these results we can say that the built prototype is comparable to an MI system using a VNA. The results reported here are obtained when only one scatterer was inside the tank. We also performed measurements for the cases when two tumors were placed inside the tank, however, the results were not consistent and in the final image the detection was mostly misplaced due to which those results are not reported here.

Our prototype is very fast in producing results thanks to the hardware acceleration and the execution time is improved by 20x compared to high-end multicore CPU. Our COTS-based system is compact because it uses very few and smaller components and most importantly our prototype is cost effective because the components used are commercially available and are very low in cost, their cost is negligible when compared to a MI system with VNA.

Chapter 6

Acceleration of a Microwave Imaging Algorithm for Brain Stroke Monitoring

Research groups who had worked on MI for brain stroke, mostly have worked on developing MI algorithms specific to brain stroke or on their numerical evaluation [103-106] or implementation of prototypes [108-109]. Continuing our work on the application of MI for breast cancer detection we believe that most of the concepts which we had already used to design the prototype for breast cancer detection and discussed in previous chapters can be applied to brain stroke monitoring. Due to the availability of the commercial off-the-shelf components which we had already used in our prototype for breast cancer detection, we are very confident that it is possible to build a MI subsystem to monitor the brain stroke and keep the overall cost and size of the brain stroke monitoring low without affecting its performance. However, at the time of writing this dissertation the hardware prototype for brain stroke monitoring is still under development and we cannot report results obtained on actual measurements performed in the laboratory on the full system.

However, a part of this prototype system is complete already, and is the digital system in charge of accelerating the imaging algorithm that shows the evolution of the brain stroke. Therefore we will present in this chapter the design of this system and the results of acceleration of the imaging algorithm. We will show how we implemented the microwave imaging algorithm in a programmable system-on-chip with an FPGA for acceleration, similar to the one used for breast cancer detection. We will show how we managed to reduce the execution time by more than five times compared to the software implementation of the same algorithm in an ARM CPU. The speed of execution as well as the small form factor and weight of the hardware makes our system suitable for bedside monitoring.

Due to the lack of full-system measurements at this stage of the project, the input data for the accelerated imaging algorithm are obtained from numerical electromagnetic simulations. Notice, however, that the performance of our digital system is independent on the quality of the input data. Therefore the reported results are representative of a realistic case.

The imaging algorithm which we are using in this MI system for brain stroke monitoring is different from the imaging algorithm (I-MUSIC) used for the breast cancer detection. With I-MUSIC the goal was to detect the presence of the tumor by finding the point in the scene that scatters the most the incident field because of a dielectric contrast (e.g. tumor vs healthy tissues surrounding it). For brain stroke monitoring, instead, the goal is to monitor the evolution of the stroke area by determining small changes in the dielectric properties of the scene between two different measurements. For this application we use an imaging algorithm based on the Truncated Singular Value Decomposition (TSVD) [104] approach.

Before describing the digital system that we designed for accelerating the TSVD algorithm we give a description of the MI system that we are building and give some details on how the imaging algorithm works.

Notice that this is a collaborative work, therefore it is important to highlight what were my personal contributions:

- C++ software porting for the Zynq programmable SoC of the TSVD algorithm described in section 6.2 (code reported in Appendix B).
- FPGA hardware implementation of the digital accelerator for the TSVD algorithm described in section 6.3.
- Experimental results described in section 6.4.

6.1 Brain stroke Monitoring via Microwave Imaging

Essential requirements of an MI system, especially for stroke monitoring, are portability and low power consumption. To achieve these goals, we are designing an MI prototype based on COTS, using the same approach followed for the brain cancer detection application. At the present stage of the project we developed the programmable system-on-chip with an FPGA for accelerating the imaging algorithm, which can produce images in a negligible time for a quick evaluation of how the stroke is evolving. Even though the rest of the system is under development, we will now illustrate the system architecture that it is currently developed, which corresponds to the scenario that we used to obtain the electromagnetic numerical simulation results with which we feed the imaging algorithm.

6.1.1 The Layout of Microwave Imaging System for Brain Stroke Monitoring

The block scheme in figure 6.1 shows the five main parts of the MI system for brain stroke monitoring that is currently under development:

- A helmet which contains the antennas.
- A switch matrix for routing the transmitted and received RF signals.

- A Vector Network Analyzer (VNA) or equivalent equipment (e.g. a COTS-based, custom-built one) for transmitting and receiving signals.
- Dedicated hardware for processing the acquired data for monitoring.
- A display for showing the reconstructed image.

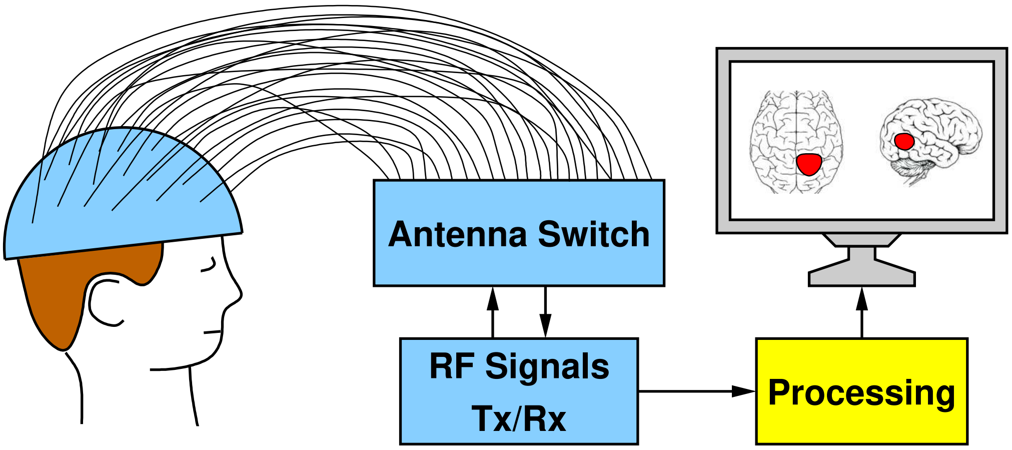

Figure 6.1: MI system composed of a helmet with 24 antennas, the equipment to transmit and receive RF signals, a switch matrix to route these signals to the antennas, and the processing unit for the image elaboration.

Inside the helmet, there are a number of antennas for transmitting (Tx) and receiving (Rx) the microwave signals. These antennas are arranged in an array and are placed around the head at the upper part of the head and provide uniform irradiation to the patient’s head, as shown in figure 6.2. Due to the physical dimensions of the antennas (3cm×4cm wideband monopoles in FR4 substrate), we planned to insert up to 24 antennas in the helmet. This number is obtained also taking into account that the helmet will hold a matching medium inserted between the antennas and the head at a 2.5-cm distance with the help of a holder and a plastic membrane. The coupling medium will be a mixture of water and Triton x-100, with proportions determined in such a way to favor the penetration of the microwave signal inside the head at a frequency of 1 GHz

[104]. The number of antennas and their layout around the head given in figure 6.2 provide an acceptable trade-off between stability, accuracy, spatial resolution for the image reconstruction, hardware complexity and overall cost of the system.

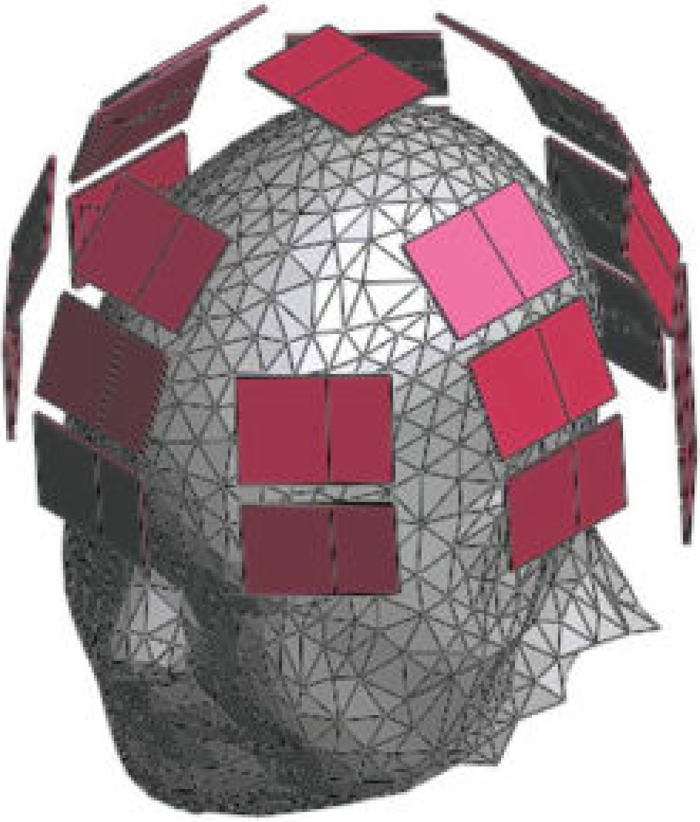

Figure 6.2: Arrangement of the antennas around head.

The antennas in the array can act as transmitter and receiver and are connected through the switching matrix to an equipment for RF signal generation and acquisition. At first, a VNA will be used for transmitting and receiving the signals due to its efficiency and easy of use. The ultimate goal, however, is to replace the VNA with COTS similar to those used in the prototype built for breast cancer detection.

The switching matrix is designed in a way that the signal generated by the transmitter is routed to one antenna at a time to act as Tx while keeping the remaining antennas as Rx. A controller controls the switch matrix in such a way that at a given time only one of the antennas acting as Tx and one acting as Rx are simultaneously connected to the transmitter/receiver pair or the VNA in bistatic mode. The scattering parameters are obtained from the ratio between received and transmitted microwave signals. These scattering parameters are then converted from magnitude-phase representation into complex numbers with real and imaginary parts.

For a complete scan of the head, all antennas are configured iteratively as transmitters (Tx), and receivers (Rx) one by one and 24X24 signals are recorded which means the reflection captured by the transmitting antenna is also recorded. When the head is wholly scanned, the scattering parameters are recorded in a textual format as a 24x24 matrix. This file is then used as an input to the imaging algorithm for image reconstruction.

It is again stated here that the system is in its initial stages and the results shown next are based on the data obtained from electromagnetic numerical simulations without including the noise. The goal here is to accelerate the imaging algorithm for brain stroke monitoring based on the data obtained in a collaborative work with the authors of [104].

6.2 MI imaging algorithm for brain stroke monitoring

The goal of the imaging algorithm implemented in the MI system is to detect the variations between two instances of the measurement, i.e., corresponding to two different monitoring times and so two possibly different extensions of the stroke area, as determined for instance by the effect of a medical treatment. To achieve this goal, we used a differential imaging algorithm that uses as input the difference between the scattered field recorded at two different times. The idea is that the dielectric contrast between the stroked area and the healthy tissues around it changes over time, and by sensing this difference we can image the area affected by the stroke.

More in detail, the algorithm senses these variations as a change in dielectric contrast $\Delta\chi$, which results in variations ΔE_S of the scattering matrices recorded at two different instances of time. These dielectric variations affect a volume of minimal size compared to the total volume of the investigated scene (i.e. the whole brain), which is supposed not to change between measurements. With this assumption the distorted Born approximation can be adopted [110], and the imaging problem can be linearized as:

$$\Delta E_S\left(\boldsymbol{r}_p, \boldsymbol{r}_q\right) = L\left(\Delta\chi\right) \tag{6.1}$$

where L is a linear and compact integral operator and relates the differential data $\Delta E_S\left(\boldsymbol{r}_p, \boldsymbol{r}_q\right)$ to the unknown $\Delta\chi$.

$\left(\boldsymbol{r}_p, \boldsymbol{r}_q\right)$ are the positions of transmitting and receiving antennas, respectively.
In the above equation kernel of the L operator is given by $-j\omega\epsilon_b/4 * \boldsymbol{E}_{\mathrm{b}}\left(\boldsymbol{r}_m, \boldsymbol{r}_p\right)\cdot\boldsymbol{E}_{\mathrm{b}}\left(\boldsymbol{r}_m, \boldsymbol{r}_q\right)$, where $\boldsymbol{r}_m$ is a point in the head, which is the region of interest (ROI), and $\boldsymbol{E}_{\mathrm{b}(\boldsymbol{r},\boldsymbol{r}_p)}$ is the "background" electric field radiated in each point $\boldsymbol{r}$ of the ROI by the antenna located at $\boldsymbol{r}_p$ when $\Delta\chi(\boldsymbol{r}) = 0$.

To solve linear inverse problems, such as the one in Equation (6.1), the singular value decomposition (SVD) of L is generally used as an initial step [110]. An effective and regularized inversion strategy is to use a truncated SVD (TSVD) of the operator L, for avoiding error amplification and reaching a stable solution.

Let $\mathbf{S} = \{\sigma_n\}$ be the singular values of L, which we obtain using a reference head model [104].

$\mathbf{U} = \{u_n\}$, and $\mathbf{V} = \{v_n\}$ are the vectors of its singular functions, where $\mathbf{U}$, and $\mathbf{V}$ are complex numbers.

The unknown differential contrast $\Delta\chi$ in each point $\boldsymbol{r}$ of the ROI is obtained as:

$$\Delta\chi(\boldsymbol{r}) = \sum_{n=1}^{m} \frac{1}{\sigma_n} < \Delta E_S, u_n > v_n(\boldsymbol{r}), \tag{6.2}$$

In the above equation $< a, b >$ is a dot-product between vectors and m is a threshold corresponding to the index at which TSVD summation is truncated. $\mathbf{V} = \{v_n\}$ is the basis for the object space, i.e., the space of the unknown of the imaging problem. Because TSVD limits the object space to the one spanned by first m singular function, for improving the accuracy one might use a threshold as large as possible. However, doing this can lead to error amplification, which means a low value of m is a preferable choice for the stability of the solution against the amount of noise affecting the data. Hence, a good trade-off between stability and accuracy is achieved by correctly choosing an appropriate threshold value. Since it is challenging to estimate the best value of threshold in advance, MI algorithm runs with different values of m and with each value of m different images are generated.

The TSVD algorithm is initially implemented in C++ and to simplify the matrix manipulation, we included the freely available *Eigen libraries* [111]. Main parameters and the data types of algorithm are listed in Tables 6.1 and 6.2, while the pseudo-code of the algorithm is given in Algorithm 1.

Table 6.1: Algorithm parameters.

Parameter	**Value**	**Note**
NV	24	Number of transmitter antennas
NM	24	Number of receiver antennas
NC	18,690	Total grid points in 3D volume
θ_{min}	−80 dB	Minimum threshold
θ_{max}	−10 dB	Maximum threshold
Δ	10 dB	Threshold step

Please note that in both Algorithm 1 and Table 1, the TSVD threshold is defined as a value in decibel, θ. This value compares the relative magnitude of the threshold

Algorithm 1 Pseudo-code of the original software implementation

```
1: $(\mathbf{U}, \mathbf{S}, \mathbf{V}) = \mathbf{SVD}(\mathbf{L})$;   ▷ Singular Value Decomposition of $\mathbf{L}$ operator, computed offline
2: $\mathbf{E} \leftarrow$ measured variation of scattered field
3: $\theta = \theta_{\text{min}}$;
4: while $\theta < \theta_{\text{max}}$ do
5:     $m$ = index of singular value $\sigma_m \in \mathbf{S}$ closer to $\theta$;
6:     $\mathbf{R} = \mathbf{0}$;
7:     for $i = 1$ to $m$ do
8:         $x = \mathbf{E} \cdot \mathbf{U_i}$;
9:         $y = x/\sigma_i$;
10:        $\mathbf{T} = y\mathbf{V_i}$;
11:        $\mathbf{R} = \mathbf{R} + \mathbf{T}$;
12:    end for
13:    storage $\leftarrow \mathbf{R}$;   ▷ $\mathbf{R}$ stored in memory
14:    $\theta = \theta + \Delta$;
15: end while
```

Table 6.2: Data type and dimensions.

Data	**Type**	**Size (FP)**
E	Complex Vector	$2 \times NM^2 = 1152$
S	Real Vector	$NM \times NV = 576$
U	Complex Matrix	$(2 \times NM^2, 2 \times NM^2) = (1152{,}1152)$
V	Complex Matrix	$(2 \times NC, 2 \times NM^2) = (37{,}380{,}1152)$
R	Complex Vector	$2 \times NC = 37{,}380$

singular value to the first and most important singular value. It requires that singular values of S are first arranged in decreasing magnitude and that the index m is found as the index of the singular value σ_m belonging to S whose relative magnitude is closest to the threshold (Algorithm 1 Line 5).

The reason of the value of the various parameters in Table 6.1 is now given. The reason due to which 24 antennas were chosen depends on the physical dimensions of the antennas and their arrangement in the helmet, as it has been already explained in section 6.1. The total number of grid points NC=18690 depends on the size of the investigated volume (20cm×14cm×14cm) and the resolution of the grid. NC is a critical parameter for the execution time of the algorithm, which has to compute $\Delta\chi$ for each of these points. Notice that while we report results only for this setting of NC, this is a constant that can be changed without affecting the functionality neither of the software nor of the hardware that runs the imaging algorithm.

The threshold is another critical parameter for the execution time, because it determines the number of different runs of the algorithm. As stated above, it is difficult to determine a priori which threshold, and so which number of singular values, will result in the best image. For this reason the algorithm is run a number of times that depends on the minimum and maximum threshold and the threshold step. According to the values in table 6.1, the algorithm is executed eight times, starting from threshold -10 dB up to -80 dB in 10-dB steps. Consequently, eight images are generated and the best image is selected at the end. Results for a “good” and a “bad” value of the thresholds are reported in figures 6.3-6.5 and 6.6, respectively.

The pseudo-code in Algorithm 1 has two main sections: the computation of the SVD (line 1) and the computation associated with the *for* loop (Lines 7-12). Since SVD is related to the background and does not change in successive measurements, it can be computed off-line and stored in memory. The results than can be retrieved from memory quickly before executing the rest of the code, hence the accelerator is required to speed up the computation of the other part (for loop). The accelerator which we designed for this section of the code is described in section 6.3.1.

In Table 2 we can see that there are up to S= 576 singular values, obtained by multiplying the number of transmitters (NM) and the number of receivers (NV) (here both are 24, hence 576). In the algorithm, all variables are complex numbers except for σ_i and

θ which are real numbers. **R** is the output of the computation in the pseudo-code, and an image can be plotted from the output **R**, highlighting the variation of the contrast in each point of the region of interest (ROI). *While* loop in the algorithm runs from minimum threshold θ_{min} with step Δ up to maximum threshold θ_{max}, the value of Δ is in table 1 (10 dB). In this way, different images are generated, as explained earlier.

To assess the performance of the MI algorithm we use electromagnetic simulations at a single frequency of 1 GHz, which is appropriate for a good penetration in the head [104]. By illuminating the head model from 24 Tx antennas and by recording the scattered signal received by 24 Rx antennas we obtain the inputs for the MI algorithm. In figure 6.3, an image reconstructed with a threshold value of -80 dB is given. With this value of the threshold, out of the 576 singular values only the first 299 are used. In the figure, there are different slices, which represent different sections in the axial plane of the 3-dimensional ROI of a head. In the figure, blue color is the background, i.e. the part of the scene that did not change across two different measurements, while the yellow color represents blood mass as the area detected by the algorithm that changed the most across two different measurements. All the images are normalized to the highest amplitude value.

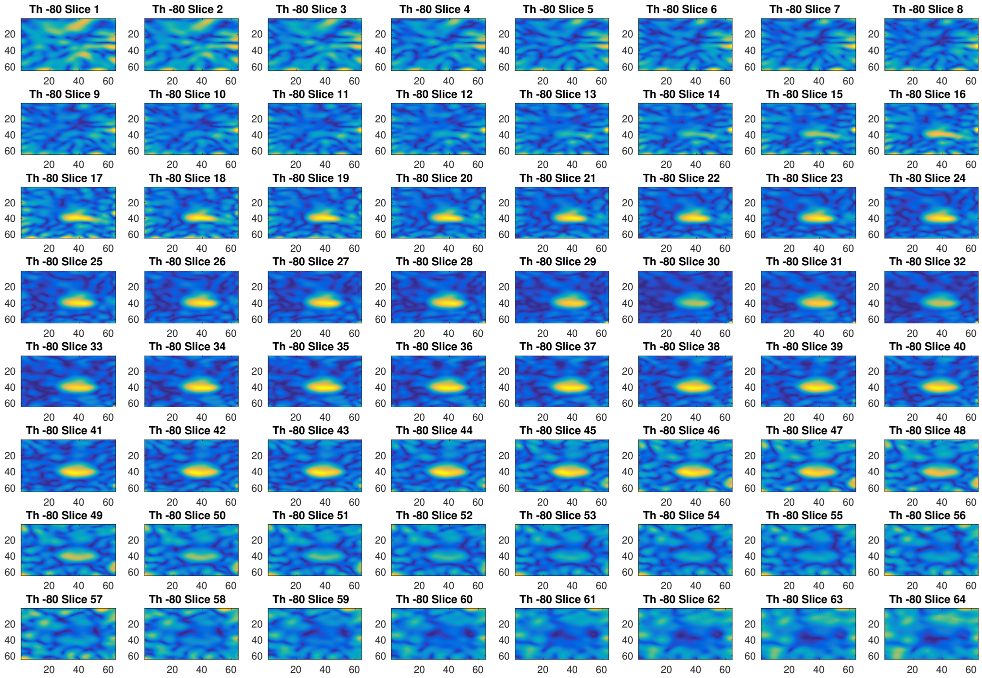

Figure 6.3: Reconstructed images obtained with a threshold value of −80 dB.

Figure 6.4 shows a zoomed section of the image in figure 6.3 with four slices, in which we can better see how the blood mass extension changes with the eight along the axis where the slices have been cut.

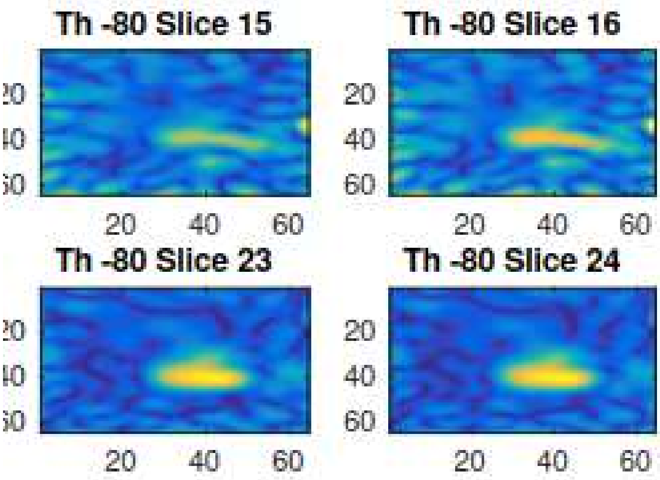

Figure 6.4: Section of the reconstructed images obtained with a threshold value of -80 dB.

Figure 6.5 shows another cutout section of the figure 6.3. Here the shown slices are located at a higher position compared to those of figure 6.4. We can clearly see that the blood mass tends to disappear as we consider slices located higher and higher.

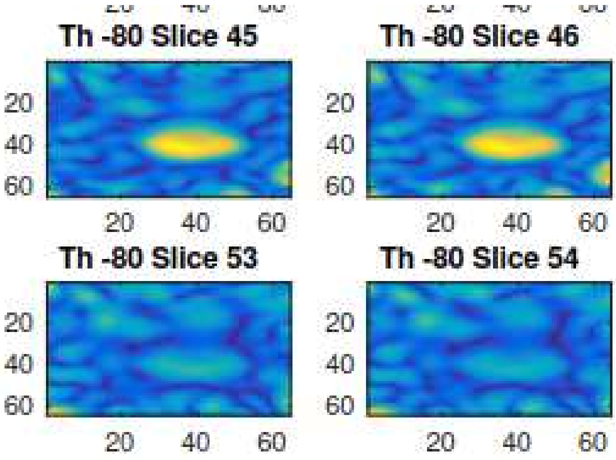

Figure 6.5: Section of the reconstructed images obtained with a threshold value of -80 dB.

Figure 6.6 is another example of the image obtained with a threshold value of -20 dB.

The first 120 singular values generate this image. By comparing this image with those in figures 6.3-6.5, we can clearly see that image of -80 dB has reconstructed a better image and -20 dB is not able to accurately reconstruct it. With −20 dB we have limited information (we are discarding too many singular values), hence resulting image cannot image the stroke.

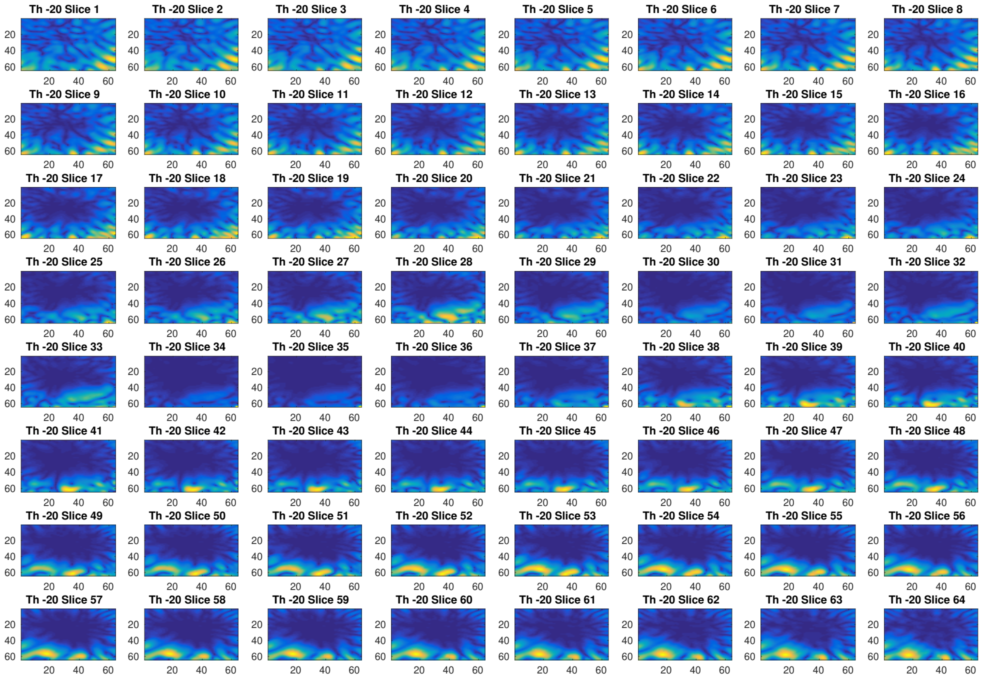

Figure 6.6: Reconstructed images obtained with a threshold value of −20 dB.

6.3 Hardware Implementation of Imaging algorithm

In this part of the chapter implementation of imaging algorithm on specialized hardware is discussed. This part is divided into three sections

- Speeding up the computation with a specialized Accelerator
- Hardware Platform

- Accelerator Design.

6.3.1 Speeding up the computation with a Specialized Accelerator

The computationally intensive part of Algorithm 1 is associated with the **for** loop (Lines 7-12), where the loop runs m times. In a software execution of the algorithm this part of the code will affect the performance and the total time required for the execution of the algorithm will increase considerably as explained in the section 6.4. The accelerator which we had designed deals with this part of the Algorithm 1. The yellow colored block in figure 6.1 represents the algorithm processing block of the MI system. Two different implementations of this block are given in figure 6.5 (a), (b) and figure (c) shows the timing diagram of the execution of these two configurations.

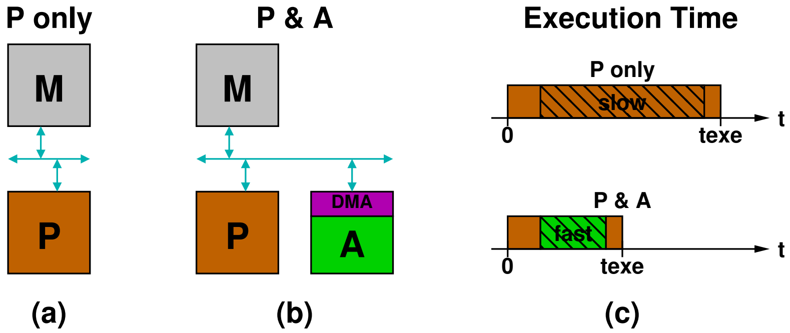

Figure 6.7: Comparison between processing systems implemented: as a general purpose processor alone (**a**); or with an accelerator (**b**); and related timing diagrams (**c**).

In figure 6.7(a), a processor (P) communicates with the memory through a bus. This implementation is labeled as “P only.” In Figure 6.7(b), there is an accelerator (A) connected to the same bus and accesses the memory via DMA. This implementation is labeled as “P&A”. In the timing diagram of the first implementation (P only), the processor runs (brown bar) from the beginning and reaches to end, while for the case of “ P&A” the total execution takes less time, because, the accelerator is evoked at some time (green bar) runs a certain amount of time and then handles the execution to the processor again. For both the execution, note that accelerator only executes some part of the code (replacing the slow section of the code with a fast one), the initial and final parts of the execution time are same for both cases.

A specialized accelerator like the one in the “P & A” case can be faster than a general purpose processor like the one in “P case” only when:

- There is a use of specialized arithmetic units
- There is a higher level of computation parallelism
- A higher level of pipelining that can be achieved through careful design.

An important factor when working with accelerator is to consider the clock frequency, especially in the case of programmable SoC on FPGA. Because, in FPGAs, the processor is often a fixed hardwired component, while on the other hand the accelerator is synthesized from a register-transfer level (RTL) code and then implemented in the PL part of the SoC, hence, the clock frequency of the accelerator is not as high as of the processor. However, the accelerator usually speeds up the computation thanks to the pipelining, higher parallelism and the use of specialized units. The final important factor of hardware acceleration is the speed of data communication, which in other words is the speed at which the accelerator accesses the data stored in the memory.
Let us understand this concept for our cases. In the case of “P&A” if the data transfer time exceeds the time spent by the processor in “P-case” for the computation, then clearly there is no need of using the accelerator. However, when the computation time and data transfer time are comparable then by overlapping data processing and data transfer, the latency of the data communication can be hidden.

6.3.2 Hardware Platform

We mapped the processing block of figure 6.1, highlighted in yellow color to an embedded system. The embedded system consists of a **Xilinx Zynq programmable SoC** with external memory (NAND flash and DDR3), standard peripherals for connectivity, and display ports (VGA, HDMI). We used the Diligent Zedboard board for development and testing of the accelerator. This board is low-cost and contains a Zynq XC7020, 4-GB flash in removable SD card, 512-MB low power DDR3 DRAM memory and the previously mentioned peripherals. Further details about the board and its main components are in [84]. On the Zynq board, we ran a version of Linux based upon Ubuntu LTS 16.04 for ARM [112]. The Zynq SoC has two main parts, The **processing system (PS)** and the **programmable logic (PL)** part. In the PS part, there is a dual-core ARM Cortex A9 with its own L1 and L2 cache, while the PL part features an Artix-7 Xilinx FPGA. Both parts are connected through an AXI bus. Figure 6.8 shows the processing block and the connections between PS and PL. In the figure there is a hypothetical accelerator implemented in the PL part communicating with the PS using FIFO and direct memory access (DMA) controller.

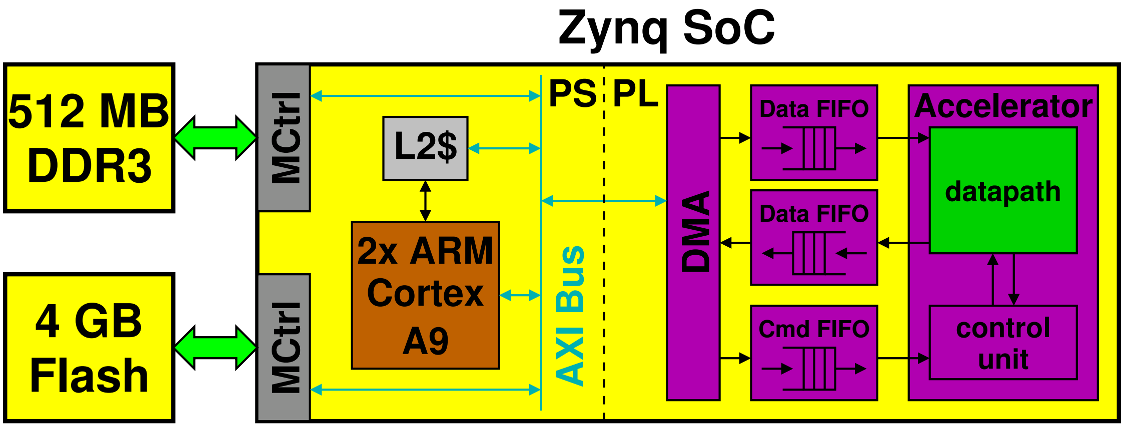

Figure 6.8: Detail of the processing system implemented in a Xilinx Zynq SoC.

Let us again consider the **Algorithm 1** and identify its main parts which need acceleration. We can see that from a computational point of view, it has two main parts:

- Computation of the SVD (line1)
- Computations associated with the for loop (line7-12)

Since computation of the SVD can be done offline and the results stored in SD card can be retrieved from there very quickly before executing the rest of the code, hence for a fast computation the *for* loop is the critical part. Our designed accelerator speeds up the computation of only the *for* loop and is discussed in next section.

6.3.3 Accelerator Design

The Algorithm involves **floating-point (FP)** computation, and the accelerator is designed in such a way that it kept the precision same as the software implementation of the algorithm. *Xilinx Vivado design* tool provides many pre-designed FP blocks such: multipliers, dividers, adders etc. These blocks reduce the design complexity of the accelerator and since they also support the AXI stream protocol their composition is very simplified. These blocks are fully pipelined which makes them very useful for acceleration application because the input data arrays (U and V) are streamed at very high speed via DMA, and they need to be processed instantly. Details about the Xilinx Vivado design tool, IP blocks, AXI streams etc. is available in [83].

In the designed accelerator, we used the composable blocks (discussed earlier) and the functions corresponding to (lines 7-12) of the Algorithm 1 are implemented with them. Figure 6.9 shows the data path of the designed accelerator,

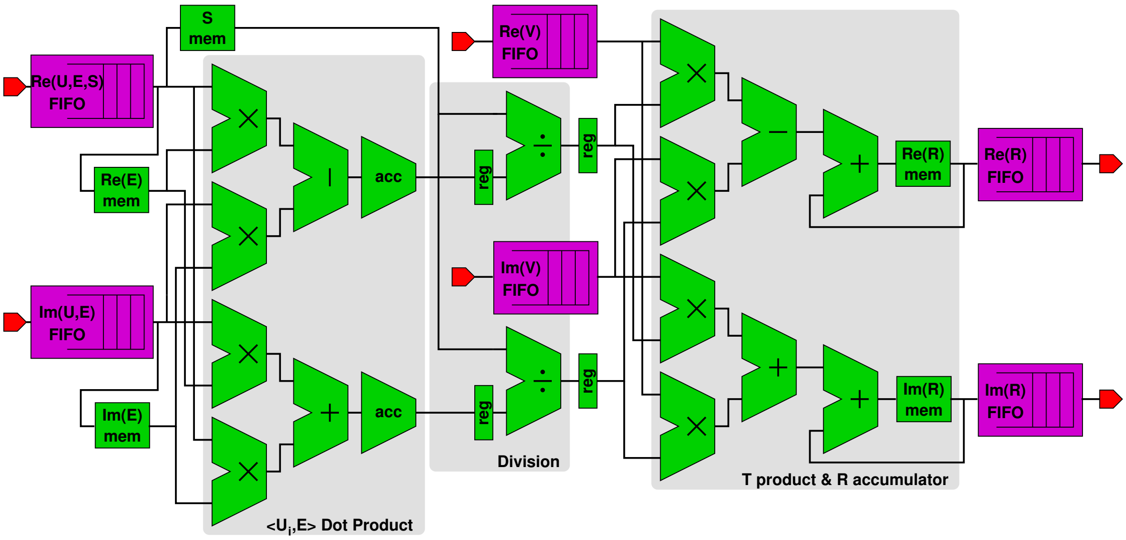

Figure 6.9: Datapath of the accelerator.

from the data path in figure 6.7 we can see that the accelerator has three main subblocks.

- The first subblock computes the dot product(x) between the complex vectors U_i and E. E is fetched from an on-chip memory. The resulting product $Re(x)$ and $Im(x)$ are then stored in corresponding registers (Line 8 in Algorithm 1).
- The second subblock computes $Re(y)$ and $Im(y)$. This block is the divider block, it starts from $Re(y)$ and $Im(y)$ and from the singular value σ_i (Line 9 in Algorithm 1). These singular values are then stored in and loaded from an on chip memory. (within PL part of the Zynq).
- The third subblock in the figure is the block that stores the output R. These accumulated R values are computed from the $Re(T)$ and $Im(T)$ variables (Lines 10-11). The values of the output R are also stored in their separate on-chip memory.

In our designed accelerator, the dot product x and accumulation of R, four floating point (FP) multiplications are computed in parallel, and they are concurrent with various FP subtractions or additions due to pipelining. It is important to note here, as already discussed, accelerators have higher parallelism and deeper pipelining than the general-purpose processors. Moreover, the concurrency of control and datapath operation in the accelerator removes the control overhead for handling the loop in Algorithm 1, whereas the processor may incur such loop overheads. In figure 6.9 there are data FIFOs which are used for communication between PS and PL parts of the SoC. Two of these FIFOs are serving the purpose of transferring first $\boldsymbol{E}$ and $\boldsymbol{S}$ arrays, which are then stored in their respective on-chip memories as shown in figure 6.9. There is another FIFO which transfers the columns of $\boldsymbol{U}$, two FIFOs transfers back the real and imaginary values of $\boldsymbol{R}$ in reverse direction. We had used same FIFOs to transfer the real and imaginary parts of $\boldsymbol{E}$, $\boldsymbol{S}$, and $\boldsymbol{U}$ because $\boldsymbol{E}$ and $\boldsymbol{S}$ are transferred only one time before the while loop in the Algorithm 1, and then $\boldsymbol{U}'s$ columns are transferred one at a time for each loop iteration, hence there is no real advantage in using separate FIFOs for each of these arrays. Moreover, there is no need to store the values of $\boldsymbol{U}$ in on-chip memory, as each column of $\boldsymbol{U}$ is used only one time per iteration, however, $\boldsymbol{E}$ and $\boldsymbol{S}$ are stored in an on-chip memory because they are reused at each iteration. In figure 6.7 control unit controls the repetition of computation performed by data path depending upon the number of loop iterations “m” in Algorithm 1. This number is transferred to the control unit by the command FIFO before transferring the data of $\boldsymbol{U}$ and $\boldsymbol{V}$ columns. Control unit read data from the FIFOs for each of the m iterations and then manages the execution of the three subblocks accordingly. The control unit is basically a **Finite State Machine (FSM)** and is represented by the state transition diagram in figure 6.8. FSM changes the state based upon the commands sent explicitly by the processor to the accelerator via the command FIFO (e.g., cmd=START, cmd=STOP) or on internal events, like completion of reading E, S, U and V from their respective FIFOs when the terminal count is raised (e.g. cntr=UMAX) or when a flag indicates the completion and validity of the computation (e.g. valid DOT). In figure 6.10, block states colored green are the loops that are repeated m times. The diagram also shows that $\boldsymbol{E}$ and $\boldsymbol{S}$ are transferred before the loop is started hence, their FIFOs can be reused for sending U values.

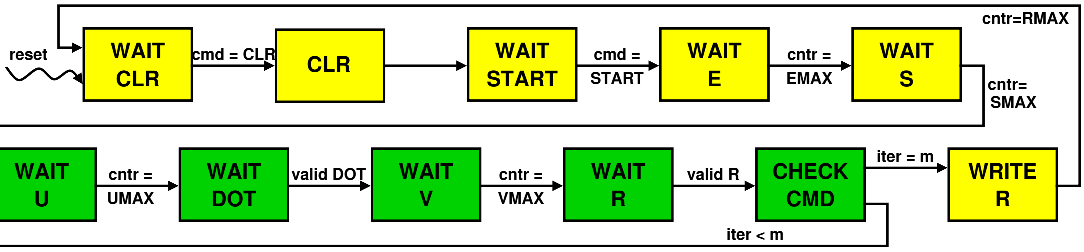

Figure 6.10: State transition diagram for the finite state machine that controls the accelerator's datapath.

The pseudo-code of the Algorithm 1 needs to be modified now, and the pseudo-code in Algorithm 2 shows the code modifications which are required to support the accelerator. On the processor side, workload mainly consists of controlling the data transfer from/to external memory and from/to the accelerator. When the accelerator receives the "start" command, then it starts the computation (line 10 Algorithm 2).

Algorithm 2 Pseudo-code of the hardware-accelerated implementation

```
(U, S, V) = SVD(L);   ▷ Singular Value Decomposition of L operator, computed offline
putdata(S);   ▷ S sent to the accelerator via FIFO data queue
E ← measured variation of scattered field
putdata(E);   ▷ E sent to the accelerator via FIFO data queue
$\theta = \theta_{\min}$;
while $\theta < \theta_{\max}$ do
    m = index of singular value $\sigma_m \in \mathbf{S}$ closer to $\theta$;
    putcmd(m);   ▷ m sent to the accelerator via FIFO command queue
    putcmd(reset(R));   ▷ "reset R" command sent via FIFO command queue
    putcmd(start);   ▷ "start" command sent via FIFO command queue
    for i = 1 to m do
        putdata(U_i);   ▷ ith column of U sent via FIFO data queue
        putdata(V_i);   ▷ ith column of V sent via FIFO data queue
    end for
    getdata(R);   ▷ R retrieved from FIFO data queue
    storage ← R;   ▷ R stored in memory
    $\theta = \theta + \Delta$;
end while
```

In the pseudo-code of Algorithm 2 the operations performed by putdata and putcmd are nonblocking; hence the two columns U_i and V_i are streamed simultaneously. Moreover, as soon the first data are available at the output of FIFO, control unit lets the datapath to start and as a result of it, a complete overlap of computation and data transfer is enabled.

6.4 Results

For the MI system to monitor brain stroke, we designed the accelerator and its FIFO interfaces at the register-transfer level (RTL) using the description language VHDL and implemented it with Vivado 2016.1. The Vivado software performs the logic synthesis and place and route targeting the FPGA of XC7Z020 Zynq device. The designed accelerator uses a single 100 MHz clock. All the FPGA resources which the accelerator utilized are in Table 6.3.

Table 6.3: FPGA resources utilized by the accelerator in the Xilinx XC7Z020 Zynq device.

Resource	**Utilization**
LUTs	19.04%
FFs	14.2%
BRAM	100%
DSPs	14.55%
IOBs	38%

Our designed accelerator uses less than 20% of the logic resources look-up tables (LUTs), digital signal processing blocks (DSPs) and flip-flops (shown in Table 3). The Block RAMs (BRAMs) has been utilized to 100% (saturated the utilization limit) because all the FIFOs uses this type of resource. In fact FIFOs utilize 70% of BRAM resources while the accelerator uses 30% of the remaining resources to store **E, S,** and **R**.

A sketched timing diagram in figure 6.11 shows that computation and communication overlap, hence the total execution time depends upon the data transfer time from the processor to the accelerator and back to the processor and is mainly determined on time for transferring the columns of U and V at each iteration of the for loop.

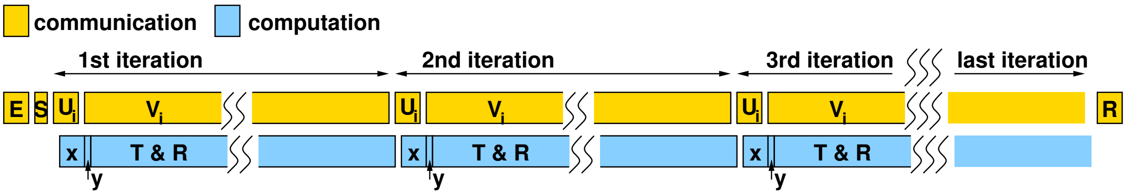

Figure 6.11: Timing diagram showing concurrency of communication (between processor and accelerator) and computation (within the accelerator).

As mentioned before the accelerator has a 100 MHz clock, for the AXI bus clock is 100 MHz and one floating point (FP) value can be transferred in burst mode after each clock cycle. Consequently, columns of U and V are transferred each in

1152/100= 1152μs time to transfer U

37380/100 = 373.8μs time to transfer V

The number of iterations for the for loop is generally 300 for the threshold between **-80** and **-50 dB**. Number of iterations for the *for* loop is less when the threshold value is higher, and this relation can be observed in fig 6.10.

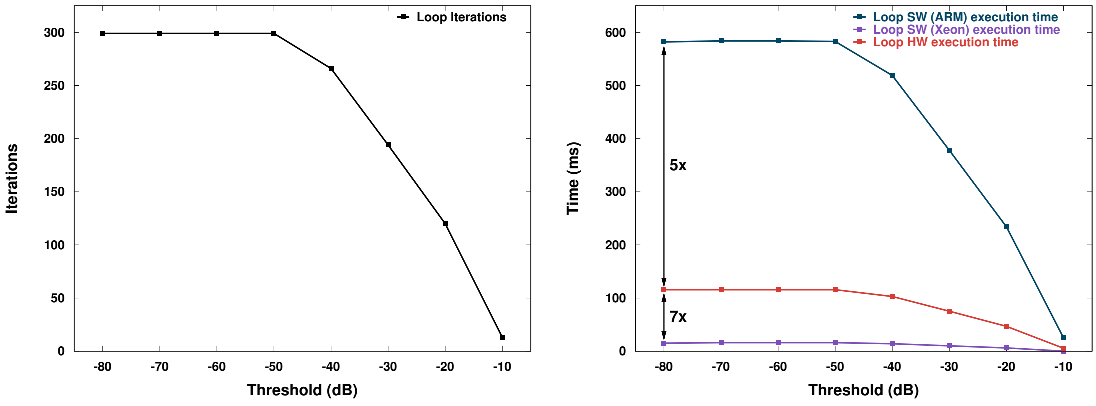

(a)

(b)

Figure 6.12: (**a**) Number of iterations; and (**b**) execution time.

Figure 6.12 (b) shows the total execution time corresponding to the relationship between the number of iterations and the threshold value. In this figure, the two curves colored blue and red represents the time required to complete the execution by the ARM processor and our hardware-accelerated case. Comparing both the curves, we can see that there is an improvement of at least five times when the accelerator is used. In the figure, there is another purple color curve which represents the software case for an Intel Xeon Processor E5-2650. Comparison of this with our accelerator shows that there is a very significant performance gap between them, in fact our accelerator has 7 times less speed then Xeon processor. However, The Intel Xeon Processor has better performance due to a very high-power cost, because the Xeon processor consumes power in the order of 100 W, which is way more then the power that our board consumes. In fact the development and evaluation board, where we implemented our processing system, consumes only 3.8 W, which in comparison to Intel Xeon processor is 26 times less. The performance-per-watt figure of merit of our MI system is about 3.7 times greater than that of Intel Xeon processor. However, since the board only allows to measure the overall power consumed, which includes several other more substantial contributions as a result of which we, unfortunately, were not able to measure the magnitude of power consumed by the ARM processor and accelerator. Nevertheless, the magnitude of power consumed still lies in the requirement of low power, and as a result of this low power consumption, the system is portable and has a very small form factor.

6.5 Conclusion

In this chapter, we described the design of a processing subsystem used in a MI system for continuous brain stroke monitoring. The designed subsystem is low-cost, low-power and compact. The subsystem consists mainly of a Xilinx Zynq SoC, which has an ARM-based CPU and an FPGA connected with the CPU by AXI bus interfaces. The implementation of the hardware accelerator in the FPGA decreases the execution time of the algorithm 5 times compared to its software execution by executing the heavy part of the computation itself.

Chapter 7

Conclusions

7.1 Conclusion

In this thesis, two different Microwave systems, one for detecting breast cancer and second for monitoring the brain stroke are discussed. The microwave imaging systems presented in the thesis are novel as both systems, not only can detect the presence of abnormal tissue but the imaging algorithms are also accelerated by specialized hardware accelerators for speedy execution of the algorithm.

7.1.1 COTS-Based Microwave Imaging System for Breast Cancer Detection

Chapters 3, 4 and 5 are devoted to the prototype which we build to detect breast cancer in females. The built prototype is different from other MI systems because for its operation it uses commercially available components off the shelf (COTS), altogether avoiding the use of costly and bulky lab equipment, such as Vector Network Analyzers (VNA) which other MI systems usually use. Use of COTS makes it possible to have a small form factor MI system. We used I-MUSIC as Imaging algorithm because for its detection it does not require large bandwidth, it offers the advantage of avoiding the processing issues of nonlinear inversion methods and most importantly this approach is independent of antenna characterization which is very important for detection systems as antenna response is unknown in practical cases when they are placed close to the breast. To speed up the execution of the I-MUSIC, especially of its most computationally intensive kernel we paired the embedded processor with a hardware accelerator running in FPGA. As an embedded system we used Xilinx's Zynq SoC to control the prototype for transmitting and receiving the radiofrequency (RF) signals and to process the I-MUSIC algorithm. In the prototype we used as breast and tumor phantoms different mixtures having properties like a real tumor inside a breast, such as (60-40% glycerin-water) mixture and a 3D-printed breast phantom. Both these tumor models are proposed in the literature due to their excellent mimicking ability of the real tumor. As a coupling liquid, we used (80-20% glycerin-water) mixture and Triton X-100 a commercially available lab detergent, because both these liquids mimic the dielectric characteristics of the healthy breast tissue. During our experiment with the prototype, we used both 2D breast phantoms and 3D printed breast models with three separate tissues for adipose, fibro-glandular and tumor. The prototype has a working frequency range of (1.4-1.6 GHz) because at this range the receiver has a good matching. However, this range does not affect the performance of the prototype as the comparison of the results obtained from the prototype with the results of the VNA operating in full range are very similar, in fact in some cases, the results of our COTS-based prototype are better than the results obtained from VNA operating in full range. Moreover, due to hardware acceleration of the imaging algorithm we speed up its execution, in fact, our prototype with hardware acceleration is 20× faster than a high-performance server at image reconstruction.

7.1.2 Acceleration of a Microwave Imaging Algorithm for Brain Stroke Monitoring

Chapter 6 of the thesis deals with a MI subsystem for monitoring brain stroke. Based on our work for designing a MI system to detect breast cancer, we used most of those concepts and ideas to design a processing subsystem for monitoring brain stroke. Our goal was to design a low power, portable, and cost-effective subsystem to monitor brain stroke with sufficiently fast response for bedside monitoring of patients during practical clinical applications. The imaging algorithm we used to monitor stroke is different from the I-MUSIC which we used for breast cancer detection. The algorithm which we used here is TSVD in which signals are acquired at single frequency instead in time or multi-frequency, which offers the advantage of simple acquisition and comparatively fast processing; an essential criteria for a continuous bedside monitoring device. The algorithm for image reconstruction detects the variation of blood mass across two successive data acquisition and the reconstructed image shows the variation of the stroke over time. From the reconstructed image, it is possible to analyze the condition of stroke visually and to take necessary actions accordingly.

Like the MI system for breast cancer detection, we used the Xilinx Zynq SoC device for processing the algorithm, and we implemented a hardware accelerator in its FPGA to execute the heavy part of the computation. Our designed accelerator uses less than 20% logic resources of the Xilinx Zynq device. The execution time of the algorithm is five times faster compared with the software execution without losing precision.

Both the MI systems presented in this thesis produced very encouraging results, and due to hardware acceleration, they have fast execution of the imaging algorithms. As per the best of our knowledge, this is the first attempt in accelerating imaging algorithms for MI systems with dedicated hardware to monitor brain strokes and to detect breast cancer in females.

Chapter 8

Publication During P.hD.

List of Publications during P.hD is given below:

- Low-Cost Low-Power Acceleration of a Microwave Imaging Algorithm for Brain Stroke Monitoring / Sarwar, Imran; Turvani, Giovanna; Casu, Mario; Tobon, Jorge; Vipiana, Francesca; Scapaticci, Rosa; Crocco, Lorenzo. - In: JOURNAL OF LOW POWER ELECTRONICS AND APPLICATIONS. - ISSN 2079-9268. - ELECTRONIC. - 8: 4: 43 (2018), pp. 1-13.

- A feasibility study for cerebrovascular diseases monitoring via microwave imaging / Tobon Vasquez, JA; Scapaticci, R .; Turvani, G .; Cow, M .; Sarwar, I .; Casu, MR; Dassano, G .; Joachimowicz, N .; Duchene, B .; Bellizzi, G .; Tedeschi, E .; Crocco, L .; Vipiana, F .. - ELECTRONIC. - (2017), pp. 1280-1282. ((Speech presented at the 19th International Conference on Electromagnetics in Advanced Applications, ICEAA 2017 held in Verona (I) in 2017.

- A COTS-Based Microwave Imaging System for Breast-Cancer Detection / Casu, MARIO ROBERTO; Vacca, Marco; TOBON VASQUEZ, JORGE ALBERTO; Pulimeno, Azzurra; Sarwar, Imran; Solimene, Raffaele; Vipiana, Francesca. - In: IEEE TRANSACTIONS ON BIOMEDICAL CIRCUITS AND SYSTEMS. - ISSN 1932-4545. - PRESS. - 11: 4 (2017), pp. 804-814.

- Experimental assessment of qualitative microwave imaging using a 3-D realistic breast phantom / TOBON VASQUEZ, JORGE ALBERTO; Vipiana, Francesca; Casu, MARIO ROBERTO; Vacca, Marco; Sarwar, Imran; Scapaticci, R .; Joachimowicz, N .; Duchene, B .. - ELECTRONIC. - (2017), pp. 2728-2731. ((Speech presented at the 11th European Conference on Antennas and Propagation conference (EUCAP) held in Paris in 19-24 March 2017.

Appendix A

C-code implementation of the I-MUSIC Algorithm

```
#include <stdio.h>
#include <stdlib.h>
#include <unistd.h>
#include <complex.h>
#include <math.h>
#include <sys/time.h>
#include ”f2c.h”
#include ”blaswrap.h”
#include ”clapack.h”

#define NUMFREQ 11
#define S11_S21 1
#define switch_tx_rx 1

#define c 300000000
#define nx 200
#define ny 200
```

```
int main(){

doublereal normc();
doublecomplex multr();
doublecomplex divr();
doublecomplex addc();
doublecomplex expc();
doublecomplex sqrtc();
doublecomplex multc();
doublecomplex conju();
int max_array();
doublereal complex_norm();
doublereal max_matrix();

integer ROWS = 35;
integer COLS = 24;
integer ldu=ROWS;
integer lda=ROWS;
integer ldvt=COLS;
int i,j,t,q,u,v,w;

                //File directors//
                FILE * re;
                FILE * im;
                FILE * eemr;
                FILE * eemi;
                FILE * epsre;
                FILE * epsimg;
                FILE * xxf;
                FILE * yyf;
                /////////////////

doublecomplex J;
```

```
doublereal beta=45;
doublereal theta[COLS];
doublereal angle_step;
doublereal ang[21];
doublereal x,y;
doublereal xx[nx], yy[ny];
doublereal xo[COLS];
doublereal yo[COLS];
doublereal xi[COLS];
doublereal yi[COLS];
doublereal rs=0.095;
doublereal mod;
doublereal x_circle_1 = 0.0085;
doublereal y_circle_1 = 0.0205;
doublereal r_circle_1 = 0.0035;
doublereal xx1[21],yy1[21];
doublereal epsrbre[NUMFREQ];
doublereal epsrbimg[NUMFREQ];
doublecomplex epsrb[NUMFREQ];
doublereal  real[ROWS][COLS];
doublereal  imag[ROWS][COLS];
doublecomplex e_m[ROWS*COLS];
double S[COLS];
doublecomplex U[ROWS*ROWS];
doublecomplex VT[COLS*COLS];
doublecomplex S_d[ROWS*COLS];
doublereal ee_mr[ROWS][COLS];
doublereal ee_mi[ROWS][COLS];
doublecomplex ee_m[ROWS*COLS];
doublecomplex Ediff1[NUMFREQ*COLS];
doublecomplex Ediff1_conj[NUMFREQ*COLS];
doublecomplex Ediff1_trasp[COLS*NUMFREQ];
doublecomplex R[COLS*COLS];
doublereal eig[COLS];
```

```
doublecomplex eigvecs[COLS*COLS];
doublecomplex provv[COLS];
doublereal norm[NUMFREQ];

doublereal freq[NUMFREQ] = {1.40e+09, 1.42e+09, 1.44e+09,
                 1.46e+09, 1.48e+09, 1.50e+09, 1.52e+09, 1.54e+09,
                 1.56e+09, 1.58e+09, 1.60e+09};
doublereal ws[NUMFREQ];
doublecomplex kb[NUMFREQ];
doublecomplex Ak[COLS];
doublecomplex F_provv;
double F[ny*nx][NUMFREQ];
double Fcm[ny*nx];
double P22[ny*nx];
double PP[ny*nx];

  //for zgesdd_ subroutine
integer lwork = COLS*COLS+2*COLS+ROWS;
doublecomplex work[lwork];
doublereal rwork[5*COLS*COLS+7*COLS];
integer iwork[8*COLS];
integer info;

        //for zheevd_ subroutine
integer lworkz = COLS*COLS+2*COLS;
integer lrworkz = 2*COLS*COLS+5*COLS+1;
integer liworkz = 5*COLS+3;
doublecomplex  workz[lworkz];
doublereal rworkz[lrworkz];
integer iworkz[liworkz];



        /////Time elements/////
struct timeval fft1, fft2;
```

```
struct timeval svd1, svd2;
struct timeval eig1, eig2;
struct timeval her1, her2;
struct timeval det1, det2;
struct timeval tot1, tot2;
        ////////////////////////

        gettimeofday(&tot1,NULL);
        gettimeofday(&fft1,NULL);

                //initialize -i
                J.r = 0.0;
                J.i = -1.0;

        //take real and imaginary part to build e_m matrix
 re = fopen(”realpart.txt”,”r”);
for(i=0;i<ROWS;i++){
        for(j=0;j<COLS;j++){
                fscanf(re,”%lf”,&real[i][j]);
                }
        }
        fclose(re);

im = fopen(”imagepart.txt”,”r”);
for(i=0;i<ROWS;i++){
        for(j=0;j<COLS;j++){
                fscanf(im,”%lf”,&imag[i][j]);
                }
        }
        fclose(im);

        //compute e_m matrix
for(i=0;i<ROWS;i++){
  for(j=0;j<COLS;j++){
```

```
                e_m[i+ROWS*j].r = real[i][j];
                e_m[i+ROWS*j].i = imag[i][j];
                }
        }

        gettimeofday(&fft2,NULL);
        printf("FFT_time = %f secondi\n",(doublereal)
                (fft2.tv_usec - fft1.tv_usec)/1000000 +
                (doublereal) (fft2.tv_sec - fft1.tv_sec));

        //compute the svd.

        gettimeofday(&svd1,NULL);

        zgesdd_( "A",&ROWS, &COLS, e_m, &lda, S,  U,
    &ldu, VT, &ldvt, work, &lwork, rwork, iwork, &info);
                //verify the correctness of zgesdd function

                if(info>0){
                        printf("Error in  zgesdd!\n");
                        return 0;
                }

 //initialize S_d elements all zero
                for(i=0;i<ROWS;i++){
                        for(j=0;j<COLS;j++){
                                S_d[j*ROWS+i].r = 0;
                                S_d[j*ROWS+i].i = 0;
                        }
                }

//compute declutter matrix (take eigenvalues between 1st&10th)
        for(t=1;t<NUMFREQ;t++){
        for(i=0;i<ROWS;i++){
```

```
                for(j=0;j<COLS;j++){
                S_d[i+j*ROWS].r= S[t]*U[i+ROWS*t].r*VT[j*COLS+t].r
                                         + S_d[i+j*ROWS].r;
                S_d[i+j*ROWS].i= S[t]*U[i+ROWS*t].i*VT[j*COLS+t].i
                                        + S_d[i+j*ROWS].i;
                                }
                        }
                }

        gettimeofday(&svd2,NULL);
                printf("SVD_time = %f secondi\n",(doublereal)
                (svd2.tv_usec - svd1.tv_usec)/1000000 +
                (doublereal) (svd2.tv_sec - svd1.tv_sec));

                ///////Angles evaluation///////
                angle_step = 360/COLS;
                theta[0] = 0;
                theta[COLS-1] = -340;

                for(i=1;i<COLS-1;i++){
                        theta[i] = -angle_step*i;
                }

                x = 0.1;
                y = 0.0;

                /*Vector with receiving antennas position [1X24]*/.

for(i=0;i<COLS;i++){
if (S11_S21 == 0){                //S11
        xo[i] = x*cos((theta[i]*0.0174532925))-
        y*sin((theta[i]*0.0174532925));
        yo[i] = x*sin((theta[i]*0.0174532925))+
        y*cos((theta[i]*0.0174532925));
```

```
                }       else if (S11_S21 == 1){     //S21
        xo[i] = x*cos(((theta[i]+beta)*0.0174532925))-
                        y*sin(((theta[i]+beta)*0.0174532925));
        yo[i] = x*sin(((theta[i]+beta)*0.0174532925))+
        y*cos(((theta[i]+beta)*0.0174532925));
                        }

if (switch_tx_rx == 1){     // normal
        xo[i] = x*cos(((theta[i]+beta)*0.0174532925))-
        y*sin(((theta[i]+beta)*0.0174532925));
        yo[i] = x*sin(((theta[i]+beta)*0.0174532925))+
        y*cos(((theta[i]+beta)*0.0174532925));
        }else if (switch_tx_rx == 0){ //switch antennas position
        xo[i] = x*cos((theta[i]*0.0174532925))-
        y*sin((theta[i]*0.0174532925));
        yo[i] = x*sin((theta[i]*0.0174532925))+
        y*cos((theta[i]*0.0174532925));
                        }

        /* Vector with transmitting antennas position [1x24]*/

if (switch_tx_rx == 1){       //normal
        xi[i] = x*cos((theta[i]*0.0174532925))-
        y*sin((theta[i]*0.0174532925));
         yi[i] = x*sin((theta[i]*0.0174532925))+
         y*cos((theta[i]*0.0174532925));
        }else if (switch_tx_rx == 0){ //switch antennas position
        xi[i] = x*cos(((theta[i]+beta)*0.0174532925))-
        y*sin(((theta[i]+beta)*0.0174532925));
        yi[i] = x*sin(((theta[i]+beta)*0.0174532925))+
        y*cos(((theta[i]+beta)*0.0174532925));
                        }
                }
        ///////end angles evaluation///////
```

```
//define xx and yy vectors
xxf = fopen(”xx.txt”,”r”);
for(i=0;i<nx;i++){
        fscanf(xxf,”%lf”,&xx[i]);
        }
fclose(xxf);

yyf = fopen(”yy.txt”,”r”);
for(i=0;i<ny;i++){
        fscanf(yyf,”%lf”,&yy[i]);
}
fclose(yyf);


//take real and imaginary part to build ee_m matrix
eemr = fopen(”EE_m_matrix_real.txt”,”r”);
for(i=0;i<ROWS;i++){
        for(j=0;j<COLS;j++){
                fscanf(eemr,”%lf”,&ee_mr[i][j]);
                }
}
fclose(eemr);

eemi = fopen(”EE_m_matrix_imag.txt”,”r”);
for(i=0;i<ROWS;i++){
        for(j=0;j<COLS;j++){
                fscanf(eemi,”%lf”,&ee_mi[i][j]);
                }
}
fclose(eemi);

//compute ee_m matrix
for(i=0;i<ROWS;i++){
```

```
        for(j=0;j<COLS;j++){
                ee_m[i+ROWS*j].r = ee_mr[i][j];
                ee_m[i+ROWS*j].i = ee_mi[i][j];
        }
}

//define ws vector
for(i=0;i<NUMFREQ;i++){
        ws[i] = 2*M_PI*freq[i];
}

//take real and imaginary part to build epsrb vector
epsre = fopen("epsrb_real.txt","r");
for(i=0;i<NUMFREQ;i++){
        fscanf(epsre,"%lf",&epsrbre[i]);
}
fclose(epsre);

epsimg = fopen("epsrb_img.txt","r");
for(i=0;i<NUMFREQ;i++){
        fscanf(epsimg,"%lf",&epsrbimg[i]);
        }
fclose(epsimg);

for(i=0;i<NUMFREQ;i++){
        epsrb[i].r = epsrbre[i];
        epsrb[i].i = epsrbimg[i];
        }

gettimeofday(&eig1,NULL);

//Ediff1 matrix and its transpose and conjugate:

//Ediff1 matrix
```

```
     for(i=0;i<NUMFREQ;i++){
             for(j=0;j<COLS;j++){
                     Ediff1[i+NUMFREQ*j] = ee_m[i+ROWS*j];
             }
     }


             //transpose
     for(i=0;i<NUMFREQ;i++){
     for(j=0;j<COLS;j++){
             Ediff1_trasp[j+COLS*i].r = Ediff1[i+NUMFREQ*j].r;
             Ediff1_trasp[j+COLS*i].i = Ediff1[i+NUMFREQ*j].i;
                     }
             }


             //conjugate
     for(i=0;i<NUMFREQ;i++){
     for(j=0;j<COLS;j++){
     Ediff1_conj[i+NUMFREQ*j] = conju(Ediff1[i+NUMFREQ*j]);
                     }
             }


             /////Correlation Matrix//////
for(t=0;t<NUMFREQ;t++){


 for(i=0;i<COLS;i++){
      for(j=0;j<COLS;j++){
             R[i+COLS*j] = multc(Ediff1_trasp[i+t*COLS],
             Ediff1_conj[t+j*NUMFREQ]);
                             }//j
                     }//i


                     /*compute eigenvalues and eigenvectors;
                     - eig --> contains the eigenvalues;
                     - R   --> contains eigenvectors,*/
```

```
zheevd_("V", "U",&COLS, R, &COLS, eig, workz,
        &lworkz, rworkz, &lrworkz, iworkz, &liworkz, &info);



//save each eigenvectors into a 24x11 matrix
for(j=0;j<COLS;j++){
eigvecs[t*COLS+j] = R[max_array(COLS,eig)*COLS+j];
provv[j] = R[max_array(COLS,eig)*COLS+j];
        }//j
norm[t] = complex_norm(COLS,provv);
        }//t



        gettimeofday(&eig2,NULL);
printf("EIGENVALUE_time = %f secondi\n",
(doublereal) (eig2.tv_usec - eig1.tv_usec)/1000000
 + (doublereal) (eig2.tv_sec - eig1.tv_sec));

        gettimeofday(&her1,NULL);

for(w=0;w<NUMFREQ;w++){

//compute different wave numbers
kb[w].r = ws[w]*(sqrtc(epsrb[w]).r/c);
kb[w].i = -ws[w]*fabs(sqrtc(epsrb[w]).i/c);

for(u=0;u<nx;u++){
for(v=0;v<ny;v++){
        F_provv.r = 0.0;
        F_provv.i = 0.0;
for(q=0;q<COLS;q++){
        //steering vector
Ak[q]=multc(expc( multc(multr(kb[w],sqrt(pow((xx[u]-xo[q]),2)
```

```
                +pow((yy[v]-yo[q]),2))),J) ),
                expc( multc(multr(kb[w],sqrt(pow((xx[u]-xi[q]),2)
                +pow((yy[v]-yi[q]),2))),J) ));

        //complex hermitian product
        F_provv =addc(multc(conju(Ak[q]),eigvecs[w*COLS+q]),F_provv);
                                        }//q_2

        F[v+u*ny][w] =normc(divr(F_provv,complex_norm(COLS,Ak)*norm[w]));
                                }//v
                        }//u
                }//w



                gettimeofday(&her2,NULL);
printf(”HERMITIAN_time = %f secondi\n”,(doublereal)
             (her2.tv_usec - her1.tv_usec)/1000000 + (doublereal)
             (her2.tv_sec - her1.tv_sec));

                gettimeofday(&det1,NULL);

                //initialize Fcm matrix
                for(v=0;v<ny;v++){
                        for(u=0;u<nx;u++){
                                Fcm[v+u*ny] = 1.0;
                        }
                }

                //compute denominator of detection function
for(w=0;w<NUMFREQ;w++){
        for(v=0;v<ny;v++){
                for(u=0;u<nx;u++){
        Fcm[v+ny*u] = Fcm[v+ny*u] * (1-pow(F[v+ny*u][w],2));
                                }
```

```
                }
        }

        //compute Detection Function
        for(v=0;v<ny;v++){
                for(u=0;u<nx;u++){
                        P22[v+ny*u] = 1/Fcm[v+ny*u];
                }
        }



gettimeofday(&det2,NULL);
printf(”DETECTION_time = %f secondi\n”,(doublereal)
  (det2.tv_usec - det1.tv_usec)/1000000 +
  (doublereal) (det2.tv_sec - det1.tv_sec));



gettimeofday(&tot2,NULL);
printf(”\nTOTAL_time = %f secondi\n”,(doublereal)
   (tot2.tv_usec - tot1.tv_usec)/1000000 +
   (doublereal) (tot2.tv_sec - tot1.tv_sec));

        //define xx1 e yy1 elements to plot detection circle
        ang[0]=0;
        ang[20]=2*M_PI;

        for(i=1;i<20;i++){
                ang[i] = M_PI/10 + ang[i-1];
        }

        for(i=0;i<21;i++){
                xx1[i]= x_circle_1 + r_circle_1*cos(ang[i]);
                yy1[i]= y_circle_1 + r_circle_1*sin(ang[i]);
        }
```

```
        //compute PP matrix, to plot it
for(v=0;v<ny;v++){
        for(u=0;u<nx;u++){
        PP[v+ny*u] = 20*log10(P22[v+ny*u]/max_matrix(ny,nx,P22));
                        }
                }

        //without noise;represent the circle into the rectangle
        for(v=0;v<ny;v++){
        for(u=0;u<nx;u++){
                mod = sqrt(pow(xx[v],2)+pow(yy[u],2));
                if(mod > rs){
                PP[v+ny*u]=-10;
                        }
                }
        }



//print detection function PP on a file  with xx and yy

FILE* file=fopen("/dev/matrix.txt","w");
for(u=0;u<nx;u++){
for(v=0;v<ny;v++){
fprintf(file,"%.3f %.3f %.3f\n",xx[u],yy[v],PP[v+ny*u]);
                        }
        fprintf(file,"\n");
        }
        fclose(file);

        //print on a file the coordinates
        FILE* file1=fopen("/dev/coordin.txt","w");
        for(u=0;u<21;u++){
                fprintf(file1,"%f %f\n",xx1[u],yy1[u]);
```

```
                }
                fclose(file1);

                return 0;
        }

        //function to determine the maximum value between
        //the elements of a doublereal array

        int max_array(int n, doublereal *array){

        int i,index;
        doublereal max=array[0];

        for(i=0;i<n;i++){

        if(array[i] >=  max ){
                max = array[i];
                index = i;
                }//if

                }//for
                return index;
        }

        //function to define norm of a complex values vector
doublereal complex_norm(int n, doublecomplex *array){
        doublereal norm, square=0.0;
                int i;

for(i=0;i<n;i++){
square =  array[i].r*array[i].r + array[i].i*array[i].i + square;
                }
                norm = sqrt(square);
```

```
        return norm;
}



//function to determine the maximum value between
//the elements of a doublereal matrix

doublereal max_matrix(int m, int n, doublereal *matrix){

        int i,j;
        doublereal max=matrix[0];

        for(i=0;i<m;i++){
                for(j=0;j<n;j++){

                        if(matrix[i+j*m] >=  max ){
                                max = matrix[i+j*m];
                        }//if
                }//for_j
        }//for_i
        return max;
}

doublecomplex conju(doublecomplex a){

        doublecomplex z;
        z.r = a.r;
        z.i = (-1)*a.i;
        return z;
}

doublecomplex multc(doublecomplex a, doublecomplex b){

doublecomplex res;
```

```
    res.r = a.r*b.r - a.i*b.i;
    res.i = a.r*b.i + a.i*b.r;
return res;
    }

    doublecomplex sqrtc(doublecomplex a){
    doublecomplex res;
    doublereal mod, theta;

    mod = sqrt(a.r*a.r + a.i*a.i);
    theta = atan(a.i/a.r);
    res.r = sqrt(mod) * (cos(theta/2));
    res.i = sqrt(mod) * (sin(theta/2));
    return res;
    }

    doublecomplex expc(doublecomplex a){

    doublecomplex res;
    doublereal t = exp(a.r);
    res.r = cos(a.i);
    res.i = sin(a.i);
    res.r=t*res.r;
    res.i=t*res.i;

            return res;

    }

    doublecomplex addc(doublecomplex a, doublecomplex b){

    doublecomplex res;
    res.r = a.r + b.r;
    res.i = a.i + b.i;
```

```
        return res;
}

doublecomplex divr(doublecomplex a, double b){

doublecomplex res;
res.r = a.r/b;
res.i = a.i/b;

        return res;
}

doublecomplex multr(doublecomplex a, doublereal b){

doublecomplex res;
res.r = a.r*b;
res.i = a.i*b;

        return res;
}

doublereal normc(doublecomplex a){
doublereal norm;
norm =  sqrt(a.r*a.r + a.i*a.i);
return norm;
}
```

Appendix B

C++ implementation of the TSVD Algorithm for Brain Stroke Monitoring

---

```
#include <stdio.h>
#include <stdlib.h>
#include <math.h>
#include <iostream>
#include <fstream>
#include <string>
#include <sstream>
#include <complex>
#include <Eigen/Dense>
#include <vector>
#include <ctime>
#include <chrono>
```

```
using namespace Eigen;
using namespace std;

#define TRUE 1
#define FALSE 0
#define CHARMAX 20

#define NV 24 /* Number of transmitters */
#define NM 24 /* Number of receivers */
#define NX 64 /* x points */
#define NY 64 /* y points */
#define NZ 64 /* z points */
#define NC 18690 /*total points IT COULD BE A NON CARTESIAN GRID*/

        /* Constants' definitions */
#define m0 12.56637061e-7
#define e0 8.854188e-12
#define freq 1e9
#define eb 40
#define sb 0.01
#define pi 3.1415926

        /* Customizable parameters */
#define threshold -5
#define minT -80 /* Maximum threshold */
#define maxT -20 /* Minimum threshold */
#define stepT 10 /* Threshold Step */
#define reconstructionIndex 5



        /* Custom complex type definition */
#define myFloat float
#define myInt int
#define ComplexMatrix MatrixXcf /*Matrix of Complex.d=double,f=float*/
```

```
#define FloatVector VectorXf /* Matrix of: d = double, f = float */
#define FloatRowVector RowVectorXcf
#define ComplexVector VectorXcf /*Vector of Complex.d=double,f=float*/

namespace patch
{
template < typename T > std::string to_string( const T& n )
        {
        std::ostringstream stm ;
        stm << n ;
        return stm.str() ;
        }
}

const std::complex<myFloat> If(0.0f, 1.0f);
struct svd_complex_struct {
        myFloat r;
        myFloat i;
        };

        typedef struct svd_complex_struct myComplex;


void createMatrixFromFileC(char fileName[],
            myInt r, myInt c, ComplexMatrix &Mat_E);
void createMatrixFromFileR(char fileName[],
            myInt r, FloatVector &Vec_E);

int main()
{
        myFloat Q, threshold_tmp;
        myInt j;

        /* Load U and V solutions from file */
```

```
        ComplexMatrix U(NM*NM, NM*NM);
        ComplexMatrix V(NC, NM*NM);
        FloatVector S(NM*NM);

        cout << ”Calling function U\n”;
        createMatrixFromFileC(”U.txt”, NM*NM, NM*NM, U);
        cout << ”Calling function S\n”;
        createMatrixFromFileR(”S.txt”, NM*NV, S);   /* NM*NV*/
        cout << ”Calling function V\n”;
        createMatrixFromFileC(”V.txt”, NC, NM*NM, V);
        // createMatrixFromFileR(”S.txt”, NM, S);   Check!
        std::cout << ”U MAT size ” << U.rows() <<
         ”-” << U.cols() << std::endl;
        std::cout << ”V MAT size ” << V.rows() <<
        ”-” << V.cols() << std::endl;
        std::cout << ”S size ” << S.size() << std::endl;

        //std::cout << ”U: ” << U << std::endl;
        //std::cout << ”V: ” << V << std::endl;
        //std::cout << ”S: ” << S << std::endl;



        /******************/
        /* RECONSTRUCTION */
        /******************/

        /* Differential Matrix */
ComplexMatrix Es1_E(NM, NM), Es2_E(NM, NM);

createMatrixFromFileC(”Es1.txt”, NM, NM, Es1_E);
//std::cout << ”Es1_E: ” << Es1_E << std::endl;
createMatrixFromFileC(”Es2.txt”, NM, NM, Es2_E);
//std::cout << ”Es2_E: ” << Es2_E << std::endl;
```

```
ComplexMatrix Es_E(NM, NM);
Es_E = Es2_E - Es1_E;


        /* Normalization */

        complex<myFloat> tmp_var;
        time_t tstart, tend;

for(threshold_tmp = minT; threshold_tmp<maxT;
      threshold_tmp=threshold_tmp+stepT){ /* Start threshold loop */

        Eigen::FloatVector valsingn = S/S(0);
        valsingn = valsingn.cwiseAbs();

        valsingn = 20*(valsingn.array().log() / log(10.0));
        valsingn = valsingn.array() - threshold_tmp;
        valsingn = valsingn.cwiseAbs();

        int min_i, min_j;
        myFloat minimum = valsingn.minCoeff(&min_i, &min_j);

/* Reshape Difference Matrix Es into a Row Vector */
Eigen::Map<FloatRowVector> Es_vec_E(Es_E.data(), Es_E.size());

ComplexMatrix RI(NC, 1);
        RI.fill(0);

cout << ”INNER LOOP TRIP COUNT: min_i = ” << min_i << endl;
        auto start = std::chrono::steady_clock::now( );
        //tstart = time(0);
        for(j=0; j<min_i; j++){

        tmp_var = U.col(j).dot(Es_vec_E);
```

```
        tmp_var = tmp_var/S(j);
        ComplexVector tmp_vec = V.col(j) * tmp_var;
        RI = RI + tmp_vec;
                }

        //tend = time(0);
        auto elapsed = std::chrono::duration_cast<std::chrono::milliseconds>(
             std::chrono::steady_clock::now( ) - start );

std::cout << ”It took ” << elapsed.count( )
          <<” millisecond(s) for threshold:”<< threshold_tmp << endl;

//cout << ”It took ”<< difftime(tend, tstart)
  //<<” second(s) for threshold:”<< threshold_tmp << endl;

        /* Print results to file */
std::string fileName;
fileName = ”singleP_RI_threshold_” + patch::to_string(threshold_tmp);

        std::ofstream RIfile(fileName.c_str());
        RIfile << RI << std::endl;
        RIfile.close();

        } /* End threshold loop */


        printf(”\n--> Execution FINISHED! <--\n”);
        return 0;
        }


void createMatrixFromFileC(char fileName[],
         myInt r, myInt c, ComplexMatrix &Mat_E){
```

```
                FILE *tmp = NULL;
                myInt i, j;
                double re, im;

        tmp = fopen(fileName, ”r”);
        if(tmp == NULL){
                printf(”Missing File: %s\n”, fileName);
                return;
                }

        printf(”File %s found.\n”, fileName);

        printf(”Matrix: %s [%d][%d] created!\n”, fileName, r, c);

for(i=0; i<r; i++){
        for(j=0; j<c; j++){
                fscanf(tmp, ”%lf %lfi ”, &re, &im);
                myFloat myRe, myIm;
                myRe = (myFloat) re;
                myIm = (myFloat) im;
                Mat_E(i, j) = myRe + myIm * If;
                }
        }

                return;
        }


void createMatrixFromFileR(char fileName[],
  myInt r, FloatVector &Vec_E){
        FILE *tmp = NULL;
        myInt i;
        double re;
tmp = fopen(fileName, ”r”);
```

```
if(tmp == NULL){
printf("Missing File: %s\n", fileName);
return;
}
printf("File %s found.\n", fileName);
printf("Vector: %s [%d] created!\n", fileName, r);
for(i=0; i<r; i++){
        fscanf(tmp, "%lf ", &re);
        Vec_E(i) = (myFloat) re;
}

        return;



}
```

[empty]

Bibliography

[1] D. M. Parkin, “Global cancer statistics in the year 2000,”Lancet Oncology, vol. 2, no.9, pp. 533–543, 2001.

[2] Sundhedsstyrelsen, Cancerregisteret 2001 (foreløbige tal for 2002- 2003), ser. Nye talfra Sundhedsstyrelsen. Copenhagen, Denmark: Sundhedsstyrelsen – Danish National Board of Health, 2005.

[2] Kræftstatistik baseret pa landspatientregisteret 2000–2004, ser. Nye tal fra Sundhedsstyrelsen. Copenhagen, Denmark: Sundhedsstyrelsen – Danish National Board of Health, 2006.

[4] American Cancer Society, Inc., Cancer Facts & Figures 2007. American Cancer Society, 2007.

[5] www.cancer.org

[6] http://www.who.int/news-room/fact-sheets/detail/cancer

[7] A. Langtry, ”Understanding Cancer of the Breast”, J. Kelly (Editor). Irish Cancer Society. Dublin, Ireland, 2008.

[8] Subcommittee, S.S., AHA statistical update. Circulation, 2007. 115: p. e69-e171.9. Economics, D.A., The economic impact of stroke in Australia. Canberra: Access Economics, 2013.

[9] B. Sarioglu, M. Tumer, U. Cindemir, B. Camli, G. Dundar, C. Ozturk, and A. D. Yalcinkaya, “An optically powered cmos tracking system for 3 t magnetic resonance environment,” IEEE Transactions on Biomedical Circuits and Systems, vol. 9, no. 1, pp. 12–20, Feb 2015

[10] Wang, J. and S. Dore, ”Inflammation after intracerebral hemorrhage”. J Cereb Blood Flow Metab, 2007. 27(5): p. 894-908.

[11] J. Redon, M. H. Olsen, R. S. Cooper, O. Zurriaga, M. A. Martinez-Beneito, S. Laurent, R. Cifkova, A. Coca, and G. Mancia, “Stroke mortality and trends from 1990 to 2006 in 39 countries from Europe and Central Asia: implications for control of high blood pressure,” European Heart Journal, vol. 32, no. 11, pp. 1424–1431, 2011.

[12] J. Olesen, M. G. Baker, T. Freund, M. di Luca, J. Mendlewicz, I. Ragan, and M. Westphal, “Consensus document on European brain research,” Journal of Neurology, Neurosurgery & Psychiatry, vol. 77, no. suppl 1, pp. i1–i49, 2006.

[13] E. J. Benjamin, M. J. Blaha, S. E. Chiuve, M. Cushman, S. R. Das, R. Deo, S. D. de Ferranti, J. Floyd, M. Fornage, C. Gillespie, C. R. Isasi, M. C. Jiménez, L. C. Jordan, S. E. Judd, D. Lackland, J. H. Lichtman, L. Lisabeth, S. Liu, C. T. Longenecker, R. H. Mackey, K. Matsushita, D. Mozaffarian, M. E. Mussolino, K. Nasir, R. W. Neumar, L. Palaniappan, D. K. Pandey, R. R. Thiagarajan, M. J. Reeves, M. Ritchey, C. J. Rodriguez, G. A. Roth, W. D. Rosamond, C. Sasson, A. Towfighi, C. W. Tsao, M. B. Turner, S. S. Virani, J. H. Voeks, J. Z. Willey, J. T. Wilkins, J. H. Wu, H. M. Alger, S. S. Wong, and P. Muntner, “Heart disease and stroke statistics—2017 update: A report from the American heart association,” Circulation, 2017.

[14] Mackay, J.; Mensah, G. The Atlas of Heart Disease and Stroke; World Health Organization: Geneve, Switzerland, 2004.

[15] Wang, J. and S. Dore, ”Inflammation after intracerebral hemorrhage”. J Cereb Blood Flow Metab, 2007. 27(5): p. 894-908.

[16] Baber, U., I. Mastoris, and R. Mehran, ”Balancing ischaemia and bleeding risks with novel oral anticoagulants”. Nat Rev Cardiol, 2014. 11(12): p. 693-703.

[17] P. T. Huynh, A. M. Jarolimek, and S. Daye, ”The false-negative mammogram, Radiographics”, vol. 18, pp. 11371154, 1998.

[18] A. Martellosio, M. Pasian, M. Bozzi, L. Perregrini, A. Mazzanti, F. Svelto, P. E. Summers, G. Renne, and M. Bellomi, “0.5-50 GHz dielectric characterisation of breast cancer tissues,” Electronics Lett., vol. 51, no. 13, pp. 974–975, 2015.

[19] J. A. Tobon V. et al., ”Design and modeling of a microwave imaging system for breast cancer detection,”2015 9th European Conference on Antennas and Propagation (EuCAP),Lisbon, 2015, pp.1-2

[20] P. M. Meaney, M. W. Fanning, D. Li, S. P. Poplack, and K. D. Paulsen, “A clinical prototype for active microwave imaging of the breast,” IEEE Trans. Microw. Theory Techn., vol. 48, no. 11, pp. 1841–1853, 2000.

[21] A,M. Hassan and M. El-Shenawee, ”Review of Electromagnetic Techniques for Breast Cancer Detection”, IEEE Rev. Biomed. Eng., vol. 4, 2011

[22] Michael D. Hill and Alastair M. Buchan, ”Thrombolysis for acute ischemic stroke: results of the Cancadian Alteplase for stroke Effectiveness Study”. Canadian Medical Association, 2005.

[23] National Cancer Institute [online](2011)Available:http://www.cancer.gov.

[24] M. Lazebnik, L. McCartney, D. Popovic, C. B. Watkins, M. J. Lindstrom, J. Harter, S. Sewall, A. Magliocco, J. H. Booske, M. Okoniewski and S. C. Hagness, ”A Large - Scale Study of the Ultrawideband Microwave Dielectric Properties of Normal Breast Tissue Obtained from Reduction Surgeries”, Physics in Medicine and Biology, Vol. 52, pp. 2637–2656, 2007.

[25] W. T. Joines, Y. Zhang, C. Li and R. L. Jirtle, ”The Measured Electrical Properties ofNormal and Malignant Human Tissues from 50 to 900 MHz”, Medical Physics, Vol. 21,No. 4, 1994.

[26] C. Gabriel, S. Gabriel and E. Corthout, ”The Dielectric Properties of Biological Tissues: I. Literature Survey”, Physics in Medicine and Biology, Vol. 41, pp. 2231- 2249, 1996.

[27] A. M. Campbell and D. V. Land, ”Dielectric Properties of Female Human Breast Tissue Measured In Vitro at 3.2 GHz”, Physics in Medicine and Biology, Vol. 37, No. 1, pp.193-210, 1992.

[28] S. Gabriel, R. W. Lau and C. Gabriel, ”The Dielectric Properties of Biological Tissues: II.Measurements in the Frequency Range 10 Hz to 20 GHz”, Physics in Medicine and Biology, Vol. 41, pp. 2251-2269, 1996

[29] S.S. Chaudhary, R. K. Mishra, A. Swarup and J. M. Thomas, ”Dielectric Properties of Normal and Malignant Human Breast Tissues at Radiowave and Microwave Frequencies” Indian Journal of Biochemistry & Biophysics, Vol.21, pp. 76-79, 1984.

[30] T. S. England and N. A. Sharples, ”Dielectric properties of the human body in the microwave region of the spectrum,” Nature, vol. 163, pp. 487-488, 1949.

[31] T. S. England, ”Dielectric properties of the human body for wavelength in the 1 -10 cm range,” Nature, vol. 1466, pp. 480–481, 1950.

[32] Semenov, S. Y., R. H. Svenson, and G. P. Tatsis, ”Microwave spectroscopy of myocardial ischemia and infarction. 1. Experimental study,” Ann. Biomed. Eng., Vol. 28, 4854, 2000.

[33] Semenov, S. Y., et al.,”Dielectrical spectroscopy of canine myocardium during acute ischemia and hypoxia at frequency spectrum from 100 kHz to 6 GHz,” IEEE Trans. Med. Imaging, Vol. 21, 547550, 1994.

[34] J. Olesen, A. Gustavsson, M. Svensson, H.-U. Wittchen, and B. Jönsson, “The economic cost of brain disorders in Europe,” European Journal of Neurology, vol. 19, no. 1, pp. 155–162, 2012

[35] (2011, 20 June). Emorial Hospital of Texas County. Available: http://www.mhtcguymon.org/

[36] (2013). The Radiology Information Resource for Patients: Available: http://www.radiologyinfo.org/content/mr_cardiac.htm

[37] (2012, 15 January). MRI scan for stroke diagnose Available: http://www.radiologyinfo.org/content/mr_cardiac.htm

[38] (2013, 3 February). CT Scan :Available: http://www.fda.gov/Radiation

[39] (2012, 25 January). MRI scan for stroke diagnose ; Available: http://www.radiologyinfo.org/content/mr_cardiac.htm

[40] A. Abubakar, P. M. Van den Berg, and J. J. Mallorqui, ”Imaging of biomedical data using a multiplicative regularized contrast source inversion method” IEEE Transactions on Microwave Theory and Techniques, vol. 50, pp. 1761-1771, 2002.

[41] Vitaliy Zhurbenko, “Challenges in the Design of Microwave Imaging Systems for Breast Cancer Detection”, Advances in Electrical and Computer Engineering, Volume 11, Number 1,2011.

[42] Fear C, Hagness S C, Meaney P M, et al. “Enhancing breast Tumor detection with near fieldimaging” [J]. IEEE Microwave Magazine 2002,3(1): 48-56

[43] P. M. Meaney, K. D. Paulsen, J. T. Chang, M. W. Fanning, and A. Hartov,”Nonactive antenna compensation for fixed-array microwave imaging. II. Imaging results,” IEEE Transactions on, Medical Imaging, vol. 18, pp. 508-518, 1999.

[44] E. C. Fear, P. M. Meaney, and M. A. Stuchly, ”Microwaves for breast cancer detection?,”IEEE, Potentials,vol. 22, pp. 12-18, 2003.

[45] Fear E C, Sill J M, ”Preliminary investigation of tissue sensing adaptive Radar for breast tumor detection” Proceeding of the 25th Annual Meeting of the IEEE Engineering in Medicine and Biology Society, Piscatawau: IEEE, 2003:3787-33890

[46] M. A. Stuchly, E. C. Fear, X. Li, S. C. Hagness, ”Confocal microwave imaging for breast cancer detection: Localization of tumors in three dimensions,” IEEE Transactions on Biomedical Engineering, vol. 49, pp. 812-822, 2002.

[47] X. Li and S. C. Hagness, ”A confocal microwave imaging algorithm for breast cancer detection,” IEEE Microwave and Wireless Components Letters, vol. 11, no. 3, pp. 130-132, 2001

[48] S. C. Hagness, A. Taflove, and J. E. Bridges, ”Two-dimensional FDTD analysis of a pulsed microwave confocal system for breast cancer detection: fixed-focus and antenna-array sensors,” IEEE Transactionson Biomedical Engineering, vol. 45, pp. 1470-1479, 1998

[49] Fear C, Hagness S C, Meaney P M, et al. “Enhancing breast Tumor detection with near field imaging”. IEEE Microwave Magazine 2002,3(1): 48-56

[50] L. E. Larsen and J. H. Jacobi, ”Microwave scattering parameter imagery of an isolated canine kidney,” Medical physics, vol. 6, p. 394, 1979.

[51] E. Fear and M. Stuchly, ”Microwave detection of breast cancer,” IEEE Transactions on Microwave Theory and Techniques, vol. 48, pp. 1854-1863, 2000.

[52] E. C. Fear and M. Okoniewski, ”Confocal microwave imaging for breast tumor detection: Application to a hemispherical breast model,” IEEE MTT-S International, Microwave Symposium Digest, 2002, vol. 3, pp.1759-1762, 2002.

[53] X. Li, S. K. Davis, S. C. Hagness, D. W. van der Weide, and B. D. Van Veen, ”Microwave imaging via space-time beamforming: Experimental investigation of tumor detection in multilayer breast phantoms,” IEEE Transactions on Microwave Theory and Techniques, vol. 52, no. 8, pp. 1856-1865, 2004.

[54] I. Craddock, A. Preece, J. Leendertz, M. Klemm, R. Nilavalan, and R. Benjamin, ”Development of a hemi-spherical wideband antenna array for breast cancer imaging,” European Conference on Antennas and Propagation EUCAP, pp. 6-10, 2006.

[55] I. Craddock, M. Klemm, J. Leendertz, A. Preece, and R. Benjamin, ”An improved hemispeherical antenna array design for breast imaging,” The Second European Conference EuCAP, pp. 1-5, 2007.

[56] W. C. Khor and M. E. Bialkowski, ”Investigations into cylindrical and planar configurations of a microwave imaging system for breast cancer detection,” IEEE, Antennas and Propagation Society International Symposium, pp. 263-266, 2006.

[57] P. M. Meaney, M. W. Fanning, T. Raynolds, C. J. Fox, Q. Fang, C. A. Kogel, et al., ”Initial clinical experience with microwave breast imaging in women with normal mammography,” Academic radiology, vol. 14, pp. 207-218, 2007.

[58] M. Bialkowski and Y. Wang, ”UWB cylindrical microwave imaging system employing virtual array antenna concept for background effect removal,” Microwave and Optical Technology Letters, vol. 53, pp. 1100-1104, 2011.

[59] Y. Kuwahara, K. Suzuki, H. Horie, and H. Hatano, ”Conformal array antenna with the aspirator for the microwave mammography,” IEEE International Symposium (APSURSI) on Antennas and Propagation Society, pp. 1-4, 2010.

[60] A. A. Bakar, D. Ireland, A. Abbosh, and Y. Wang, ”Experimental Assessment of Microwave Diagnostic Tool for Ultra-Wideband Breast Cancer Detection,” Progress In Electromagnetics Research M, vol. 23, 2012.

[61] M. Haynes, J. Stang, and M. Moghaddam, ”Microwave breast imaging system prototype with integrated numerical characterization,” Journal of Biomedical Imaging, vol. 2012, p. 2, 2012.

[62] H. Trefna and M. Persson, ”Antenna array design for brain monitoring,” IEEE International Symposium Antennas and Propagation Society AP-S vol. , pp. 1-4, 2008.

[63] D. Ireland and M. Bialkowski, ”Feasibility study on microwave stroke detection using a realistic phantom and the FDTD method,” Asia-Pacific Microwave Conference 2010, pp. 1-4, 2010.

[64] (2011, 26 May). Dielectric properties of body tissues in the frequency range 10 Hz– 100 GHz Available: http://niremf.ifac.cnr.it/tissprop/

[65] D. Ireland and M. E. Bialkowski, ”Microwave head imaging for stroke detection,” Progress In Electromagnetics Research M, vol. 21, pp. 163-175, 2011.

[66] H. Zhang, A. O. El-Rayis, N. Haridas, N. H. Noordin, A. T. Erdogan, and T. Arslan, ”A smart antenna array for brain cancer detection,” Antennas and Propagation Conference (LAPC), 2011 Loughborough, pp. 1-4, 2011.

[67] R. Scapaticci, L. Di Donato, I. Catapano, and L. Crocco, ”A feasibility study on microwave imaging for brain stroke monitoring,” Progress In Electromagnetics Research B, vol. 40, pp. 305-324, 2012.

[68] S. Y. Semenov and D. R. Corfield, ”Microwave tomography for brain imaging: Feasibility assessment for stroke detection,” International Journal of Antennas and Propagation, vol. 2008, 2008.

[69] D. Liang, H. T. Hui, T. S. Yeo, and B. K. Li, “Stacked phased array coils for increasing the signal-to-noise ratio in magnetic resonance imaging,” IEEE Transactions on Biomedical Circuits and Systems, vol. 7, no. 1, pp.24–30, Feb 2013.

[70] B. Sarioglu, M. Tumer, U. Cindemir, B. Camli, G. Dundar, C. Ozturk, and A. D. Yalcinkaya, “An optically powered cmos tracking system for 3D magnetic resonance environment,” IEEE Transactions on Biomedical Circuits and Systems, vol. 9, no. 1, pp. 12–20, Feb 2015.

[71] S. M. Sohn, L. DelaBarre, A. Gopinath, and J. T. Vaughan, “Design of an electrically automated rf transceiver head coil in mri,” IEEE Transactions on Biomedical Circuits and Systems, vol. 9, no. 5, pp. 725–732, Oct 2015.

[72] Casu, M.R.; Vacca, M.; Tobon, J.A.; Pulimeno, A.; Sarwar, I.; Solimene, R.; Vipiana, F. ”A COTS-Based Microwave Imaging System for Breast-Cancer Detection”. IEEE Trans. Biomed. Circ. Syst.2017, 11, 804-814.

[73] Meaney, P. ”Microwave Imaging and Emerging Applications”. Int. J. Biomed. Imaging 2012, doi:10.1155/2012/252093.

[74] M. Lazebnik et al. “A large-scale study of the ultra wideband microwave dielectric properties of normal, benign and malignant breast tissues obtained from cancer surgeries”, Physics in Medicine and Biology, 2007

[75] J. A. Tobon Vasquez, F. Vipiana, G. Dassano, M. R. Casu, M. Vacca, A. Pulimeno, and R. Solimene, “Experimental results on the use of the MUSIC algorithm for early breast cancer detection,” in Int. Conf. on Electromagnetics in Advanced Applications (ICEAA), 2015.

[76] E. C. Fear, S. C. Hagness, P. M. Meaney, M. Okoniewski, and M. A. Stuchly, ”Enhancing breast tumor detection with near-field imaging,” IEEE, Microwave Magazine, vol. 3, pp. 48-56, 2002.

[77] V. Zhurbenko, ”Challenges in the design of microwave imaging systems for breast cancer detection,” Advances in Electrical and Computer Engineering, vol. 11, pp. 91-96, 2011.

[78] P. M. Meaney, K. D. Paulsen, J. T. Chang, M. W. Fanning, and A. Hartov, ”Nonactive antenna compensation for fixed-array microwave imaging. II. Imaging results,” IEEE Transactions on, Medical Imaging, vol. 18, pp. 508-518, 1999.

[79] M. Bassi, A. Bevilacqua, A. Gerosa, and A. Neviani, “Integrated SFCW transceivers for UWB breast cancer imaging: Architectures and circuit constraints,” IEEE Trans. Circuits Syst. I, vol. 59, no. 6, pp. 1228–1241,2012.

[80] M. Bassi, M. Caruso, M. S. Khan, A. Bevilacqua, A. D. Capobianco, and A. Neviani, “An integrated microwave imaging radar with planar antennas for breast cancer detection,” IEEE Trans. Microw. Theory Techn., vol. 61,no. 5, pp. 2108–2118, May 2013.

[81] G. Ruvio, R. Solimene, A. Cuccaro, and M. J. Ammann, “Comparison of noncoherent linear breast cancer detection algorithms applied to a 2-D numerical model,” IEEE Antennas Wireless Propag. Lett., vol. 12, pp. 853–856, 2013.

[82] M. D. Hossain, A. S. Mohan, and M. J. Abedin, “Beamspace time-reversal microwave imaging for breast cancer detection,” IEEE Antennas Wireless Propag. Lett., 2013.

[83] Vivado Design Suite User Guide, High-Level Synthesis” in Xilinx, 2014

[84] Zynq ZedBoard Concepts, Tools, and Techniques A hands-on guide to effective embedded system design" in Xilinx, 2013.

[85] AXI Reference Guide Vivado Design Suite" in Xilinx, 2015.

[86] R. Figueras, J. Sabadell, L. Teres, and F. Serra-Graells, "A 70-mm pitch 8-mw selfbiased charge-integration active pixel for digital mammography," IEEE Transactions on Biomedical Circuits and Systems, vol. 5, no. 5, pp. 481-489, Oct 2011.

[87] D. Liang, H. T. Hui, T. S. Yeo, and B. K. Li, "Stacked phased array coils for increasing the signal-to-noise ratio in magnetic resonance imaging," IEEE Transactions on Biomedical Circuits and Systems, vol. 7, no. 1, pp. 24–30 Feb 2013.

[88] B. Sarioglu, M. Tumer, U. Cindemir, B. Camli, G. Dundar, C. Ozturk, and A. D. Yalcinkaya, "An optically powered cmos tracking system for 3D magnetic resonance environment," IEEE Transactions on Biomedical Circuits and Systems, vol. 9, no. 1, pp. 12–20, Feb 2015.

[89] S. M. Sohn, L. DelaBarre, A. Gopinath, and J. T. Vaughan, "Design of an electrically automated rf transceiver head coil in mri," IEEE Transactions on Biomedical Circuits and Systems, vol. 9, no. 5, pp. 725–732, Oct 2015.

[90] Ruvio, G., Solimene, R., D'Alterio, A., Ammann, M.J., Pierri, R. "RF breast cancer detection employing a noncharacterized vivaldi antenna and a music-inspired algorithm". Int. J. RF Microw. Comput. Aided Eng. 23(5), 598–609 (2013).

[91] G. Ruvio, R. Solimene, A. Cuccaro, D. Gaetano, J. E. Browne, and M. J. Ammann, "Breast cancer detection using interferometric music: Experimental and numerical assessment," Medical Physics, vol. 41, no. 103101, pp. 1–11, 2014.

[92] P.M. Meaney, M.W. Fanning, D. Li, S.P. Poplack, and K.D. Paulsen, "A clinical prototype for active microwave imaging of the breast" IEEE Transactions on Microwave Theory and Techniques, vol. 48, no. 11, pp. 1841–1853, Nov 2000

[93] J. A. Tobon Vasquez, E. Attardo, G. Dassano, F. Vipiana, M. R. Casu, M. Vacca, A. Pulimeno, and G. Vecchi, "Design and modeling of a microwave imaging system for breast cancer detection," in 9th European Conf. Antennas Propag. (EuCAP), 2015

[94] D.Gibbins, M.Klemm, I.J.Craddock, J.A.Leendertz, A.Preece, R. Benjamin, "A Comparison of a Wide-Slot and a Stacked Patch Antenna for the Purpose of Breast Cancer Detection," Antennas and Propagation, IEEE Transactions" on , vol.58, no.3, pp.665,674, March 2010.

[95] P. M. Meaney, F. Shubitidze, M. W. Fanning, M. Kmiec, N. R. Epstein, and K. D. Paulsen, "Surface wave multipath signals in near-field microwave imaging," Int. Journal of Biomed. Imag., vol. 2012, 2012.

[96] M. Lazebnik, L. McCartney, D. Popovic, C. B. Watkins, M. J. Lindstrom, J. Harter, S. Sewall, A. Magliocco, J. H. Booske, M. Okoniewski, and S. C. Hagness, "A largescale study of the ultrawideband microwave dielectric properties of normal breast tissue obtained from reduction surgeries," Phys Med Biol., vol. 52, no. 10, pp. 2637– 2656, Apr 2007

[97] N. Joachimowicz, B. Duchene, C. Conessa, O. Meyer, and O. Dubrunfaut, "Easy-toproduce stable-in-time 3d- printed breast phantoms for microwave imaging," in PIERS, 2015

[98] B. Razavi, RF Microelectronics. Upper Saddle River, NJ: Prentice-Hall, 1998.

[99] R. Scapaticci, L. Di Donato, I. Catapano, and L. Crocco, "A feasibility study on microwave imaging for brain stroke monitoring," Progress in Electromagnetics Research B, Vol. 40, 305-324, 2012 (doi:10.2528/PIERB12022006).

[100] Mackay, J.; Mensah, G. "The Atlas of Heart Disease and Stroke"; World Health Organization: Geneve, Switzerland, 2004.

[101] Sarwar I, Turvani G, Casu MR, Tobon JA, Vipiana F, Scapaticci R, Crocco L. "Low-Cost Low-Power Acceleration of a Microwave Imaging Algorithm for Brain Stroke Monitoring". Journal of Low Power Electronics and Applications. 2018; 8(4):43.

[102] M. Pastorino, Microwave imaging vol. 208:John Wiley& Sons, 2010.

[103] Semenov, S.Y.; Corfield, D.R. "Microwave Tomography for Brain Imaging: Feasibility Assessment for Stroke Detection". Int. J. Antennas Propag. 2008,

[104] R. Scapaticci, O. M. Bucci, I. Catapano, L. Crocco, "Differential Microwave Imaging for Brain Stroke Follow up", International Journal of Antennas and Propagation, 2014, Article ID 312528, 11 pages.

[105] Vasquez, J.A.T.; Scapaticci, R.; Turvani, G.; Vacca, M.; Sarwar, I.; Casu, M.R.; Dassano, G.; Joachimowicz, N.Duchˇene, B.; Bellizzi, G.; et al. "A feasibility study for cerebrovascular diseases monitoring via microwave imaging". In Proceedings of the 2017 International Conference on Electromagnetics in Advanced Applications (ICEAA), Verona, Italy, 11–15 September 2017; pp. 1280–1282,

[106] Bisio, I.; Estatico, C.; Fedeli, A.; Lavagetto, F.; Pastorino, M.; Randazzo, A.; Sciarrone, "A. Brain Stroke Microwave Imaging by Means of a Newton-ConjugateGradient Method in Lp Banach Spaces". IEEE Trans.Microw. Theory Tech. 2018, 66, 3668–3682,

[107] Persson, M.; Fhager, A.; Trefná, H.D.; Yu, Y.; McKelvey, T.; Pegenius, G.; Karlsson, J.; Elam, M. "Microwave-Based Stroke Diagnosis Making Global Prehospital Thrombolytic Treatment Possible". IEEE Trans.Biomed. Eng. 2014, 61, 2806–2817,

[108] Mohammed, B.J.; Abbosh, A.M.; Mustafa, S.; Ireland, D. ”Microwave System for Head Imaging”. IEEE Trans.Instrum. Meas. 2014, 63, 117–123,

[109] Mobashsher, A.T.; Abbosh, A.M.; Wang, Y. ”Microwave System to Detect Traumatic Brain Injuries Using Compact Unidirectional Antenna and Wideband Transceiver With Verification on Realistic Head Phantom”, IEEE Trans. Microw. Theory Tech. 2014, 62, 1826–1836,

[110] Bertero, M.; Boccacci, P. ”Introduction to Inverse Problems in Imaging”; CRC Press: Bristol, UK, 1998.

[111] Eigen. Available online: http://eigen.tuxfamily.org.

[112] Xillinux. Available online: http://xillybus.com/xillinux

[113] B. Ward, “How Linux Boots” in How Linux Works, 1st. Ed, No Starch Press, 2004, pp. 54 - 63.

[114] http://www.zynqbook.com/

[115] Romeo, Stefania & Di Donato, Loreto & Bucci, Ovidio & Catapano, Ilaria & Crocco, Lorenzo & Scarfi, Maria Rosaria & Massa, Rita.”Dielectric characterization study of liquid based materials for mimicking breast tissues”. Microwave and Optical Technology Letters. 53. 1276-1280. 10.1002/mop.26001. (2011)

[116] M. Lazebnik, L. McCartney, D. Popovic, C. B. Watkins, M. J. Lindstrom, J. Harter, S. Sewall, A. Magliocco, J. H. Booske, M. Okoniewski, and S. C. Hagness, “A largescale study of the ultrawideband microwave dielectric properties of normal breast tissue obtained from reduction surgeries,” Phys Med Biol., vol. 52, no. 10, pp.2637– 2656, Apr 2007.

[117] M. Donelli, I. J. Craddock, D. Gibbins, and M. Sarafianou, ”A Three-Dimensional Time Domain Microwave Imaging Method for Breast Cancer Detection Based on an Evolutionary Algorithm,” Progress In Electromagnetics Research M, Vol. 18, 179-195, 2011. doi:10.2528/PIERM11040903

[118] T. Henriksson, M. Klemm, D. Gibbins, J. Leendertz, T. Horseman, A. W. Preece, R. Benjamin, and I. J. Craddock, “Clinical trials of a multistatic UWB radar for breast imaging,” in IEEE Antennas and Propagation Conference (LAPC), Loughborough, UK, 2011

[119] Ley, Sebastian & Sachs, J & Helbig, M. (2017). ”MNP enhanced microwave breast cancer imaging based on ultra-wideband pseudo-noise sensing”. 2754-2757. 10.23919/EuCAP.2017.7928407.

[120] M. J. Burfeindt, T. J. Colgan, R. O. Mays, J. D. Shea, N. Behdad, B. D. Van Veen, and S. C. Hagness, “MRI-derived 3-d-printed breast phantom for microwave breast imaging validation,” IEEE Antennas and Wireless Propagation Letters, Vol. 11 (2012), pp. 1610–1613.